



# PARITANTRA

Journal of Systems Science  
and Engineering

A PUBLICATION OF  
SYSTEMS SOCIETY OF INDIA

Selected Papers from  
**NSC-2021: Systems for Sustainable  
Healthcare Habitats**

A SPECIAL ISSUE

VOLUME 26

NUMBER 1

JUNE 2022

ISSN 0972-5032(P)

# PARITANTRA

Journal of Systems Science and Engineering

Volume 26

Number 1

June 2022

ISSN 0972-5032 (P)



Gram: TECHNOLOGY DELHI  
Telex: 31-73087 IIT IN  
FAX: 91-11-6862037  
Electronic Mail: pss @ ee.iitd.ernet.in

**P. S. SATSANGI**

B.Sc. (Elec. Engg. Banaras Hindu University (BHU))  
M.S. (Michigan State University, USA)  
Ph.D. (University of Waterloo, Ontario, Canada)

Professor  
Electrical Engineering Department (EE)  
& Applied Systems Research Programme  
Indian Institute of Technology  
Hauz Khas, New Delhi - 110016  
Res. 3, Street C, I.I.T. Estate, New Delhi - 110016  
Phone: Off. 651840, 666979 Ext. 2207, 653561 (EE) Res.: 665424

**P. S. SATSANGI**  
Managing Director

**FOUNDATION FOR  
INNOVATION AND  
TECHNOLOGY  
TRANSFER**

Gram: TECHNOLOGY DELHI  
Telex: 31-73087 IIT IN  
Fax: 91-11-6862037  
Phone: Off.: 651840, 666979 Ext. 2207  
653561 (EE) Res.: 665424

## EDITORIAL BOARD

**EMERITUS EDITOR**

**Prof. Prem Saran Satsangi**

*Chairman*

Advisory Committee on Education  
Dayalbagh Educational Institutions  
Dayalbagh, Agra 282005

*Retired Professor*

Department of Electrical Engineering, IIT Delhi

&

*Visiting Post Doctoral Fellow*  
Faculty of Environmental Studies  
University of Waterloo  
(During Summer Quarter 1970  
on Vacation Leave from IIT Delhi)

**CHIEF EDITOR**

**Prof. Prem Kumar Kalra**

*Professor & Head*

Department of Computer Science and Engineering, IIT Delhi  
*President, Systems Society of India*

## EDITORIAL ADVISORY BOARD

- **Prof. Anand Srivastava**  
Professor  
Department of Mathematics  
University of Kiel
- **Prof. Prem Kumar Kalra**  
Director/Vice-Chancellor  
Dayalbagh Educational Institute
- **Prof. Anna Margaretha Horatschek**  
Professor Emeritus  
Department of English  
University of Kiel
- **Prof. Peter Roe**  
Professor Emeritus  
Department of Systems Design Engineering  
University of Waterloo
- **Prof. Karmeshu**  
Distinguished Professor  
University of Petroleum and Energy Studies  
Honorary Professor, Shiv Nadar University
- **Prof. Siddhartha Mukhopadhyay**  
Professor  
Department of Electrical Engineering  
IIT Kharagpur

- **Prof. Gordon Savage**  
Professor  
Department of Systems Design Engineering  
University of Waterloo
- **Prof. D. Anand Rao**  
Retired Professor  
Department of Electrical Engineering  
Dayalbagh Educational Institute
- **Prof. Pami Dua**  
Director/Vice-Chancellor  
Delhi School of Economics  
University of Delhi
- **Dr. Bani Dayal Dhir**  
Assistant Professor  
Department of English Studies  
Dayalbagh Educational Institute
- **Prof. C. Patvardhan**  
Professor  
Department of Electrical Engineering  
Dayalbagh Educational Institute
- **Prof. Huzur Saran**  
Professor  
Department of Computer Science and Engineering  
IIT Delhi
- **Prof. Vishal Sahni**  
Retired Professor  
Department of Electrical Engineering  
Dayalbagh Educational Institute  
Manager, Rajaborari Estate
- **Dr. Dayal Pyari Srivastava**  
Assistant Professor  
Department of Physics and Computer Science  
Dayalbagh Educational Institute
- **Dr. Prem Sewak Sudhish**  
Associate Professor  
Department of Physics and Computer Science  
Dayalbagh Educational Institute
- **Prof. V.B. Gupta**  
Editor, ODL Newsletter  
Vice Chairman, Advisory Committee on Education  
Coordinator, Distance Education Program,  
Dayalbagh Educational Institute

### EDITORIAL COORDINATOR

**Prof. D. Bhagwan Das**  
Professor, Department of Electrical Engineering  
Dayalbagh Educational Institute (Deemed to be University)  
Dayalbagh, Agra 282005, INDIA  
(email: systems.society@gmail.com)

### Published by

**Systems Society of India**  
IT Centre, DEI ICT Distance Education Centre  
Dayalbagh Educational Institute (Deemed to be University)  
Model School, Soami Nagar, New Delhi 110017

*Copyright © 2022, Systems Society of India. All rights reserved. No part of this publication may be reproduced, stored, transmitted, or disseminated in any form, or by any means, without prior written permission from the Editorial Office, to whom all requests to reproduce copyright material should be directed.*

# PARITANTRA

Journal of Systems Science and Engineering

## Aims and Scope

This journal publishes original research and advancement in the field of theory and applications of systems science and engineering. The journal is primarily devoted to unification of themes, cross fertilization of ideas, identification and characterization of underlying quantitative and qualitative features of problem formulation and general solution; and solution of multi-level interdisciplinary socio-economic, engineering-economic and real-world problems in the context of national/global development. The journal has a very wide scope which includes applied systems research, systems modelling methodology, socio-economic and environmental systems, operational research and management, informatics, artificial intelligence and soft systems including literary systems and theology ("Better Worldliness").

## Manuscript Preparation

Authors are requested to prepare their manuscripts using a standard manuscript format template provided on the SSI website: [www.sysi.org](http://www.sysi.org) in MS word.

## Submission

Papers may be submitted electronically to the Editorial Coordinator.  
(email: [systems.society@gmail.com](mailto:systems.society@gmail.com))

PARITANTRA Journal of Systems Science and Engineering has a priority access to papers presented at meetings organized or sponsored by SSI. These papers may need an extension and further review before they are ready for publication. In addition, the journal may bring a special issue with papers which obtain the best paper awards during the presentations in a National Systems Conference. The journal also encourages special issues on emerging themes in systems science and engineering, a proposal for which should be submitted to the Chief Editor through the Editorial Coordinator.

## Copyright

All authors must sign the Transfer of Copyright Agreement before the article can be published. This transfer agreement enables SSI to protect the copyrighted material for the authors, without affecting the authors' proprietary rights. The copyright transfer covers the exclusive rights to reproduce and distribute the article, including reprints, photographic reproductions, microfilm or any other reproductions of similar nature and translations, and includes the right to adapt the article for use in conjunction with computer systems and programs, including reproduction or publication in machine-readable form and incorporation in retrieval systems. Authors are responsible for obtaining from the copyright holder permission to reproduce any figures or other material included in the paper for which copyright already exists.

# Editorial

## Selected Papers from NSC-2021: Systems for Sustainable Healthcare Habitats

### A SPECIAL ISSUE

The Dayalbagh Educational Institute (DEI), in association with Systems Society of India (SSI), organised the 44th National Systems Conference (NSC-2021) on Systems for Sustainable Healthcare Habitats on 22 – 23 May, 2021 at Dayalbagh Educational Institute, Agra, India.

DEI, SSI and the NSC-2021 Program and Organising Committee are eternally grateful for the inspiration, blessings, guidance and direction received from Revered Prof. P.S. Satsangi Sahab, Founding President of the Systems Society of India; Chairman of the Advisory Committee on Education for Dayalbagh Educational Institutions (a non-statutory body constituted to serve as a think-tank to suggest inter-alia steps necessary for achieving highest levels of excellence); and the Chief Patron for the 44<sup>th</sup> National Systems Conference, 2021.

A call for papers was sent out in March 2021, there were 57 papers submitted from different institutions. After review 30 papers for oral presentations and 10 papers for poster presentations were selected. Oral presentations were divided into 6 broad categories based on the subject area, with 5 papers in each category.

The conference was held online with a few thousand participants in each session across the globe connected in the virtual mode. For each paper, a pre-recorded video of 8-10 minutes was presented, followed by a live audio interaction with Q&A. Similarly, for each paper in the poster session a pre-recorded video of 3 minutes or less was presented followed by a live audio interaction.

At the brief inaugural session, a short video by Prof. Erik Goodman from Michigan State University was played where he saluted Revered Prof. P.S. Satsangi Sahab for His vision in founding and nurturing the SSI and he expressed his best wishes for the success of NSC-2021. The conference had four plenary talks by internationally reputed systems scientists in different areas — Prof. Mo Jamshidi, University of Texas at San Antonio, USA; Prof. Evangelyn C. Alocilja, Michigan State University, USA; Prof. Laxmidhar Behera, IIT Kanpur (now at IIT Mandi), India; and Dr Tom Rand, ArcTern Ventures, Canada. A session on What GenNext Thinks was organised with six invited short talks by outstanding young researchers from various parts of the world giving their ideas of research. A panel discussion was moderated by Dr. Anoop Srivastava, retired Additional Director General, Railway Protection Force, with eminent panelists on the theme of the conference, i.e., Systems for Sustainable Healthcare Habitats. At the end, an award ceremony was held for the SSI awards and the best papers awards followed by a short cultural program presented by the students of DEI, which was very well appreciated.

This Special Issue is prepared with six papers that received the best paper award in each of the six oral sessions corresponding to the six categories – consciousness and biological systems, education systems, environment systems, healthcare systems, information and communication systems, and mathematical systems. The papers were reviewed and were duly revised for publication in this issue.

We sincerely appreciate the efforts of all authors in contributing to this Special Issue. We would also like to express our deep gratitude to the Editorial Board of the journal PARITANTRA for supporting and sponsoring this Special Issue. We also gratefully acknowledge competent assistance from Dr. Priti Gupta, IIT Delhi for copy editing and proofreading and Mrs. Aruna Sharma for design and layout.

- NSC-2021 Program and Organising Committee

# PARITANTRA

Journal of Systems Science and Engineering

Volume 26

Number 1

June 2022

ISSN 0972-5032 (P)

## Selected Papers from NSC-2021: Systems for Sustainable Healthcare Habitats

A SPECIAL ISSUE

### Contents

Calibration of Off-the-Shelf Low-Cost Wearable EEG Headset for Application in Field Studies for Children <b>Manvi Jain and C.M. Markan</b>	1
Extractive Lecture Summarization System Using Evolutionary Algorithms – Optimizing Word, Sentence and Text Features <b>Binathi Bingi and Lotika Singh</b>	8
Self-Powered and Self-Sustained Energy Systems: Energy Autonomy in the Internet-of-Things Systems <b>Ankit Mittal and Aatmesh Shrivastava</b>	15
Low-Power and High-Frequency Optogenetic Retinal Prosthetics with ChRmine <b>Himanshu Bansal, Neha Gupta and Sukhdev Roy</b>	27
Deep Feature Compression Based Ensemble Model Towards Content Based Image Retrieval <b>Rohan Raju Dhanakshirur and Prem Kumar Kalra</b>	33
Separation Axioms of the Space of Endless Causal Curves <b>Gunjan Agrawal and Shruti Sinha</b>	41
<b>Appendix: NSC-2021 Conference Committee</b>	<b>46</b>

# Calibration of Off-the-Shelf Low-Cost Wearable EEG Headset for Application in Field Studies

Manvi Jain<sup>1\*</sup>, C.M. Markan<sup>2</sup>

<sup>1</sup>Department of Cognitive Sciences,

<sup>2</sup>Department of Physics and Computer Science,  
Dayalbagh Educational Institute, Agra, 282005, India

*Electroencephalography (EEG) is an integral tool in neurocognitive research worldwide. However, research grade EEG (32/64ch) systems are expensive and are cumbersome to setup. While high density EEG systems are important for clinical usage, they are not suited for field studies (outside the lab). Further, the long setup time of EEG can be bothersome to specific subject categories including children and elderly. In such cases off-the-shelf Low-Cost Dry EEG Devices (LCDE) have been proposed as promising substitutes. However, small number of electrodes in LCDE limit the detection scalp area reducing the utility of an LCDE only to a specific set of cognitive tasks. This paper proposes a novel methodology for calibration of an LCDE (e.g., DREEM Headband) to identify the specific class of cognitive tasks an LCDE is likely suited for. The methodology involves comparative analysis of recorded EEG data using LCDE with simulations of EEG-like signals (simulated using BESA software) by embedding dipoles in specific brain regions. As a pilot study, simulated signals in the four brain lobes were inverse mapped qualitatively to predict position and orientation of dipoles resulting in brain activity. We also did a comparative analysis of various LCDEs. In conclusion, we have created a list of psychological studies which can be performed using various LCDEs, capable of replacing traditional and expensive wet EEG systems in both inside and outside lab studies.*

**Keywords** – Dry EEG, DREEM, Inverse mapping, Localization error, BESA, Dipole simulation, Psychological testing

## I. INTRODUCTION

Electroencephalography (EEG) signals reflect physiological markers of cognition and awareness [1]. Traditional EEG systems extensively used in research today are usually very expensive and fragile. More importantly, they use dozens of channels and have detailed setup time, rendering their use highly impractical in outside lab settings [2]. In such conditions, LCDEs as shown in Fig. 1 could be recruited in neuropsychological studies for obtaining results similar to that recorded using standard wet EEG systems [1]–[3]. The devices shown in Fig. 1 are advantageous over traditional EEG systems due to several reasons. Firstly, these are head band-like devices which can be carried easily in field settings. They are plugin-play systems, therefore offer an easy, faster and user-friendly setup. They have fewer channels thereby allowing to focus on specific brain regions depending

upon the task displayed [4]. Moreover, they can be used in studies with children as participants when cumbersome setup of wet EEG is difficult. The LCDE to be used must be chosen on the basis of availability and accessibility of resources, setup time required, and available technical expertise. However, research shows that cognitive activities that can be accounted for with such devices are limited primarily due to fewer number of available channels [2], [5]. Most of the psychological tests performed using EEG devices involve measuring activations in specific brain regions. The fact that LCDEs contain a smaller number of channels becomes important because usually psychologists find it difficult to identify the electrodes specific to the region of interest in the brain according to the test in use, thus, extracting a data full of noise from unrequired channels in the EEG system. To identify a solution to this problem, we performed a pilot study in which we simulated activity in all four brain lobes (refer to Fig. 3) to recognize positions and amount of minimum number of electrodes and orientation of dipoles that are required to produce projected activity in specific brain regions.

\*Corresponding author: manvijain65@gmail.com  
ISSN 0972-5032 (P), Copyright ©2022, SSI

In Section III, we use the simulation model to produce EEG-like activity in brain regions covered by an LCDE (Fig. 1a) in order to map comparison between simulated and real data. Result of Section III is a chart of cognitive studies which can be performed using available LCDEs based on the cognitive activity localized in specific brain lobes for future reference while identifying a suitable dry EEG device corresponding to the psychological tests applied. For example, visual and basic cognitive tasks based on analytical problem-solving skills are most suitable for analysis using devices that cover frontal brain region such as DREEM headband and Emotiv epoc+ (Fig. 1a and 1c). Some low-cost and easily accessible LCDEs are reviewed briefly on the basis of the number of channels and major characteristic features below:

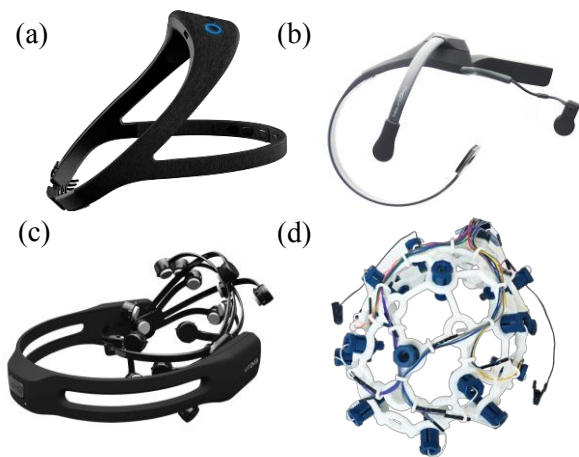


Fig. 1: Low-cost Dry EEG (LCDE) devices. (a) DREEM headband [28], (b) Neurosky mindwave mobile [29], (c) Emotiv epoc+ [30] and (d) OpenBCI Ultracortex Mark IV

**DREEM Headband:** This headband-like dry EEG device covers frontal and occipital regions of brain with electrodes placed at F7, F8, Fp1, O1, O2 and Fp2 as ground. Signals are sampled at 250 Hz. Along with electrodes, it also consists of a pulse sensor to monitor heart rate and accelerometer to measure head movements and respiratory rate [3].

**Emotiv epoc+:** This device is extensively used in research in the fields of Brain-computer interface and brain state detection [6]. It consists of two electrode arms, each comprising several sensor electrodes along with two reference electrodes covering the frontal, temporal, parietal, and occipital lobes of brain at following electrode positions- Frontal (Fp1, Fp2, F3, F4, F7, F8, FC5, FC6); Temporal (T7, T8); Parietal (P3, P4, P7, P8) and Occipital (O1, O2).

**Neurosky Mindwave mobile:** This single-channel wireless device is a low-cost, dry EEG headset, capable of transmitting EEG signals from electrodes of interest via Bluetooth to smartphone [7]. The headset consists of a

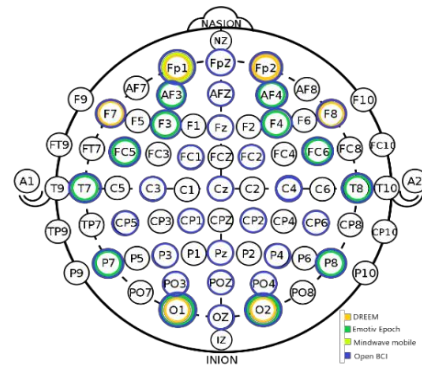


Fig. 2: Electrode map for the four dry EEG devices

single electrode over Frontal lobe (Fp1) on forehead above left eye.

**OpenBCI Ultracortex Mark IV:** This device samples up to 16 EEG channels using dry EEG sensors with setup time almost similar to a wet EEG system. It is capable of recording brain electrical activity with EEG, muscle activity with EMG (electromyograph) and heart activity with ECG (electrocardiograph) [9].

**A. Motivation for the study**

Lesser number of channels in dry-EEG devices restrict data acquisition to specific brain regions. According to Michel and others (2004), change in brain activity at electrodes of interest produces artefactual activity at all other electrodes irrespective of their position. However, activity at all electrodes cannot be recorded by single or few-channeled devices, preventing analysis of major changes in brain regions proximal to regions of interest. Therefore, there is a need to characterize such devices before their practical implementation in the real world. The aim of our study was to characterize the quality of data collected by one such LCDE - DREEM headband in comparison to near to ideal data, simulated using dipole simulator program of Brain Electrical Source Analysis (BESA) software.

**B. Contributions**

The main contributions of this paper are as follows:

1. To simulate cortical activity in the four brain lobes (shown in Fig. 3a) using BESA simulator by embedding dipoles in a few electrode positions to localize the corresponding source of activity in the brain. This is required for illustrating the combinations of minimum electrodes that can be used for studying neural activity evoked by the psychological test-specific cognitive functions and organize a list of tests which can use devices containing channels in region of interest.
2. To devise a methodology for comparison between EEG

signals collected by the DREEM headband and standard noise-free signals simulated using BESA simulator at frontal and occipital lobes of the brain, for calibration of data quality derived from DREEM headband in comparison to the simulated dataset based upon source localization method.

## II. MATERIALS

### A. Study resources

**DREEM headband ©DREEM 2021:** The DREEM device is a wireless headband-like EEG device that records electrical signals produced in brain during different stages of sleep without requiring any external connections. It records brain cortical activity with 5 (+1 ground) dry electrodes and provides 7 derivations (FpZ-O1, FpZ-O2, FpZ-F7, F8-F7, F7-O1, F8-O2, FpZ-F8). The sampling frequency is 250 Hz and the signals are bandpass filtered at 1Hz–30 Hz.

**Brain Electrical Source Analysis (BESA):** This dipole simulator program produced by Patrick Berg allows simulation of evoked or induced brain activity [10]. BESA dipole simulator allows dipole approximation or modelling [11], [12] which simulates electrical activity similar to that generated by partial depolarization of pyramidal neurons in the brain. Dipoles in the brain as shown in Fig. 3 (b) are caused by charge separation in neurons during flow of electrical charges for information signaling [13].

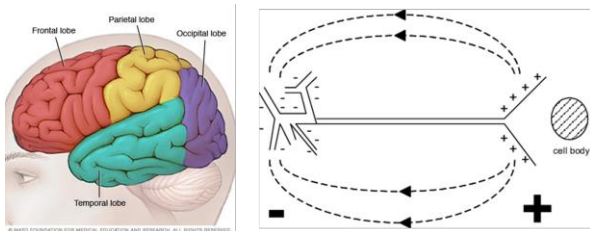


Fig. 3. (a) The four lobes of brain: Frontal, Parietal, Temporal and Occipital. Source: Mayo Foundation. (b) A dipole model generated at the apical dendrite tree.

## III. PILOT STUDY: SIMULATION

### A. Simulation procedure

Fig. 2 is an electrode map representing all electrode positions covered by the four LCDEs discussed in Section I. We selected only few major electrode positions out of all available data for all four lobes and simulated activity using minimum two dipoles and maximum six dipoles to describe the corresponding source localization in each brain lobe. Positions of dipoles placed in the brain lobes during simulation process were: Frontal lobe - Fp1, Fp2, Fpz, F3, F4, F7, F8, Parietal lobe - Pz, P3, P4,

Temporal lobe - T5, T6 and Occipital lobe - O1, O2.

### B. Simulation results

The simulated waveforms for dipoles embedded in four brain lobes were imported in BESA software for spatial analysis using 1) current source density maps, which depict surface activity averaged over short segments of time (shown in Fig. 4c), and 2) distributed imaging method called Classical LORETA Analysis Recursively Applied (CLARA) which is an iterative application of sLORETA technique of source analysis (shown in Fig. 4b) [14]. Resulting surface activity for frontal lobe simulation is represented as a colormap depicting regular activity in and near frontal regions of the head model, depicted in Fig. 4c showing six surface activity maps for 30 seconds time duration. The source analysis for the frontal lobe simulation is represented in Fig. 4b in which source activity specific heightened power at location of simulation i.e., frontal region of the brain can be clearly seen. This shows that similar simulation procedure can be repeated for channels in any dry EEG device to estimate the region of resulting activation to compare whether the device is able to identify the activation in the region of interest. We have created a list of possible psychological tests that could be performed using the available LCDEs after applying similar simulations in some regions. We have generalized the solution by using source localization technique as most researchers prefer deeper cortical analysis due to its time independent nature. Another reason to use source localization technique as the major tool is because this study aims to give details on source of activation produced as a result of cognitive functions evoked by different psychological tests. Thus, in Table I, we have summarized a list of relevant LCDEs (amongst four devices studied under this project as shown in Fig. 1 that can be implemented with major psychological tests based on relevant cognitive functioning involved and corresponding region of brain activated (as suggested by past studies).

## IV. COMPARITIVE STUDY: METHODOLOGY

### A. Data collection and pre-processing

**Experimental Procedure:** Task-related brain activity was recorded using DREEM headband device on a human subject (with no recent neuropsychological or visual disorder history) for 4 minutes while the subject was involved in a basic visual-cognitive task called Tower of London task which induces activity located in frontal region (as it requires progressive planning and decision making) and occipital region (since it is a visual task, it requires active visual perception) of the brain. The distribution of six electrodes in the device follows the 10-20 international system of electrode placement: channels Fp1, Fp2 (reference channel), F7, F8 in frontal region and O1, O2 in occipital region are present. The recorded

TABLE I  
DRY EEG DEVICES FOR COGNITIVE TESTING

TASKS	LOBES	COGNITIVE FUNCTIONS	ELECTRODES	DEVICES
Stroop task	Right prefrontal cortex [16]	Executive functions; visuospatial processing, colour determination, sustained attention	Frontal: Fp1, Fpz, F7, F8, F3, F4, FC5, FC6; Occipital: O1, O2	DREEM Headband, Emotiv epoc+
Number-letter task	Orbital frontal lobe, dorsolateral prefrontal cortex, and posterior parietal cortex [17]	Visualization of the verbal information, working memory	Frontal: Fp1, Fp2, AF3, AF4, Fpz, AFz, Fz, F7, F8, C3; Parietal: Cz, C4, CP5, CP1, CP2, CP6, Pz, P7, P8, P3, P4	Open BCI
Letter-memory task	Lateral prefrontal cortex [18]	Spatial and nonspatial working memory, visualization	Frontal: Fp1, Fp2, F3, F4, F7, F8, FC5, FC6; Occipital: O1, O2	Emotiv epoc+
Anti-saccade task	Frontal lobe (dlPFC-dorsolateral prefrontal cortex) [19]	Working memory, executive functions, and intelligence	Frontal: F3, F4, Fp1, Fp2, F3, F4, F7, F8, FC5, FC6 [Normal Electrical Activity of the Brain in Obsessive-Compulsive Patients After Anodal Stimulation of the Left]	Emotiv epoc+
Wisconsin card sorting task	Frontoparietal [20]	Set shifting, task switching, working memory and inhibitory control	Frontal: Fp1, Fp2, F3, F4, F7, F8; Parietal: P3, P4, P7, P8	Emotiv epoc+
Tower of hanoi	Frontal	Goal-subgoal conflict resolution, working memory [21]	Frontal: Fp1, Fpz, F7, F8, F3, F4, FC5, FC6; Occipital: O1, O2	DREEM Headband, Emotiv epoc+
Hooper visual organization test (HVOT)	Frontal (precentral gyrus), parietal and occipital [22]	Executive functioning, lexical retrieval, visuospatial processing	Frontal: Fp1, Fpz, F7, F8, F3, F4, FC5, FC6; Parietal: Cz, C4, CP5, CP1, CP2, CP6, Pz, P7, P8, P3, P4; Occipital: O1, O2, PO3, PO4, POz,	Open BCI
Clock drawing task – clox (1 and 2)	Bilateral frontal, occipital and parietal lobes [23]	Visuospatial processing, executive function, semantic memory, and planning	Frontal: Fp1, Fpz, F7, F8, F3, F4, FC5, FC6; Parietal: Cz, C4, CP5, CP1, CP2, CP6, Pz, P7, P8, P3, P4; Occipital: O1, O2, PO3, PO4, POz,	Open BCI, Emotiv epoc+
D2 test	Frontal [24]	Individual attention and concentration performance	Frontal: Fp1, Fp2, F7, F8; Occipital: O1, O2	Neurosky mindwave mobile, DREEM Headband
Target word search (WS task)	Frontal, occipital [25]	Visual processing, logical reasoning, problem-solving	Frontal: Fp1, Fp2, F3, F4, F7, F8, FC5, FC6; Parietal: P3, P4, P7, P8; Occipital: O1, O2	Emotiv epoc+
Trail-making test A&B	Frontal cortex [26]	Attention-related functions	Frontal: Fp1, Fp2, F7, F8; Occipital: O1, O2	Neurosky mindwave mobile, DREEM Headband
Visual and auditory continuous performance test (IVA)	Frontal, parietal and occipital	Vigilance, auditory focus, auditory speed, auditory consistency, visual focus, visual speed, visual prudence, and visual consistency [27]	Frontal: Fp1, Fpz, F7, F8, F3, F4, FC5, FC6; Parietal: Cz, C4, CP5, CP1, CP2, CP6, Pz, P7, P8, P3, P4; Occipital: O1, O2, PO3, PO4, POz,	Open BCI

List of psychological tests along with the cognitive functions and region of activation in brain corresponding to them (as suggested by past studies). Using results of source analysis, minimum number of electrodes that can identify neural activation in the tests are suggested along with a suitable LCDE which is both easily accessible and can provide quality result.

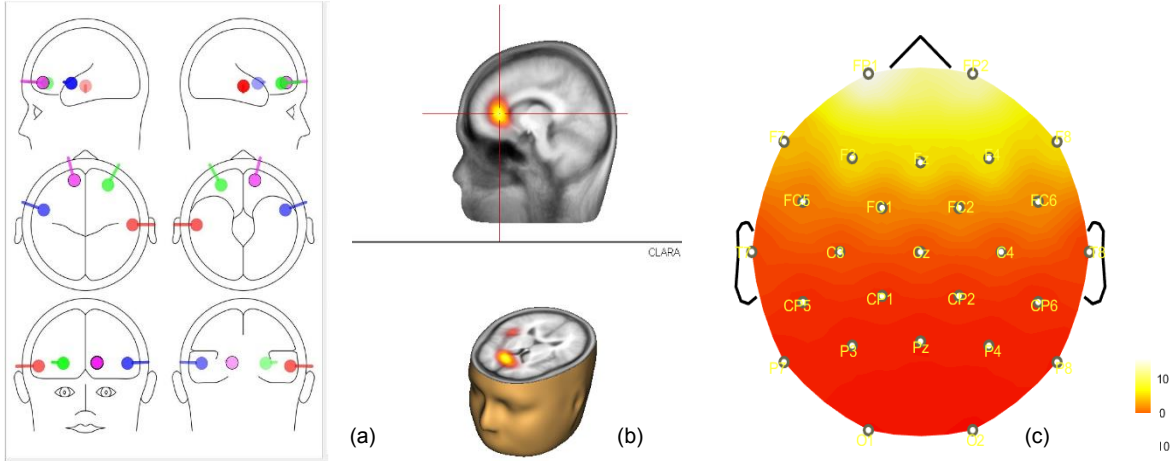


**Fig. 4 (a): Frontal lobe: dipoles embedded in frontal region of head model. (b) Source localization depicting activation in frontal lobe. (c) Cortical or surface activity colormap for dataset simulated for dipoles placed at frontal lobe depicting heightened surface activity over frontal region of brain.**

dataset was imported in BESA for artefact identification through its automatic pattern search tool for identifying regular eye blinks and cardiac activity and removing them for artefact reduction. For noise filtering, the dataset was band passed at 0.1 Hz – 30 Hz for specifying frequency content of the signals.

**B. Simulation of model dataset**

The previous section (Section III) illustrated the inverse mapping feature of artificial dipole placement using BISA dipole simulator. Six artificial dipoles were seeded in a head model at electrode positions same as that of DH to simulate signals at varying noise levels for comparison with DREEM signals: (a) noise-free, (b) rms noise voltage: 0.2  $\mu$ V, (c) rms noise voltage: 0.4  $\mu$ V, (d) rms noise voltage: 0.6  $\mu$ V and (e) rms noise voltage: 0.8  $\mu$ V datasets. For application of this tool, we identified the MNI coordinates (Montreal Neurological Institute template of EEG coordinate system) of all six electrode positions exhibited by DREEM Headband for simulation in a standard head model in frontal and occipital region of the model.

**C. Comparison of noise sensitivity level in simulated dataset(s)**

Noise sensitivity for EEG-like signals can be determined by several methods. The mathematical concept used in this study to determine noise sensitivity is derived using localization error resulting from source analysis of model dataset simulated at different noise levels. Here, the localization error states the difference between the localized source for noise-free dataset and noisy dataset (at different noise levels), both simulated using BESA dipole simulator program. Steps followed for measuring noise sensitivity level of model dataset(s) are: (1) source

analysis using CLARA technique of localization was performed in BESA software (2) the resulting MNI coordinates for highest amplitude source localized by the software were calculated (3) using the MNI coordinates, localization error  $\llbracket \epsilon \rrbracket$  was calculated based on Eq. (1) as used in previous studies [14] in MATLAB 2020a.

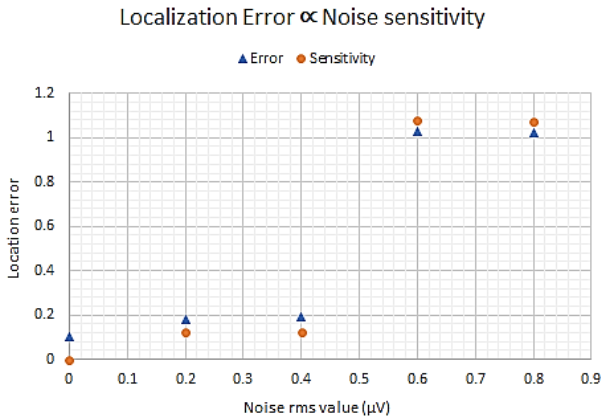


**Fig 5. Noise sensitivity (represented by orange circles) for model datasets with different noise levels with respect to noise-free dataset and localization error (represented by blue triangles) for model datasets with different noise levels with respect to dry EEG data.**

$$\epsilon = \sqrt{(x^1 - x^2)^2 + (y^1 - y^2)^2 + (z^1 - z^2)^2} \quad (1)$$

The resulting noise sensitivity for various model datasets is represented in Fig. 5. The graph in Fig. 5 shows that there is an increasing trend in noise sensitivity with increasing noise level in model dataset, starting with minimal noise sensitivity in model dataset (b) and (c) as 0.122 and 0.126 respectively, drastically increasing to 1.077 and 1.071 in model dataset (d) and (e).

## V. RESULTS

### A. Comparative analysis between DREEM dataset and simulated model dataset

For comparison with dry EEG data recorded using DREEM Headband, we selected the noise-free model dataset amongst all the datasets simulated using BESA dipole simulator program. Both the comparison datasets were free of artefacts and were passed through a band-pass filter for normalization purpose. The method for comparison included source analysis in BESA software to compare the localized source in both datasets and determine the level of localization error to establish a correlation between both the datasets. The source analysis technique used was CLARA which is Classical LORETA Analysis Recursively Applied since localization error is minimum in sLORETA amongst all source analysis techniques [15].

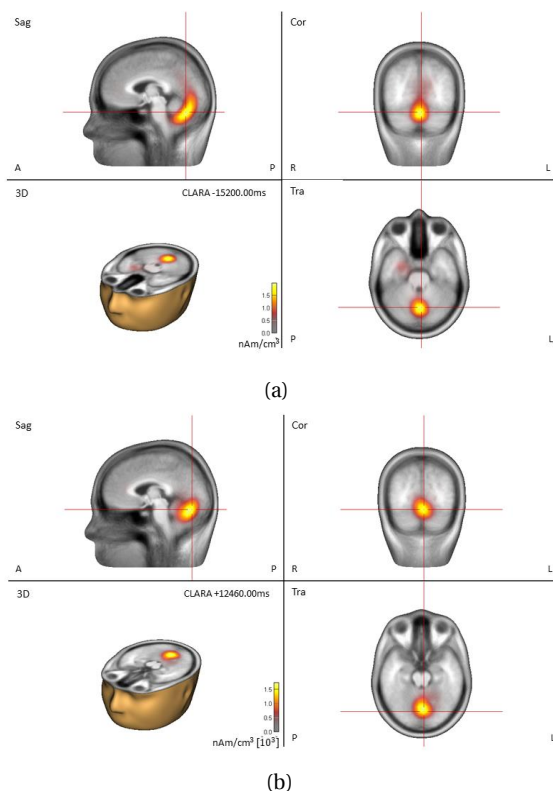


**Fig. 6. Source localization for comparative analysis between (a) Noise-free model dataset simulated in BESA dipole simulator program and (b) Dry EEG dataset recorded using DREEM Headband**

The localized source for both comparable datasets can be seen in Fig. 6 and the localization error between the two sources, calculated using Eq. (1) comes out to be 0.1871 depicting minimal level of deviation between the two localized sources. However, amplitude scale in both

datasets is differentiable as can be seen in scale units of Fig. 6a and b, clearly showing amplitude difference on a scale of  $10^3$ nAm. The difference occurs due to several factors discussed in further sections.

## VI. DISCUSSION

The results of the comparative study shows that a dry EEG data in its processed state (i.e., computational artefactual corrections applied), is comparable with an artificially simulated noise-free data with a minimal localization error of 10%. Simultaneously, it must be noted that noise sensitivity based on amplitude is larger in dry EEG dataset by a scale of  $10^3$  nAm as compared to noise-free model dataset. This indicates that even though the dry EEG dataset is affected by environmental noise, muscle movement or electrical disturbances from equipment in surroundings, they are reliable sources of measure of brain activity in cognitive studies. A more important conclusion of this study is a reference chart of psychological tests suggesting the number and position of EEG electrodes that can be used in further cognitive studies that aim to identify source of activation in the brain pertaining to the cognitive function involved in the tests, along with a list of preferred dry EEG devices to us.

## VII. CONCLUSION

Field studies performed outside sophisticated lab environments require the use of less sensitive, portable and low-cost neurophysiological monitoring equipment. However, the data quality might be affected because of ruthless environment of monitoring, so the proposed method of comparative analysis in this study could be a good calibration methodology for characterizing any brain activity signals recorded using LCDEs before their real-world implementation to account for the quality of data recorded using the devices.

*Limitations of the study:* Future studies could use wet EEG data for comparison with Dry EEG data and model dataset for finding the correlation between datasets recorded using wet EEG, dry EEG and model data simulated using BESA simulator.

## REFERENCES

- [1] LaRocco, J., Le, M. D., & Paeng, D. G. (2020). A systemic review of available low-cost EEG headsets used for drowsiness detection. *Frontiers in Neuroinformatics*, 14.
- [2] Puce, A., & Hämäläinen, M. S. (2017). A review of issues related to data acquisition and analysis in EEG/MEG studies. *Brain Sciences*, 7(6), 58.
- [3] Arnal, P. J. et al. (2020). The Dreem Headband compared to polysomnography for electroencephalographic signal acquisition and sleep staging. *Sleep*, 43(11), zsaa097.
- [4] Johnstone, S. J., Jiang, H., Sun, L., Rogers, J. M., Valderrama, J., & Zhang, D. (2021). Development of frontal EEG differences between eyes-closed and eyes-open resting conditions.

- ions in children: data from a single-channel dry-sensor portable device. *Clinical EEG and Neuroscience*, 52(4), 235-245.
- [5] Radüntz, T. (2018). Signal quality evaluation of emerging EEG devices. *Frontiers in Physiology*, 9, 98.
- [6] Badcock, N. A., Mousikou, P., Mahajan, Y., De Lissa, P., Thie, J., & McArthur, G. (2013). Validation of the Emotiv EPOC® EEG gaming system for measuring research quality auditory ERPs. *PeerJ*, 1, e38.
- [7] Doudou, M., Bouabdallah, A., & Cherfaoui, V. (2018). A loud on physiological sensors for efficient driver drowsiness detection system. *Sensors & Transducers Journal*, 224(8), 39-50.
- [8] Skukies, R., Jentoft, E., Asko, O. (2020). 'International 10-20 system for EEG electrode placement' [Online]. Available: [Electrode Placement - Department of Psychology \(uio.no\)](#)
- [9] Mohamed, F., Nataraj, S. K., Ahmed, S. F., & Yaacob, S. (2018). An approach in determining fatigueness and drowsiness detection using EEG. *Res. Inventy Int. J. Eng. Sci*, 8(3), 20-28.
- [10] Berg, P., & Scherg, M. (1994). A fast method for forward computation of multiple-shell spherical head models. *Electroencephalography and clinical Neurophysiology*, 90(1), 58-64.
- [11] Litt, B. (1991). Dipoles and the EEG. *American Journal of EEG Technology*, 31(2), 119-121.
- [12] Miltner, W., Braun, C., Johnson Jr, R., Simpson, G. V., & Ruchkin, D. S. (1994). A test of brain electrical source analysis (BESA): A simulation study. *Electroencephalography and Clinical Neurophysiology*, 91(4), 295-310.
- [13] Salvetti, A., & Wilamowski, B. M. (2008, May). A brain-computer interface for recognizing brain activity. In 2008 Conference on Human System Interactions (pp. 714-719). IEEE.
- [14] Khemakhem, R., Kammoun, I., Chtourou, K., Boughariou, J., Ghorbel, M., & Hamida, A. B. (2017, May). EEG localization error exploration vs distance between sources. In 2017 International Conference on Advanced Technologies for Signal and Image Processing (ATSIP) (pp. 1-5). IEEE.
- [15] Pascual-Marqui, R. D. (2002). Standardized low-resolution brain electromagnetic tomography (sLORETA): technical details. *Methods Find Exp Clin Pharmacol*, 24(Suppl D), 5-12.
- [16] Vendrell, P., Junqué, C., Pujol, J., Jurado, M. A., Molet, J., & Grafman, J. (1995). The role of prefrontal regions in the Stroop task. *Neuropsychologia*, 33(3), 341-352.
- [17] Haut, M. W., Kuwabara, H., Leach, S., & Arias, R. G. (2000). Neural activation during performance of number-letter sequencing. *Applied Neuropsychology*, 7(4), 237-242.
- [18] Owen, A. M., Stern, C. E., Look, R. B., Tracey, I., Rosen, B. R., & Petrides, M. (1998). Functional organization of spatial and nonspatial working memory processing within the human lateral frontal cortex. *Proceedings of the National Academy of Sciences*, 95(13), 7721-7726.
- [19] Klein, C., Rauh, R., & Biscaldi, M. (2010). Cognitive correlates of anti-saccade task performance. *Experimental Brain Research*, 203(4), 759-764.
- [20] Buchsbaum, B. R., Greer, S., Chang, W. L., & Berman, K. F. (2005). Meta-analysis of neuroimaging studies of the Wisconsin Card-Sorting task and component processes. *Human Brain Mapping*, 25(1), 35-45.
- [21] Goel, V., & Grafman, J. (1995). Are the frontal lobes implicated in "planning" functions? Interpreting data from the Tower of Hanoi. *Neuropsychologia*, 33(5), 623-642.
- [22] Jefferson, A. L., Wong, S., Bolen, E., Ozonoff, A., Green, R. C., & Stern, R. A. (2006). Cognitive correlates of HVOT performance differ between individuals with mild cognitive impairment and normal controls. *Archives of Clinical Neuropsychology*, 21(5), 405-412.
- [23] Talwar, N. A. et al. (2019). The neural correlates of the clock-drawing test in healthy aging. *Frontiers in Human Neuroscience*, 13, 25.
- [24] Brickenkamp, R., & Zillmer, E. (1998). *The d2 test: A timed test of selective attention. Göttingen, Germany: Hogrefe.*
- [25] Fockert, J. D., Rees, G., Frith, C., & Lavie, N. (2004). Neural correlates of attentional capture in visual search. *Journal of Cognitive Neuroscience*, 16(5), 751-759.
- [26] Müller, L. D. et al. (2014). Neural correlates of a standardized version of the trail making test in young and elderly adults: a functional near-infrared spectroscopy study. *Neuropsychologia*, 56, 271-279.
- [27] Tinus, T. P. (2003). The integrated visual and auditory continuous performance test as a neuropsychological measure. *Archives of Clinical Neuropsychology*, 18(5), 439-454.
- [28] "DREEM Headband," ©DREEM 2021 [Online]. Available: <https://dreem.com/>
- [29] "Neurosky Mindwave Mobile," © 2015 NeuroSky, [Online]. Available: <https://neurosky.com/>
- [30] "Emotiv epoc+," © UX Themes, [Online] Available: <https://www.emotiv.com/>
- [31] "OpenBCI Ultracortex Mark IV," © 2021 OpenBCI, [Online]. Available: [www.openbci.com](http://www.openbci.com).

# Extractive Lecture Summarization Evolutionary Algorithms – Optimizing Word, Sentence and Text Features

Binathi Bingi\*, Lotika Singh

Department of Physics and Computer Science,  
Dayalbagh Educational Institute, Agra, 282005, India

*Automatic extractive text summarization on lectures has become more predominant with increase in online learning. These systems help in collecting important information, key phrases and sentences that best describe the lecture transcript. In this paper, we have proposed automatic extractive lecture summarization as an optimization problem, and Non-dominated Sorting Genetic Algorithm (NSGAI) is employed to solve this. The possible set of sentences that form the summary are encoded as solutions of GA and are evaluated based on word, sentence, and text features. These features constitute the objective functions that measure different aspects of the summary and are optimized simultaneously using the search capability of GA. For evaluation of the model, two summarization datasets DocEng'19 and CNN/Daily mail are used. The results are compared with optimization, machine learning and deep learning models using ROUGE (Recall-Oriented Understudy for Gisting Evaluation, which serves as a metric for evaluating automatic summarization) measures. The paper also demonstrates the effect of similarity measures and objective functions over the quality of the generated summary.*

**Keywords** – Lecture summarization system, Multi-objective binary optimization, Extractive summarization, Sentence, Text quality measures.

## I. INTRODUCTION

Text summarization aims to create a shorter version of the document that conveys the main theme of the document [1]. Based on the extraction methodology, there are two types of summarization techniques – abstractive [2] and extractive [3]. Abstractive summarization uses vocabulary beyond the specified text, generates a summary like human generated summary. To accomplish this it requires deep learning, high computation power and highly complex algorithms with limited generalization [4]. Due to these challenges, extractive summarization is used by lecture summarization models. Extractive summarization leverages only the content from the text. It chooses key phrases and important sentences from the text to create a summary of desired length. In education, with increase in (Massive Open Online Courses) MOOCs, video lecture transcripts are available but locating the important information from the Lecture transcript (L) can be a challenging task. In such cases, automatic extractive summarization of lectures is a powerful tool. In the beginning of the 21st century, manual summarizations were created using multimedia applications [5]. With increase in the data, manual summarization became a tedious process and probabilistic models were

used for summarization [6]. To improve performance, researchers incorporated rhetorical information into the summaries [7]. In recent years, different methods like meta-heuristic based [8]-[10], unsupervised learning based [11], [12], supervised learning based [13], [15] neural-network based [4], [16], [19] have been used to solve the problem of extractive summarization. Deep learning techniques require huge computational resources and training data, on the contrary meta-heuristic algorithms are unsupervised and can optimize multiple features to generate good quality summary using comparatively less computational resources and training data.

There are four methods used for generating summary features [20]: (i) word scoring (ii) sentence scoring (iii) graph scoring (iv) text scoring. In this paper, we have used a combination of word, sentence and text scoring features to create five objective functions and formulated the lecture summarization problem as a multi-objective optimization problem. To show that the performance of model depends on the objective functions and similarity/dissimilarity function chosen, different combinations of the above have been explored. For reporting the best summary and evaluation of the model, most of the approaches use gold standard summaries, but in real scenarios like lecture summarization, gold standard references might not be available. To overcome this, we have explored unsupervised learning techniques to choose a

---

\* Corresponding author: b.binathi@gmail.com  
ISSN 0972-5032 (P); Copyright ©2022, SSI

single optimal solution from a set of solutions generated by NSGA-II [21].

## II. LECTURE SUMMARIZATION MULTIOBJECTIVE SUMMARIZATION

Multi-objective optimization problem optimizes more than one objective function simultaneously by adhering to some constraints to solve a particular problem. Genetic Algorithm (GA) is a search-based global optimization technique proposed by John Holland in 1975 [22]. Based on the representation of solutions, there exists two variants of GA – binary-coded and real-coded. In this paper, we use binary-coded vectors to represent the solutions and five objective functions are associated with each solution. The algorithm executes in a way like other optimization algorithms. It starts with population - a random set of solutions. For each solution, the offspring is generated using crossover and mutation operations [23], [24] and solution is evaluated in comparison with all solutions in the population.

### A. Problem Definition

Consider a Lecture transcript (L) consisting of N sentences,  $\{s_1, s_2, \dots, s_N\}$ . Our task is to find the subset of sentences (S) which cover the information in the lecture,  $S \in L$  such that

$$|S| \leq S_{max} \quad (1)$$

where  $S_{max}$  represents the maximum number of sentences in the summary and  $|S|$  represents the number of sentences in the generated summary.

### B. Sentence similarity/dissimilarity and quality measures

To generate a high-quality summary, five objective functions are optimized simultaneously using binary genetic algorithm and NSGA-II framework. In this paper, we have analyzed three similarity/dissimilarity measures that are included in the objective functions and their description follows:

#### 1. Normalized Google Distance (NGD)

It measures the dissimilarity between two sentences using the terms in the sentences [25]. It is mathematically defined as:

$$d(s_i, s_j) = \frac{\sum_{t_i \in s_i} \sum_{t_j \in s_j} NGD(t_1, t_2)}{|s_i| * |s_j|} \quad (2)$$

where,  $t_1$  and  $t_2$  are words belonging to sentences  $s_i$  and  $s_j$  respectively,  $|s_i|$ ,  $|s_j|$  are word count in sentences  $s_i$  and  $s_j$  respectively.

$$NGD(t_1, t_2) = \frac{\max\{\log(s_{t_1}), \log(s_{t_2})\} - \log(s_{t_1, t_2})}{\log N - \min\{\log(s_{t_1}), \log(s_{t_2})\}} \quad (3)$$

Where  $s_{t_1}$ ,  $s_{t_2}$  represent number of sentences in L containing the word  $t_1$  and word  $t_2$  respectively,  $s_{t_1, t_2}$  represents the number of sentences in L containing both the words  $t_1$  and  $t_2$ , N is the number of sentences in L.

#### 2. Word Mover Distance

This measure calculates the dissimilarity between two documents. It is a distance measure between embedded words of one document and to the other document [26].

#### 3. Cosine Similarity

It is a similarity measure that calculates the cosine angle between two non-zero vectors [25]. The vectors are generated using Word2vec model [27].

### C. Objective functions – word feature, sentence feature, text feature

To obtain a good summary, selection of good objective functions is important. The set of objective functions used in this paper are sentence score, sentence length, coverage, cohesion, readability. The first objective function is a combination of word features and motivated by the paper [20]. Text feature – sentence length and sentence features – cohesion, coverage, readability form the remaining four objective functions. We provide a brief description of the functions below:

#### 1. Word Feature

Word features help us decide the importance of a sentence and is a weighted combination of title word, thematic word, keyword, proper noun, numerical and term weight.

##### a) Title word

Sentences that contain title words indicate the subject of the transcript. Score of the title words is calculated as

$$Title\_Score(w_{ij}|Title) = 5/15 \quad (4)$$

where,  $w_{ij}$  is the word  $i$  in sentence  $j$ . The above equation indicates if the word  $i$  in sentence  $j$  is one of the title words, then a score of 5/15 is assigned to it.

##### b) Thematic word

The thematic words of L are computed using Latent Dirichlet Allocation (LDA) algorithm [28]. The sentence that contains theme words is most likely to represent theme of the transcript.

$$Thematic\_Score(w_{ij}|Thematic\ word) = 4/15 \quad (5)$$

where,  $w_{ij}$  is the word  $i$  in sentence  $j$ . If word  $i$  is one of the thematic words, then a score of 4/15 is assigned to it.

c) *Keyword*

The keywords are determined using tf-idf measure. The score is calculated as, if the word  $i$  of sentence  $j$  is a keyword, then a score of 3/15 is allocated to it.

$$Keyword\_Score(w_{ij}|Keyword) = 3/15 \quad (6)$$

d) *Proper Noun*

The sentences in the transcript that contain more proper nouns have a higher probability to be included in the summary. If a word  $i$  in sentence  $j$  is a proper noun, then a score of 2/15 is assigned to it.

$$Propernoun\_Score(w_{ij}|Propernoun) = 2/15 \quad (7)$$

e) *Numerical data*

Sentences containing numerical data might be significant and are assigned the below score.

$$Numeric\_Score(w_{ij}|Numeric) = 1/15 \quad (8)$$

where,  $w_{ij}$  word  $i$  in sentence  $j$ . If  $w_{ij}$  is a number, then a score of 1/15 is assigned to it.

f) *Term weight*

The frequency of the word occurring in the transcript can be used to compute the importance of sentence. The term weight score is calculated as below:

$$w_{ij} = \frac{TF}{IDF} = \left( \frac{\log(1 + tf)}{\log(df)} \right) \quad (9)$$

$$TW_{Score}(w_{ij}) = \frac{\sum_{i=1}^k W_i(s_j)}{\text{Max}(\sum_{i=1}^k W_i(s_j^N))} \quad (10)$$

The first objective function, sentence score of a sentence ( $s_j$ ) is calculated as the sum of the above word features.

$$S\_Score(s_j) = \sum_{i=1}^N (Title_{Score}(w_{ij}) + Thematic_{Score}(w_{ij}) + Keyword_{Score}(w_{ij}) + Propernoun_{Score}(w_{ij}) + Numeric_{Score}(w_{ij}) + TW_{Score}(w_{ij})) \quad (11)$$

where,  $w_{ij}$  is  $i^{th}$  word in sentence  $j$ ,  $N$  is the total number of words in sentence  $j$ .

1) *Sentence Feature*

a) *Sentence Length*

Shorter sentences have less chance to appear in the summary [29]. Normalized sigmoid function [30] is used to calculate the sentence length score.

$$SL\_Score = \sum_{\forall s_i \in Summary} \frac{1 - \exp\left(\frac{-l(s_i) - \mu(s)}{std(s)}\right)}{1 + \exp\left(\frac{-l(s_i) - \mu(s)}{std(s)}\right)} \quad (12)$$

where,  $std(s)$  is the standard deviation of length of sentences,  $l(s_i)$  is the length of the sentence  $s_i$ , the average length of sentences in the summary is represented as  $\mu(s)$ . The next three objective functions are based on text features – cohesion, coverage, and readability.

2) *Text Feature*

a) *Cohesion*

The relatedness of the sentences in the summary is measured using cohesion [31] and is defined as:

$$COH\_Score = \frac{\log(A_s * 9 + 1)}{\log(M * 9 + 1)} \quad (13)$$

where,

$$A_s = \frac{\sum_{\forall s_i, s_j \in Summary} sim(s_i, s_j)}{O_s} \quad (14)$$

$$O_s = \frac{N * (N - 1)}{2} \quad (15)$$

$$M = \max sim(s_i, s_j), i, j \leq N \quad (16)$$

b) *Coverage*

It measures the extent to which the summary provides information about the transcript [8].

$$Cov\_Score = \sum_{\forall s_i \in Summary} \sum_{\forall s_j \in L, s_i \neq s_j} \frac{sim(s_i, s_j)}{N - 1} \quad (17)$$

c) *Readability*

Readability, measures similarity of each sentence to that of its previous sentence. Optimizing this objective function to be maximum ensures that two consecutive sentences are related to each other thereby making the generated summary readable [9].

$$R\_Score = \sum_{i=2}^{|N|} sim(s_i, s_{i-1}) \quad (18)$$

### III. EXTRACTIVE LECTURE SUMMARIZATION USING MULTI-OBJECTIVE GENETIC ALGORITHM

In this paper, we have experimented with different combinations of objective functions as well as similarity/dissimilarity functions to identify the best suitable combination. To calculate ROUGE score, a standard reference or gold summary is used but which might not be readily available in real-life situations like summarizing a lecture transcript. In cases where the reference summary is available, supervised information can be used to select the best solution. In situations where the reference summary is not present unsupervised learning approaches like ensemble approach is used [9]. In the ensemble approach, all the sentences from all the corresponding summaries of the rank-1 solutions of final Pareto front are arranged as per the frequency of occurrence. The summary is generated by adding sentences from the pool one after the other until it reaches the desired summary length. The proposed approach is evaluated on two datasets – CNN dataset [32] and CNN/Daily Mail [33] dataset. A brief description is shown in Fig.1.

TABLE I  
BRIEF DESCRIPTIONS OF DATASETS USED

	CNN	CNN/Daily Mail
#Documents	50	11,590 (Test data)
Source	DocEng' 19	CNN/Daily Mail
Length of summary	10% x DocSent	3.75 sentences on average

#DocSent is the number of sentences in the document

### IV. RESULTS AND DISCUSSIONS

Our proposed approach is implemented using the three similarity/dissimilarity functions discussed in the above sections to understand their impact. From Fig. 1, it is observed that (Word Mover's Distance) WMD similarity measure provides better results compared to the other functions on the CNN dataset. It can be concluded that using different similarity/dissimilarity measures can help in improving the performance. WMD helps in capturing semantic relationships between sentences which could be one of the reasons for an improved performance. Our approach with WMD similarity measure was implemented on CNN dataset with a combination of different objective functions and the results can be seen in Fig. 2. From Table II, we can notice that optimizing word, sentence text features-based objectives simultaneously yield a better summary than other approaches.

Based on Table II and Fig. 1, it is observed that best summary is generated using all the objective functions

and WMD as similarity measure. Our approach with WMD and all objective functions is tested on CNN/Daily Mail dataset using ROUGE1 F-measure and the results are as shown in Fig. 3. Even though the objective functions used in our approach – coverage and readability exhibit conflicting behaviors as coverage is an extrinsic measure and readability is an intrinsic measure our model yielded results comparable to the state-of-the-art models. Considering all the objective functions with WMD as similarity measure, from Fig. 2 our model performed better than the extractive summarization models (PGN [34], DCA [35], REFRESH [32], NEUSUM [19]) and performed almost equally to deep learning based abstractive summarization models (Transformers, BERT). As in case of any multi-objective optimization, though objective functions are conflicting in behavior, using all the objective functions we were able to capture features at word, sentence and text level. Semantic information is captured using WMD measure.

### V. CONCLUSION

A lecture summarization model is an effective learning tool for students. Although, the lecture summarization approach used in this paper has some limitations, it provided an improvement in quality when compared to most of the other dated approaches. The model eliminates the need for large training datasets and high computation power. The model leaves scope for improvement in areas like automatically determining the length of the summary to be generated, objective functions and similarity/dissimilarity functions.

### REFERENCES

- [1] Hovy, E., & Lin, C.Y. (1997). Automated text summarization and the SUMMARIST system. *Proceedings of Association for Computational Linguistics*, 197–214.
- [2] Gupta, V., & Lehal, G. (2010). A survey of text summarization extractive techniques. *Journal of Emerging Technologies in Web Intelligence*, 2(3), 258–268. <https://doi.org/10.4304/jetwi.2.3.258-268>
- [3] Ganesan, K., Zhai, C., & Han, J. (2010). Opinosis: a graph-based approach to abstractive summarization of highly redundant opinions. *Proceedings of the 23<sup>rd</sup> International Conference on Computational Linguistics*, 340–348.
- [4] Miller, D. (2019). Leveraging bert for extractive text summarization on lectures. In *Computation and Language*. <https://arxiv.org/abs/1906.04165>
- [5] Glass, J., Hazen, T. J., Cyphers, S., Malioutov, I., Huynh, D., & Barzilay, R. (2007). Recent progress in the MIT spoken lecture processing project. *Eighth Annual Conference of the International Speech Communication Association*.
- [6] Murray, G., Renals, S., & Carletta, J. (2005). Extractive summarization of meeting recordings. *9th European Conference on Speech Communication and Technology*, 593–596.
- [7] Hovy, E., & Lin, C.Y. (1997). Automated text summarization and the SUMMARIST system. *Proceedings of Association for Computational Linguistics*, 197–214.

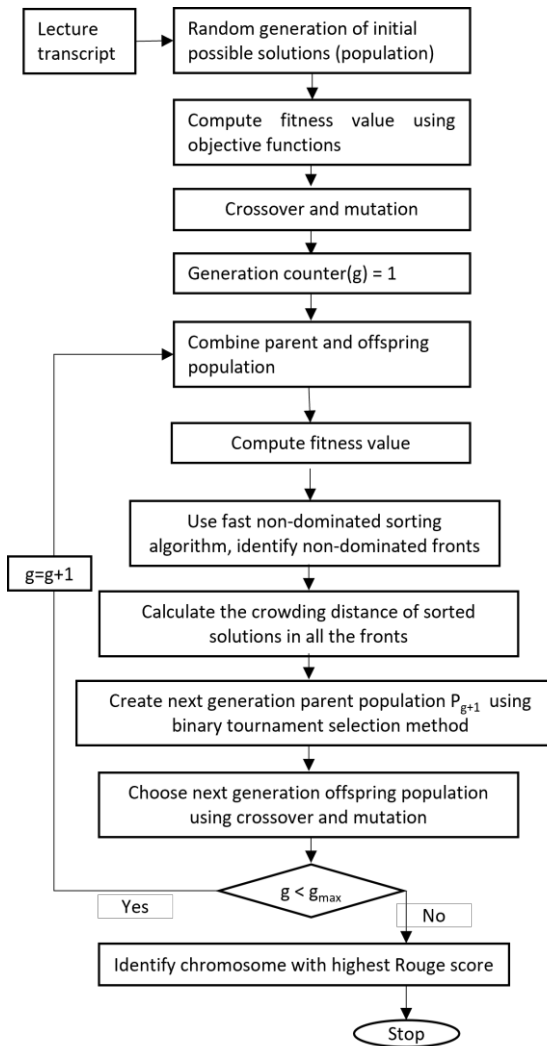


Fig. 1. Algorithm to find the best summary with highest ROUGE score using NSGA-II.

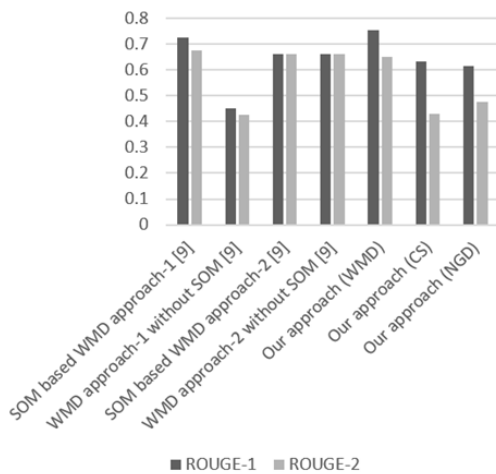


Fig. 2. ROUGE precision scores obtained using different approaches on CNN dataset

TABLE II  
COMPARISON OF ROUGE SCORES OBTAINED USING OUR APPROACH (WMD) WHEN THE OPTIMAL SOLUTION

Strategies	ROUGE-1	ROUGE-2
S_Score	0.43353	0.27312
SL_Score	0.37564	0.13237
CoV_Score	0.35259	0.10192
R_Score	0.43643	0.20468
S_Score and SL_Score	0.58327	0.44284
S_Score and CoV_Score	0.36962	0.12040
S_Score and R_Score	0.61095	0.45969
SL_Score and CoV_Score	0.64692	0.51532
SL_Score and R_Score	0.53142	0.33365
CoV_Score and R_Score	0.4664	0.22977
SL_Score, CoV_Score and R_Score	0.64120	0.53962
All objective functions	0.7559	0.64984
Ensemble approach	0.30302	0.11611

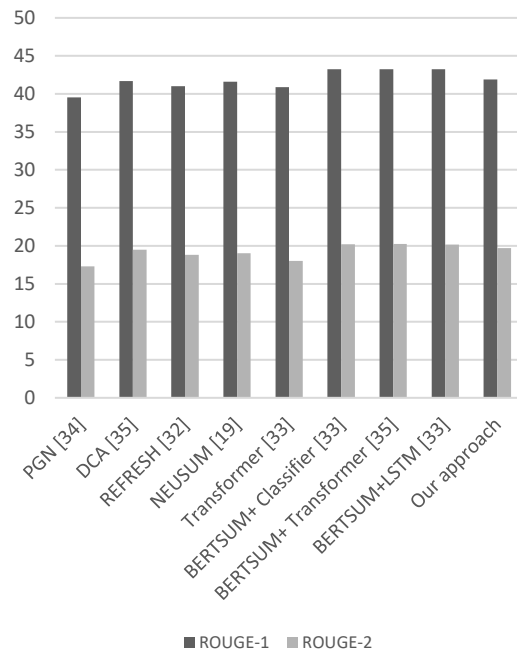


Fig. 3. Comparison of ROUGE scores obtained using our approach (wmd) with state of the art models

- [8] Gupta, V., & Lehal, G. (2010). A survey of text summarization extractive techniques. *Journal of Emerging Technologies in Web Intelligence*, 2(3), 258–268. <https://doi.org/10.4304/jetwi.2.3.258-268>
- [9] Ganesan, K., Zhai, C., & Han, J. (2010). Opinosis: a graph-based approach to abstractive summarization of highly redundant opinions. *Proceedings of the 23<sup>rd</sup> International Conference on Computational Linguistics*, 340–348.
- [10] Miller, D. (2019). Leveraging bert for extractive text summarization on lectures. In *Computation and Language*. <https://arxiv.org/abs/1906.04165>
- [11] Glass, J., Hazen, T. J., Cyphers, S., Malioutov, I., Huynh, D., & Barzilay, R. (2007). Recent progress in the MIT spoken lecture processing project. *Eighth Annual Conference of the International Speech Communication Association*.
- [12] Murray, G., Renals, S., & Carletta, J. (2005). Extractive summarization of meeting recordings. *9th European Conference on Speech Communication and Technology*, 593–596.
- [13] Zhang, J. J., Chan, H. Y., & Fung, P. (2007). Improving lecture speech summarization using rhetorical information. *Automatic Speech Recognition & Understanding*, 195–200.
- [14] Mendozaab, M., Bonillaa, S., Nogueraa, C., Cobosab, C., & León, E. (2014). Extractive single-document summarization based on genetic operators and guided local search. *Expert Systems with Applications*, 41(9), 4158–4169. <https://doi.org/10.1016/j.eswa.2013.12.042>
- [15] Saini, N., Saha, S., Chakraborty, D., & Bhattacharyya, P. (2019). Extractive single document summarization using binary differential evolution: Optimization of different sentence quality measures. *PLoS ONE*, 14(11). <https://doi.org/10.1371/journal.pone.0223477>
- [16] Song, W., Cheon, L. C., Park, S. C., & Ding, X. F. (2011). Fuzzy evolutionary optimization modeling and its applications to unsupervised categorization and extractive summarization. *Expert Systems with Applications*, 38(8), 9112–9121. <https://doi.org/10.1016/j.eswa.2010.12.102>
- [17] Svore, K., Vanderwende, L., & Burges, C. (2007). Enhancing single-document summarization by combining RankNet and third-party sources. *Proceedings of the 2007 Joint Conference on Empirical Methods in Natural Language Processing and Computational Natural Language Learning (EMNLP-CoNLL)*, 448–457.
- [18] Dunlavy, D.M., O’Leary, D.P., Conroy, J.M., & Schlesinger, J.D. (2007). A system for querying, clustering and summarizing documents. *Information Processing & Management*, 43(6), 1588–1605.
- [19] Lafferty, J. D., McCallum, A., & Pereira, F. C. N. (2001). Conditional random fields: Probabilistic models for segmenting and labeling sequence data. *Proceedings of the Eighteenth International Conference on Machine Learning*, 282–289.
- [20] Wan, X., Yang, J., & Xiao, J. (2007). Manifold-Ranking Based Topic-Focused Multi-Document Summarization. *IJCAI’07: Proceedings of the 20th International Joint Conference on Artificial Intelligence*, 2903–2908.
- [21] Oliveira, H., Lins, R. D., Lima, R., Freitas, F., & Simske, S. J. (2017). A regression-based approach using integer linear programming for single-document summarization. *IEEE 29th International Conference on Tools with Artificial Intelligence (ICTAI)*, 270–277.
- [22] Nallapati, R., Zhai, F., & Zhou, B. (2017). Summa-RuNNer: A Recurrent Neural Network Based Sequence Model for Extractive Summarization of Documents. *The Thirty-First AAAI Conference on Artificial Intelligence*, 3075–3081.
- [23] Cheng, J., & Lapata, M. (2016). Neural summarization by extracting sentences and words. *Proceedings of the 54th Annual Meeting of the Association for Computational Linguistics (Volume 1: Long Papers)*, Association for Computational Linguistics, Berlin, Germany, 484–494
- [24] Dong, Y., Shen, Y., Crawford, E., Hoof, H. van, & Cheung, J.C.K. (2018). Banditsum: Extractive summarization as a contextual bandit. *Proceedings of the EMNLP Conference*, 3739–3748. <https://doi.org/10.18653/v1/D18-1409>
- [25] Zhou, Q., Yang, N., Wei, F., Huang, S., Zhou, M., & Zhao, T. (2018). Neural document summarization by jointly learning to score and select sentences. *Proceedings of the 56th Annual Meeting of the Association for Computational Linguistics (Volume 1: Long Papers)*, 654–663. <https://www.aclweb.org/anthology/P18-1061>
- [26] Abbasi-ghalehtaki, R., Khotanlo, H., & Esmaeilpour, M. (2016). Fuzzy evolutionary cellular learning automata model for text summarization. *Swarm and Evolutionary Computation*. <http://dx.doi.org/10.1016/j.swevo.2016.03.004>
- [27] Deb, K., Pratap, A., Agarwal, S., & Meyarivan, T. (2002). A fast and elitist multiobjective genetic algorithm: NSGA-II. *IEEE Transactions on Evolutionary Computation*, 6(2), 182–197.
- [28] Holland, J. H. (1992). *Adaptation in natural and artificial systems: An introductory analysis with applications to biology, control, and artificial intelligence*. MIT Press.
- [29] Storn, R., & Price, K. (1997). Differential evolution—a simple and efficient heuristic for global optimization over continuous spaces. *Journal of Global Optimization*, 11(4), 341–359. <https://doi.org/10.1023/A:1008202821328>
- [30] Qin, A. K., Huang, V. L., & Suganthan, P. N. (2009). Differential evolution algorithm with strategy adaptation for global numerical optimization. *IEEE Transactions on Evolutionary Computation*, 13(2), 398–417.
- [31] RM, A. (2009). A new sentence similarity measure and sentence based extractive technique for automatic text summarization. *Expert Systems with Applications*, 36 (4), 7764–7772.
- [32] Liu, J., Chen, K.-Y., Hsieh, Y.L., & Chen, B. (2016). Exploring Word Mover’s Distance and Semantic-Aware Embedding Techniques for Extractive Broadcast News Summarization. *Interspeech*. <https://doi.org/10.21437/Interspeech.2016-710>
- [33] Mikolov, T., Sutskever, I., Chen, K., Corrado, G. S., & Dean, J. (2013). Distributed representations of words and phrases and their compositionality. In *Advances in Neural Information Processing Systems*, 3111–3119.
- [34] Blei, David, M., Andrew, Y. N., & Jordan, M. I. (2003). Latent Dirichlet Allocation. *The Journal of Machine Learning Research*, 3, 993–1022.
- [35] Kupiec, J., Pedersen, J. P., & Chen, F. (1995). A trainable document summarizer. *Proceedings of the 18th Annual International ACM SIGIR Conference on Research and Development in Information Retrieval*, 68–73. <https://doi.org/10.1145/215206.215333>
- [36] Gupta, V., Chauhan, P., & Garg, S. (2012). A statistical tool for multi-document summarization. *International Journal of Scientific and Research Publications*, 2(5).
- [37] Shareghi, E., & Hassanabadi, L. S. (2008). Text summarization with harmony search algorithm-based sentence extraction. *Proceedings of the 5th International Conference on Soft Computing as Trans-disciplinary Science and Technology*, 226–231.
- [38] Narayan, S., Cohen, S. B., & Lapata, M. (2018). Ranking sentences for extractive summarization with reinforcement learning. *Proceedings of the 2018 Conference of the North American Chapter of the*

- Association for Computational Linguistics: Human Language Technologies, Volume 1 (Long Papers)*, 1747–1759.
- [39] Liu, Y. (2019). Fine-tune BERT for extractive summarization. *arXiv preprint arXiv:1903.10318*.
- [40] See, A., Liu, P. J., & Manning, C. D. (2017). Get to the point: Summarization with pointer generator networks. *Proceedings of the ACL Conference*. arxiv:1704.04368
- [41] Celikyilmaz, A., Bosselut, A., He, X., & Choi, Y. (2018). Deep communicating agents for abstractive summarization. *Proceeding of the NAACL Conference.*, 1662–1675.

# Self-Powered and Self-Sustained Energy Systems: Energy Autonomy in the Internet-of-Things Systems

Ankit Mittal\* and Aatmesh Shrivastava

Department of Electrical and Computer Engineering,  
Northeastern University, Boston, USA

*To enable a wide and diverse deployment of the IoT devices for a smart, resilient, and sustainable growth of the global ecosystem, an efficient energy system is vital. In this paper, we present self-powered and self-sustained IoT systems and optimization techniques for their “WHOLISTIC” development. We present a generalized system architecture of the IoT system and with a graph modelling approach, identify critical optimization points in addition to the Type-I and Type-II system optimizations. Finally, we present the IoT applications where such autonomous energy systems are successfully deployed.*

**Keywords** – IoT, Ultra-low power systems, SoS, Energy harvesting, Green computing, Environment sustainability, Graph theory

## I. INTRODUCTION

Internet-of-Things (IoT) promises to integrate electronics in Every-Thing and Every-Ware and has ushered an exponential increase in the demand for Ultra-low Power (ULP) and low-cost IoT devices [1]. Different applications in the industrial, urban, healthcare, smart-home, and wearable space are benefitting from the integration of IoT technologies. It has led to an overall improvement in the quality of life. As we integrate more and more IoT sensors in our environment and living space to make them smarter and well connected, an exponential growth in the number of interconnected devices, as shown in Fig.1, has emerged. An anticipated 75 billion IoT devices are expected to be connected by the year 2025 [2].

A majority of these IoT devices are powered from batteries with a limited lifetime. One estimate indicates that more than 274 million battery replacements would be needed every day when trillions of such IoT devices are powered by batteries, even when these batteries have a 10-year life-time [3]. Power saving techniques such as duty-cycling the IoT device operation and low power circuit designs [4], [5] prolong the lifetime but cannot prevent system drop-out from the network when the energy eventually runs out. Battery-based systems, in the context of such massively expanding IoT networks, not only face challenges in terms of operational reliability but also pose a serious threat to the environmental sustainability due to generation of a large amount of e-waste. Further, the growth in the battery power-density

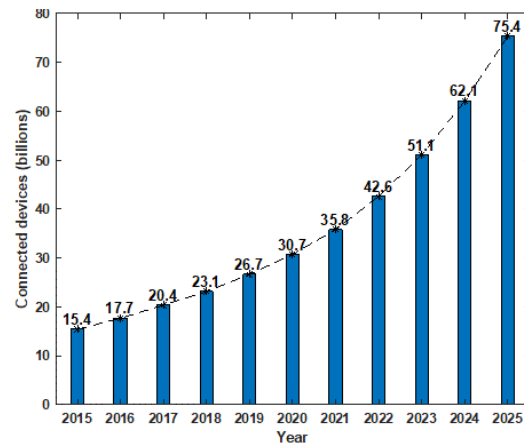


Fig.1. The exponential growth of connected IoT devices.

has not been matched by the demand side power requirement from the IoT devices. For a smart IoT system in the broader spectrum of applications, a *WHOLISTIC* [6] and self-sustained energy system is needed. Energy harvesting techniques where energy is scavenged from ambient sources is a promising approach towards a self-sustained and a perpetual self-powered energy system IoT. It aims to fulfill the “deploy and forget” goal for the IoT sensors from the point of view of energy systems. Although, these self-sustained energy systems are being successfully deployed in the IoT realm but an optimal utilization of the harvested energy in the IoT system, with an unflinching performance is still a challenge.

In this paper, we present an autonomous self-powered, self-sustained energy system for the IoT system,

\* Corresponding author: [mittal.ank@northeastern.edu](mailto:mittal.ank@northeastern.edu)

ISSN 0972-5032 (P); Copyright ©2022, SSI

system of systems (SoS) [7]. To address the overall complexity of the IoT systems resulting from the synergy of diverse and independent complex subsystems, a *WHOLISTIC* design approach can provide a more optimal performance over a mere reductionist approach. General systems principles, have considerably enhanced the understanding and performance of wide range of diverse systems including electrical systems [7], education systems [8], socioeconomic systems [9], transportation systems [10], brain-microtubules modeling [11], and have even been used for explaining spiritual consciousness systems [12]. Using these principles, we present a generalized model for the IoT system under the *WHOLISTIC* design methodology to maximize the overall system performance. The generic IoT system model lays the foundation of a system engineering-oriented framework that can be extended and developed for a specific IoT application.

The paper is organized as follows. In Section II, we present the architecture of an ultra-low power IoT system with a generalized system model. In Section III, we discuss the key components of the energy harvesting system as an autonomous energy system. Design techniques to further improve the performance of such self-powered IoT systems are discussed in Section IV. A brief discussion on the IoT systems where such autonomous energy systems are deployed is presented in Section V and Section VI concludes the paper.

## II. ULTRA LOW POWER IoT SYSTEMS

IoT systems with the integration of diverse systems are actually heterogeneous systems, with increasing efforts to develop them as a monolithic system (single chip solution). The exponential growth of the IoT systems in segments like healthcare, wireless connectivity, and industrial IoT has enabled sensing, processing, and communication of the information of diverse nature in a massively connected network of devices with an ultra-low latency in range of nanoseconds (ns) to few microseconds ( $\mu$ s). In the systems terminology, an IoT system can be regarded as system of systems (SoS), explained below, as it conforms to the principles of SoS [13] also referred to by the acronym “*OMGEE*”.

*Operational (O) and management independence (M)*: A simplified scenario of the IoT systems with diverse subsystems deployed for a targeted application is visualized in Fig. 2. While these subsystems co-exist to achieve the central system goal, they maintain functional and managerial independence with their respective goals and objectives. The architectural governance must ensure that even in the case of a subsystem failure, the overall goal of the system is fulfilled perpetually.

*Geographic distribution (G)*: IoT systems such as smart city and healthcare systems are distributed over a wide geographical region with a 24-hour connectivity. This

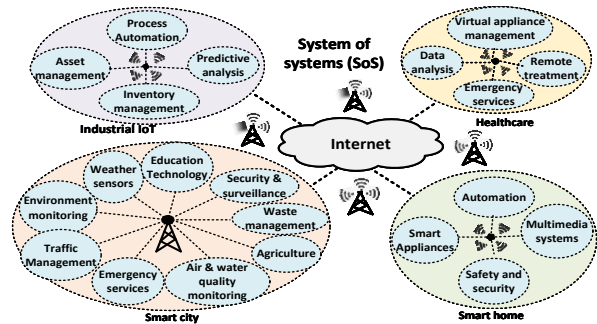


**Fig. 2. A practical IoT system comprising of diverse, independent, continuously evolving, widely distributed subsystems, is a system of systems (SoS).**

connectivity “everytime, everywhere, with everyone, and everything” is ensured by leveraging different wireless technologies [14], [15] such as Bluetooth, ZigBee, SigFox, LoRa etc. which have helped to overcome geographical barriers significantly. It has advanced IoT systems like healthcare where remote health monitoring has significantly leveraged from such technologies [16].

*Emergent behavior (E)*: Emergence is defined as something unexpected in the collective behavior not attributed to any specific subsystem [7]. The interdisciplinary nature of the subsystems of diverse nature in the IoT systems gives rise to objective (ontological) and observed (epistemic) emergent properties. In the context of energy harvesting based ULP IoT systems, environmental sustainability is the beneficial emergent attribute that can advance green computing [17].

*Evolutionary development (E)*: Architecting IoT systems is in itself an evolutionary process where subsystems are continuously enhanced, updated and evolved to maximize the robustness, beneficial emergence, and adaptability to the deployed environment which is often highly dynamic in nature. A detailed discussion on the system architecture design, integration, and evaluation of the diverse subsystems for the ULP IoT system is presented below. It will help us to identify the critical points and interconnections to engineer system optimizations. Analysis of these subsystems and their interactions, aids to identify the critical points of optimization and implement system engineering techniques to achieve a *WHOLISTIC* system performance.

### A. Architecting ultra-low power IoT system

Architecting IoT systems must consider different aspects of the subsystems like complexity, diversity, integration strategy and the overall system security. In Fig. 3, we present a blueprint of a generalized architecture of the IoT system notably an Ultra-Low Power (ULP) IoT system, a microelectronic system which is feasible to be driven by the energy harvesting based energy system.

ULP IoT system comprises of three fundamental subsystems i.e., energy system, energy management, and application system. The coordinated energy flow allows the overall system to attain energy autonomy with a self-powered energy system. “*Simple is complex*” as the fundamental system complexity paradox [7] also underscores the design architecture of the ULP IoT systems which are bound by the constraints of power, performance, and area (PPA). The diverse nature of these subsystems necessitates multiple cycles of “analysis, synthesis, and evaluation” to achieve the required system specifications.

**1. Energy systems:** Energy systems are responsible to provide energy and power to drive the subsystems to accomplish the central goal of the IoT system. The failure of energy systems leading to a system blackout can potentially interrupt or even disrupt the ULP IoT system. Classical battery-based energy system as the singular energy system for IoT applications pose feasibility challenges for the critical applications like remote environment monitoring or biomedical applications where battery replacement is largely impractical, infeasible, and even uneconomical. Techniques like duty cycling to prolong battery lifetime become restrictive for IoT sensors which are required to operate in an always power-on state. Thus, the inevitable process of battery replacement generates massive *e-waste* which challenges the sustainable development of IoT systems. Fig. 3 shows the energy harvesting based energy system as a self-sustained energy system that can potentially overcome the battery replacement requirement in the ULP IoT systems.

**2. Energy management system:** To accomplish the goal of energy autonomy in the IoT systems, a critical architectural component is the energy management system. Energy management system must manage the available energy from the energy harvesting based energy system ensuring a continuous self-sustained unflinching system performance. In Fig. 3, we see the different subsystems of the energy management system which are primarily responsible to provide a stable and regulated power supply to the entire system, ensure observability of the energy flow in the system, make decisions under the dynamic load or environmental conditions, and provide a robust infrastructure to drive the IoT application. We present a detailed analysis of these subsystems in Section IV which highlights their critical role in the *WHOLISTIC* system performance.

**3. Application system:** The nature of IoT application dictates the design of the subsystems and their interactions. The application system which covers a wide spectrum of applications in the IoT space presents varied design goals for the energy system and management. In Section V we present different application systems which are driven by the self-powered energy systems.

### B. System simulation and evaluation

To validate the performance under the Requirement Specifications (RS) and prevent deployment failures, ULP IoT systems are simulated and tested on test platforms which emulate the actual deployment environment. To develop a simulation framework to validate the diverse subsystems of interdisciplinary nature, surrogate models or metamodels in the form of behavioral models are abstracted to integrate them into the simulation platform. Diverse modelling for healthcare IoT systems [18]–[20] and radio frequency IoT systems [21] have demonstrated the value addition of developing such models to advance the system design [22]. To emulate the external environment where such systems would be deployed, models of analytical, statistical, or even empirical nature are developed to emulate and account for real life condition [23]. These models are continually updated to minimize the modelling errors or imperfections. These simulation platforms in the form of software/hardware prototypes also serve to speed up the system evaluation process allowing to anticipate possible failures ahead of time thus maximizing system reliability. Modelling aging induced degradation in the design of integrated circuits for IoT sensors is one example where such models can predict the lifetime of IoT systems [24].

### C. System integration

The diverse nature of IoT subsystems must address the three fundamental aspects of integration i.e. physical, functional, and semantic compatibility implemented at the interface level. In Fig. 3 we see that along with the compatibility, optimizations even at the interface level must be undertaken to maximize the system performance. For IoT applications like wireless sensor nodes in the IoT network, standard protocols ensure a seamless information exchange in the network [25]. Integration strategies like system bridging, which involves an additional system to address the integration aspects or system refactoring that modifies the existing systems and interfaces, are the two most basic integration strategies in SoS. Another critical aspect that needs to be addressed during the integration of diverse subsystems is the security of the overall system. Specifically, Integrated Circuit (IC) design for the ULP IoT system has transformed into a supply-chain based process where design and manufacturing is outsourced. The horizontal business model of chip manufacturing provides multiple entry points to an adversary to insert malicious hardware in the chip to compromise the overall system security. It can disrupt system operations after a long time once these systems are deployed [26]. Countermeasures against these cyber-attacks for the hardware security of the ULP IoT system is now an integral part of the design and integration flow [27]–[30].

### D. System evolutionary development

With an increasing complexity of IoT systems deployed

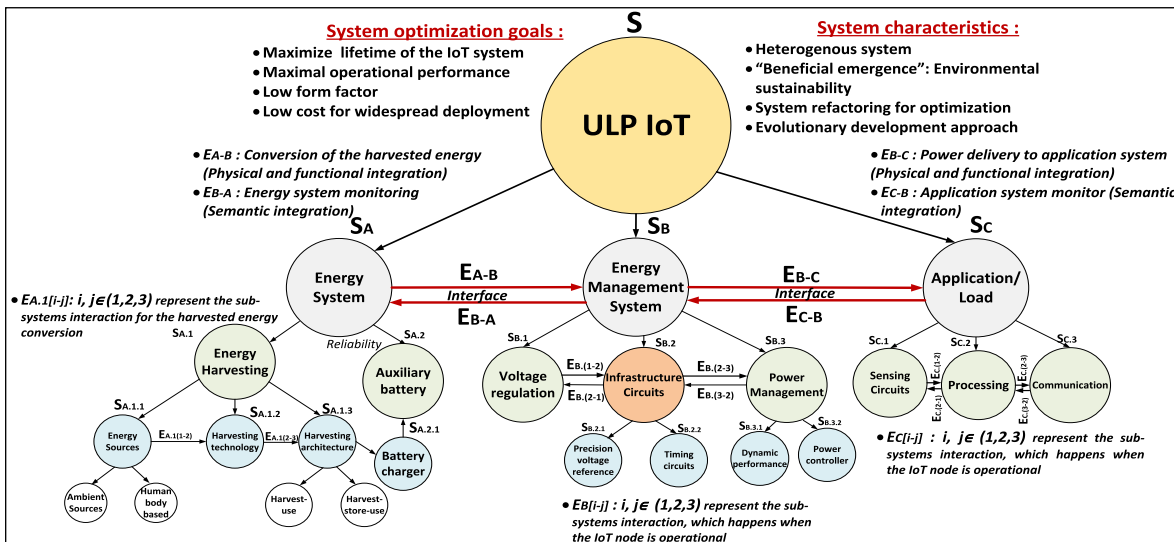


Fig. 3. Architecting ULP IoT system using a graph modelling approach helps to identify and optimize key interfaces, interactions, and parameters of the diverse subsystems.

for the networked society, envisioning all possible test scenarios to simulate the system may seem infeasible and hence design upgrade is essential to the development of IoT systems. The systems are advanced to address the changing needs of the environment or users [31]. Thus, an evolutionary development and enhancement of IoT systems as an architectural specification maximizes the intended objective of the system even under the dynamic conditions of the external environment. Such evolutionary changes can be implemented at the boundaries of subsystems, protocols, device level in the system framework [32], [33]. In the context of ULP IoT system this translates to the design of programmable hardware [34], in-situ training, software updates [35] etc. The techniques of supervised and unsupervised learnings also “train” the system to develop resilience against the stochastic environment [36], [37].

### E. ULP IoT system: Graph modelling

We see that the IoT system as SoS is a synergy of diverse complex independent systems integrated to accomplish the targeted application. Systems view in this regard becomes critical to design, simulate, evaluate, and integrate IoT systems particularly the self-sustained self-powered ULP IoT systems. A system graph based mathematical modelling approach in the generalized systemic view is a natural choice to achieve a *WHOLISTIC* performance for the IoT systems [38]. Recent works in the domain of healthcare [39], smart home [40], [41], smart city [42], vehicular routing [43], have shown the use of graph-based modelling approach to develop and advance the design of the IoT systems. While [39]-[43] present the system graph models for a software-oriented infrastructure development, we model the ULP IoT

system as a generalized microelectronic system to optimize the hardware design. In Fig. 4, we present the graph model of a generalized ULP IoT system feasible to be driven by the self-powered energy system.

**1. System graph representation nomenclature:** We represent the ULP IoT system as a directed graph comprising of various architectural systems represented by the vertices ( $V$ ) and the interactions and interconnections by edges ( $E$ ). The architectural representation of the ULP IoT system ( $S$ ) in : Energy systems are responsible to provide energy and power to drive the subsystems to accomplish the central comprises of three fundamental systems i.e. energy system ( $S_A$ ), energy management system ( $S_B$ ), and application system ( $S_C$ ) as also described in Section 0-A. While each of these complex subsystems can be further represented by a higher order of singularly hierarchical system, our representation of  $S_A, S_B, S_C$  to two levels is a generalized representation of the ULP IoT systems. These subsystems, which are represented by  $S_{i,j}$  where  $i, j \in N$ , form the vertices ( $V$ ) of the system graph (graph order 24). The interactions and interconnection between the subsystems of this directed graph are represented by the edges  $E$ . Directionality of the graph implies the energy flow in the modelled system. ( $E_{A,1[i-j]}$ ), represents the interaction between the subsystems of ( $S_A$ ), ( $E_{B,[i-j]}$ ), represents the interaction between the subsystems of ( $S_B$ ), ( $E_{C,[i-j]}$ ) represents the interaction between the subsystems of ( $S_C$ ) where  $i, j \in \{1, 2, 3\}$ . The details of each subsystem along with interactions are tabulated in Table I. We have limited the number of nodes and edges in this system graph modelling without compromising the generalized representation to demonstrate the plausibility of such optimization philosophy specifically to the ULP IoT systems. Application specific graph for different IoT applications can be even represented as multigraphs with higher order

TABLE I  
DEFINITION OF NODES AND EDGES OF THE GENERALIZED ULP IoT SYSTEM GRAPH

System graph component	Description	Design details
<i>Graph nodes (V)</i>		
$S_A$	Energy system	Source of energy/power for the entire ULP IoT system
$S_B$	Energy Management system	To monitor, regulate, control, distribute the energy from energy system ( $S_A$ ) to the application system ( $S_C$ )
$S_C$	Application system	Sensing, processing, and communication of information for the ULP IoT system
$S_{A,[i]} : i \in \{1,2\}$	Subsystems $S_A$ : Level 1	Primary system $S_{A,1}$ ; backup system $S_{A,2}$ (reliability)
$S_{A,1,[i]} : i \in \{1,2,3\};$ $S_{A,2,1}$	Subsystems $S_A$ : Level 2	$S_{A,1,[i]} : i \in \{1,2,3\}$ : To enable energy harvesting $S_{A,2,1}$ : Replenish battery charge
$S_{B,[i]} : i \in \{1,2,3\}$	Subsystems $S_B$ : Level 1	Regulate, monitor, control, distribute energy to the entire ULP IoT system
$S_{B,1,[i]} : i \in \{1,2\}$ $S_{B,2,[i]} : i \in \{1,2\};$	Subsystems $S_B$ : Level 2	Precision timing control, ultra-low power consumption. Programmability and on-chip learning ensure evolutionary development
$S_{C,[i]} : i \in \{1,2,3\}$	Subsystems $S_C$ : Level 1	Sensing, processing, and communication of the information
<i>Graph edges (E)</i>		
$E_{A-B}$	Energy/information link from $S_A$ to $S_C$ : Feedforward link	Monitor, regulate the received energy/power. System re-factoring integration strategy
$E_{B-C}$	Energy/Information link from $S_B$ to $S_C$ : Feedforward link	Surplus is stored, operational risk indicated
$E_{B-A}$	$S_B$ and $S_A$ interaction: Feedback link	Surplus to be stored for $S_A$ indicated by $S_B$ based on the operational state of $S_C$ (indicated by $E_{C-B}$ )
$E_{C-B}$	$S_C$ and $S_B$ interaction: Feedback link	Indicates the operational state of $S_C$ . $S_B$ takes control measures to ensure unflinching performance even under dynamic conditions
$E_{A,[1-2]}$	Energy harvested by $S_{A,1,2}$ : Feedforward link	Design of the harvesting technology to maximize harvesting
$E_{A,[2-3]}$	Available harvested energy to $S_{A,1,3}$ : Feedforward link	Commonly implemented energy harvesting architectures like harvest-use; harvest-store-use
$E_{B,[1-2]}$	Regulated voltage to $S_{[j],[i]} : i \in \{1,2,3\}, j \in \{B,C\}$ ,	Voltage regulation, conversion can be implemented with switching converters, linear regulators etc.
$E_{B,[2-1]}$	Control of $S_{B,1}$	Design to ensure system startup conditions, load scalability etc.
$E_{B,[2-3]}$	Power management link: Feedforward link	Implement ultra-low power optimization techniques like power gating, duty cycling etc., battery management
$E_{B,[3-2]}$	Control of $S_{B,2}$ governed by $S_{B,3}$ : Feedback link	Power management implements power saving techniques like clock gating, power gating etc.
$E_{C,[i-j]}$	Interaction between $S_{C,[i]}$ where $i \in \{1,2,3\};$	Sensing: Diverse and heterogeneous sensors, Processing: Realtime, on-chip learning systems, Communication: Wireless link (PAN, LAN, WLAN etc.)

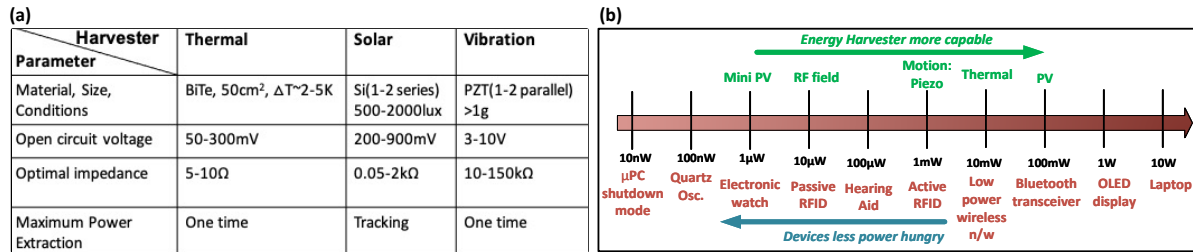


Fig. 4. (a) Commonly used energy harvesters and their properties (b) Energy harvesting along with an effective energy management is necessary to meet the increasing power demands.

system complexity [42], [44]. Recent work on Space-time-varying graph (STVG) can be applied to address the evolutionary aspect of the IoT systems as well [45].

**2. System graph objectives:** The main objectives which guide the optimizations strategy include:

- i). Maximizing IoT system lifetime
- ii). Unfailing system performance in all conditions
- iii). Low form factor
- iv). Low cost for widespread deployment.

With the representation of the IoT system as a generalized system graph, we discuss some of the critical interactions to boost the overall performance of the system with the implementation of Type I and Type II system optimization principles [6] for the self-powered, self-sustained IoT systems. For the ULP IoT system, the overall “beneficial emergence” from system optimization is immense when the scenario is scaled to the entire ecosystem as depicted in Fig. 2, leading to the environmental sustainability with its green computing approach. A mathematical formulation of such optimization framework and modelling can also be undertaken for a specific IoT system.

### III. ENERGY HARVESTING SYSTEM

The goal of the energy harvesting system ( $S_{A.1}$ ) is to ideally harvest all the available energy, which can enable a robust energy system for the ULP IoT system operations. An efficient energy harvesting system must have reliable and efficient energy sources ( $S_{A.1.1}$ ), which can be converted into the usable energy with maximum possible efficiency ( $S_{A.1.2}$ ) and delivered to the load or stored, as dictated by the energy management system.

#### A. Energy Harvesting Sources ( $S_{A.1.1}$ )

The conventional methods of energy harvesting include harvesting from the ambient renewable sources like solar [46], [47] thermal [48], [49] pressure [46], [47], electromagnetic [50] etc. ULP IoT systems driven from the

energy of human body have also gained a significant traction over the years where energy is harvested from the body heat [51], cerebrospinal fluid [52], endocochlear potential [53] for the IoT systems like IMDs and wireless body sensor networks among others. Different factors like availability of the source, reliability, energy density, controllability, and ease-of-use must be evaluated specific to the application.

#### B. Energy Harvesting Technology ( $S_{A.1.2}$ )

Functional integration of the diverse energy sources to the energy harvesting system is achieved using energy harvesting technology (or energy harvester). The role of the energy harvesters is to efficiently convert the energy from different energy sources to electrical energy which can drive the entire ULP-IoT system. Such source-specific harvesters and their properties are tabulated in Fig. 4(a). To maximize the efficiency of harvesting ( $E_{A.1.1|2}$ ), these harvesters must present an optimal impedance even under the dynamic source-load conditions. Such optimizations and decision control is architecturally governed by energy management system ( $S_B$ ).

#### C. Energy Harvesting Architecture ( $S_{A.1.3}$ )

Energy harvesting architecture can be broadly classified as Harvest-use architecture and Harvest-store-use architecture [54].

**1. Harvest-use architecture:** In this architecture, the load is directly driven by the harvesting system [55]. Our objective to design self-perpetual self-powered ULP IoT system design with an unfailing performance under all conditions may be challenged by certain aspects of this architecture which includes lack of controllability, frequent operational failure due to abrupt changes in the harvested energy, system start-up failure on account of inadequate voltage, and incapability to store any surplus energy.

**2. Harvest-store-use architecture:** In the harvest-store-

use based architecture, the system derives power from the storage system, which is an essential component of this architecture. The storage capability in harvest-store-use architecture addresses the key challenges faced in harvest-use architecture particularly system reliability, storage of surplus energy. This makes harvest-store-use architecture a preferred choice for the self-autonomous energy systems. The perpetual interaction of harvest-use-based architecture with the energy management system ( $S_B$ ), ensures that the stored energy is well regulated for use and any surplus energy is stored for future use or even enhance the dynamic performance of the system. Energy systems can be directed by energy management systems through the interface ( $E_{A-B}$ ) to store the additional energy when load (subsystems of  $S_B$  or  $S_C$ ) is operationally duty cycled, or to compensate for energy system's inability to supply adequate power for a period of time. Commonly used storage technology include capacitors [46], [49], [50], [56], super-capacitors [47], Li-based batteries[47], [48], integrated batteries [57] etc.

#### D. Energy Harvesting System challenges

To realize energy harvesting based energy system as a reliable, feasible, self-sustained, and perpetual energy system, it is crucial to address the operational challenges faced at different system and interface level operated by such energy system. A brief discussion on these aspects is presented below:

**1. Monitoring:** An essential task of energy management system ( $S_B$ ) is to monitor the net energy availability in the system, which indicates the status/'health' of the ULP IoT system. In the harvest-store-use architecture,  $S_B$  monitors the available energy through the interface ( $E_{A-B}$ ) and ensures that energy flow to  $S_C$  through the interface ( $E_{B-C}$ ) is uninterrupted which minimizes the outage probability. Such monitoring systems must be designed with minimal power consumption to prevent additional overhead to the energy budget of the IoT system.

**2. Reliability:** The primary objective of the ULP IoT system to have an uncompromising and unflinching performance at all times, may quickly deplete the harvested energy specifically under conditions of overload or inadequate energy supply which may lead to a system black-out or brown-out. The reliability issues in a single energy source based architectures (SISO/SIMO) are addressed by the architectures where energy is harvested from multiple energy sources (MISO/MIMO) [47], [56], [58]. Auxiliary system like additional battery ( $S_{A,2}$ ) is another way to impart better reliability to the system.

**3. Integration:** An efficient integration of diverse energy sources (ambient or human body based) as the source of electrical energy in the ULP IoT system not only requires

an efficient conversion by the harvesting technology ( $S_{A,1,2}$ ), but an efficient interface ( $E_{A-B}$ ) to optimize this energy flow is essential. While harvesting technology presents a system-bridging strategy for the physical integration of these diverse energy sources, the functional and semantic integration is achieved using a system-refactoring approach where the interface is optimized to maximize the available energy to the system. The energy management system must present an optimal impedance at the interface ( $E_{A-B}$ ) corresponding to the impedance of harvesting technology (Fig. 4 (a)) for a high conversion efficiency.

**4. Deployment:** Cost is a significant consideration which influences a widespread deployment of the ULP IoT systems particularly in the IoT segments like consumer electronics, healthcare, industrial IoT. A low form factor as a design specification in energy harvesting based ULP IoT systems, supports a monolithic integrated solution (chipset), reducing the cost of these systems significantly. Post deployment, any required design upgrade of these systems should be at no or minimal maintenance and operational cost [59].

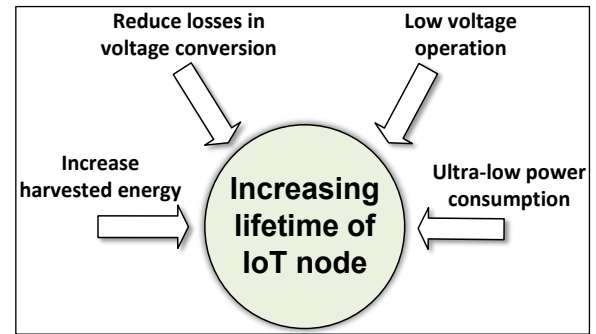


Fig. 5. The lifetime of a self-powered IoT system can be significantly improved with different techniques at the component level, sub-system level and system level

#### IV. IoT ENERGY MANAGEMENT

Energy management system ( $S_B$ ) processes the energy from the energy system ( $S_A$ ) to be used by the application system ( $S_C$ ). The success of energy harvesting system for the self-powered IoT is therefore not only limited to the intrinsic optimizations, the effective use and management of this energy is of paramount importance. Accordingly, energy management system must ensure a low energy processing cost for the harvested energy to be efficiently used in the application system.

Fig. 4(b) presents typical power consumption of different electronic systems ranging from nanowatt (nW) to few watts (W). The power consumption of such systems at the higher end of spectrum, is beyond the maximum harvesting capability of energy harvesting based system which implies that energy harvesting system may not be

able to cater to the power requirements of such systems exclusively, but the co-existence of an efficient management system helps to achieve the goal of self-concepts of system engineering like analysis, design, controllability, observability, stability, and simulations are part of the optimizations of these systems. We briefly discuss different techniques at critical points of the system graph to optimize integration of energy management subsystems at physical, functional, and semantic level to achieve architectural resonance.

### A. Interface with Energy System

**1. Maximum power point tracking:** A well-designed interface ( $E_{A-B}$ ) between ( $S_A$ ) and ( $S_B$ ) must ensure a minimal loss during the energy conversion. This implies that the interface must present an optimal impedance for the maximum power transfer. This impedance matching may be a one-time setting (thermal, piezo) or may require continuous tracking (solar, RF). To ensure maximal power transfer even under dynamic ambient conditions, maximum power point tracking circuits (MPPT) are implemented in the energy management system to continuously track the maximum power point [47], [56], [58], [60] for a high energy conversion efficiency.

**2. Low startup voltage operation:** For energy harvesters like thermal energy generators (TEG), the open circuit voltage may be below the operation requirement of the different subsystems of ( $S_B$ ) and ( $S_C$ ). Under such scenario, the ULP IoT system may even fail to startup. To ensure that the ULP IoT system is supplied with the minimum required threshold operational voltage, different startup mechanism may be used which include pre-charge voltage from external source like battery, cold start (CS) unit [4], [58], [61]. Along with the startup circuit, the lifetime of the ULP IoT system on energy harvesting based energy system can be substantially increased by reducing the operating voltage of the subsystems [3].

**3. Voltage regulation of harvested energy:** Energy management system regulates the harvested voltage and provides multiple output voltages to operate subsystems with different supply voltage requirements ( $S_{B,1}$ ). Voltage regulation ( $E_{B(1-2)}$ ) is achieved using linear regulators [62], [63] switching converters [64], [65]. Single input multiple output (MIMO) [65] design architectures cater to the multiple supply requirement of the subsystems.

### B. Energy Management: Infrastructure Circuit

Infrastructure circuits ( $S_{B,2}$ ) represent critical subsystem of the energy management system. These infrastructure circuits comprise of timing circuits ( $S_{B,2,1}$ ) like system clock generator, pulse generator, wake-up timers etc. to actuate system operations with temporal precision and

powered ULP IoT systems. In Fig. 5, different methods to increase the lifetime of an IoT system with energy harvesting based energy system are presented. Different voltage reference circuits ( $S_{B,2,2}$ ) like power on reset circuit (POR), bandgap reference (BGR) to provide a precise reference voltage for the entire ULP IoT system. In many IoT applications, IoT nodes may mostly be in an idle mode and “wake-up” only for short bursts of activity. To check for system activity/stimulus, the occasional wakeups are coordinated by the precision timing circuits. Further, to enable a low operational voltage for the sub-systems, precision reference voltage is required. With such critical role in the systems operation, infrastructure circuits are in an always power-on state even when the entire ULP IoT system is operationally duty cycled. The idle power (leakage power) sets the minimum energy requirement for the energy system to prevent blackout of the entire ULP IoT system. Ultra-low power high precision oscillators [5], BGR circuits [4] are essential to optimizing the WHOLISTIC system performance [3].

### C. Power Management

Power management system ( $S_{B,3}$ ) comprises of power management controller which implements power saving for the ULP IoT system to extend its operational lifetime along with over-voltage and under-voltage protection scheme for the battery management. Different techniques include fine power gating, clock gating, optimizing the process technology etc. Design optimizations in the infrastructure circuits along with these power saving techniques can provide a 4-70 times improvement in the lifetime of the ULP IoT system [3].

### D. Energy Management: Architecture Governance

To prevent uncoordinated changes in the energy flow, the management system ensures an overall control on subsystems  $S_k$ ,  $k \in (A, B, C)$ ; and interconnections. A closed loop approach in the energy management system provides a flexible platform for the overall system achieving WHOLISTIC performance [56]. The optimization strategy of energy management subsystems is a multivariate concurrent optimization problem in itself, primarily guided by the specifications of the application system. Thus, system optimizations significantly enhance the optimization benefits of such complex IoT systems by providing a deeper insight into system’s interaction systems which may be excluded/overlooked in the traditional reductionist design approach.

## V. IoT APPLICATION

The application system ( $S_C$ ) in the system graph, represents key objective which the ULP IoT system must efficiently accomplish. Primarily, information sensing ( $S_{C,1}$ ), processing ( $S_{C,2}$ ) and communicating the processed in

**TABLE II**  
**SUMMARY OF ENERGY HARVESTING BASED ENERGY SYSTEMS**

Ref	TCAS 2019 [46]	JSSC 2019 [48]	JSSC 2013 [56]	MTT 2013 [50]	JSSC 2012 [47]	JSSC 2011 [49]
<b>Technology</b>	65nm	350nm	130nm	180nm	350nm	350nm
<b>Energy Source</b>	Solar, Piezo	Thermal	RF, Thermal/Solar	RF	Solar, Thermal, Piezo	Thermal
<b>Energy Harvesting Architecture</b>	MISO	SISO	MISO	SISO	MISO	SISO
<b>Harvesting Technology</b>	Solar Cells + Piezo Crystal	TEG array	TEG array	On-chip antenna	Solar cell+ TEG + Piezo crystal	TEG
<b>Input Voltage</b>	0.55V	0.18V-10V	30mV, -10dBm	-17dBm	-	25mV (35mV for startup)
<b>Conversion Efficiency (%)</b>	74.60	86% 99% peak efficiency	38%	42% (Simulated)	64%: Thermal 87%: Photovoltaic 79%: Piezo	58%
<b>Output voltage</b>	1.8-2.5V	-	1.35V	1V	20mV-0.16V: Thermal 0.15V-0.75V: Solar 1.5V-5V: Piezo	1.8V
<b>Storage Technology</b>	Capacitor	Capacitor + Battery (3.3V) for energy Recycling	Capacitor	Capacitor	Supercapacitors & 3.3V Li Battery	Capacitor
<b>In built Power Extraction</b>	Yes	Yes	No	Impedance Matching network	Yes	Yes
<b>Maximum Power Output</b>	35μW-70μW	38μW-200mW	ASIC power req. 19μW	2.5nJ	1.3mW: Thermal 2.5mW: Photo 200μW: Piezo	~300μW
<b>Applications</b>	Wireless Sensor Nodes	Body Sensor Network (BSN)	Self-powered ASIC for measurement of Biomedical signals	Implantable Intraocular Pressure Monitoring	Ultra-low power IoT systems	Implantable, wireless micro sensors

formation ( $S_{C.3}$ ) represent the elemental features of the application system. Depending on the specific application like IMDs, body sensor network (BSN), ULP IoT radios, different optimization weights are assigned to different systems and interface. In Table II, we present different ULP IoT system deployed for the application in healthcare [48], [50], [56] wireless communication [46] etc. driven by the energy harvesting based energy system. To improve the reliability and efficiency of the system, multiple input single output (MISO) architecture ( $S_{A.1.1}$ ) [46], [47], [56], additional storage technology like supercapacitor and battery ( $S_{A.2.1}$ ) [47], [48] are included in the ULP IoT system design as discussed in Section III. These system level optimization managed by the energy management system can ensure an unflinching performance even under stochastic environmental conditions and load fluctuations [56]. To validate the system performance for the fundamental system properties i.e. synthetically, hermeneutically, and constitutively de-

terminability [67] in the stochastic conditions, ULP IoT systems are validated with system level simulations during the design phase and tested on testbeds before the final deployment. Specific system standards and frameworks ensure interoperability of these systems in the IoT ecosystem [68]. The system optimization engineering techniques discussed in Section III, IV when applied to the energy harvesting based ULP IoT systems hold the potential of self-powered self-sustained energy systems for future IoT applications towards green IoT [69], [70].

## VI. CONCLUSION

The evolution of IoT systems as the self-powered and self-sustained systems will lead to an even wider global deployment of such devices ensuring connectivity for a smart and resilient ecosystem with strong beneficial emergent properties of environmental sustainability through its “green computing” approach. In this paper

we presented an autonomous energy system based on energy harvesting. With a generalized system architecture and graph modelling of the ULP IoT system we identify the critical optimization points in the energy flow leading to a *WHOLISTIC* system with higher reliabi-

lity, performance robustness and significant lifetime improvement. The generalized graph model of the IoT system would also motivate the future design methodology of the ULP IoT system to a more *WHOLISTIC* approach over the traditional reductionist approach.

## REFERENCES

- [1] Al-Fuqaha, A., Guizani, M., Mohammadi, M., Aledhari, M., & Ayyash, M. (2015). Internet of things: A survey on enabling technologies, protocols and applications. *IEEE Communications Surveys & Tutorials*, 17(4), 2347-2376.
- [2] "IoT market size worldwide 2017-2025|Statista," [Online]. Available: <https://www.statista.com/statistics/976313/global-iot-market-size/>
- [3] Shafiee, N., Tewari, S., Calhoun, B., & Shrivastava, A. (2017). Infrastructure circuits for lifetime improvement of ultra-low power IoT devices. *IEEE Transactions on Circuits and Systems I: Regular Papers*, 64(9), 2598-2610.
- [4] Shrivastava, A., Craig, K., Roberts, N. E., Wentzloff, D. D., & Calhoun, B. H. (2015, February). 5.4 A 32nW bandgap reference voltage operational from 0.5 V supply for ultra-low power systems. In *2015 IEEE International Solid-State Circuits Conference (ISSCC) Digest of Technical Papers* (pp. 1-3). IEEE.
- [5] Shrivastava, A., Kamakshi, D. A., & Calhoun, B. H. (2016). A 1.5 nW, 32.768 kHz XTAL oscillator operational from a 0.3 V supply. *IEEE Journal of Solid-State Circuits*, 51(3), 686-696.
- [6] D. A. Rao, "Introduction to Systems and Systems Philosophy", [Online]. Available: [https://www.dei.ac.in/dei/paritantrika/files/archives/Systems\\_Methodology.pdf](https://www.dei.ac.in/dei/paritantrika/files/archives/Systems_Methodology.pdf)
- [7] Jamshidi, M. (Ed.). (2017). *Systems of systems engineering: principles and applications*. CRC press.
- [8] K. S. Daya, "Systems Approach", [Online]. Available: <https://www.dei.ac.in/dei/files/aboutDEI/DEI-Systems-Approach.pdf>
- [9] Satsangi, P.S. & Ellis, J. B. (1971). A generalized system-theoretic framework for modelling large scale national economic systems in dynamic, structural and spatial terms. *International Journal of Systems Science*, 2(2), 213-223.
- [10] Satsangi, P. S. (1977). A Physical System Theory Modeling Framework for Transportation System Studies. *IEEE Transactions on Systems, Man, and Cybernetics*, 7(11), 763-778.
- [11] Srivastava, D. P., Sahni, V., & Satsangi, P. S. (2016). Modelling microtubules in the brain as n-qudit quantum Hopfield network and beyond. *International Journal of General Systems*, 45(1), 41-54.
- [12] P. S. Satsangi, S. R. Hameroff, V. Sahni, and P. Dua, "Chapter 2: Cosmic Consciousness Hierarchization," in *Consciousness: Integrating Eastern and Western Perspectives*, New Age Books, 2016. [Online]. Available: <https://books.google.com/books?id=0aUwngAACAAJ>
- [13] Maier, M. W. (1998). Architecting principles for systems-of-systems. *Systems Engineering: The Journal of the International Council on Systems Engineering*, 1(4), 267-284.
- [14] Andreev, S. et al. (2015). Understanding the IoT connectivity landscape: a contemporary M2M radio technology roadmap. *IEEE Communications Magazine*, 53(9), 32-40.
- [15] Akpakwu, G. A., Silva, B. J., Hancke, G. P., & Abu-Mahfouz, A. M. (2017). A survey on 5G networks for the Internet of Things: Communication technologies and challenges. *IEEE Access*, 6, 3619-3647.
- [16] Ghosh, A. M., Halder, D., & Hossain, S. A. (2016, May). Remote health monitoring system through IoT. In *2016 5th International Conference on Informatics, Electronics and Vision (ICIEV)* (pp. 921-926). IEEE.
- [17] Zhu, C., Leung, V. C., Shu, L., & Ngai, E. C. H. (2015). Green internet of things for smart world. *IEEE Access*, 3, 2151-2162.
- [18] Suster, M. A., Vitale, N. H., Maji, D., & Mohseni, P. (2016). A circuit model of human whole blood in a microfluidic dielectric sensor. *IEEE Transactions on Circuits and Systems II: Express Briefs*, 63(12), 1156-1160.
- [19] Martos-Repath, I., Mittal, A., Zaeimbashi, M., Das, D., Sun, N. X., Shrivastava, A., & Onabajo, M. (2020, August). Modeling of magnetoelectric antennas for circuit simulations in magnetic sensing applications. In *2020 IEEE 63rd International Midwest Symposium on Circuits and Systems (MWSCAS)* (pp. 49-52). IEEE.
- [20] Duncan, K. R., & Etienne-Cummings, R. (2017, May). A model based approach for realizing a safe wireless biotelemetry system. In *2017 IEEE International Symposium on Circuits and Systems (ISCAS)* (pp. 1-4). IEEE.
- [21] Kazanc, O., Maloberti, F., & Dehollain, C. (2012, May). Simulation oriented rectenna design methodology for remote powering of wireless sensor systems. In *2012 IEEE International Symposium on Circuits and Systems (ISCAS)* (pp. 2877-2880). IEEE.
- [22] Das, D. et al. (2020). A radio frequency magnetoelectric antenna prototyping platform for neural activity monitoring devices with sensing and energy harvesting capabilities. *Electronics*, 9(12), 2123.
- [23] Borrelli, A., Monti, C., Vari, M., & Mazzenga, F. (2004, June). Channel models for IEEE 802.11 b indoor system design. In *2004 IEEE International Conference on Communications (IEEE Cat. No. 04CH37577)* (Vol. 6, pp. 3701-3705). IEEE.
- [24] Maricau, E., & Gielen, G. (2011, September). Transistor aging-induced degradation of analog circuits: Impact analysis and design guidelines. In *2011 Proceedings of the ESSCIRC (ESSCIRC)* (pp. 243-246). IEEE.
- [25] Sharma, M. (2014, July). Wireless sensor networks: Routing protocols and security issues. In *Fifth International Conference on Computing, Communications and Networking Technologies (ICCCNT)* (pp. 1-5). IEEE.
- [26] Yang, T., Mittal, A., Fei, Y., & Shrivastava, A. (2020). Large Delay Analog Trojans: A Silent Fabrication-Time Attack Exploiting Analog Modalities. *IEEE Transactions on Very Large Scale Integration (VLSI) Systems*, 29(1), 124-135.
- [27] Agrawal, D., Baktir, S., Karakoyunlu, D., Rohatgi, P., & Sunar, B. (2007, May). Trojan detection using IC fingerprinting. In *2007 IEEE Symposium on Security and Privacy (SP'07)* (pp. 296-310). IEEE.
- [28] Bhunia, S., Hsiao, M. S., Banga, M., & Narasimhan, S. (2014). Hardware Trojan attacks: Threat analysis and

- countermeasures. *Proceedings of the IEEE*, 102(8), 1229-1247.
- [29] Elshamy, M., Di Natale, G., Pavlidis, A., Louërât, M. M., & Stratigopoulos, H. G. (2020, May). Hardware trojan attacks in analog/mixed-signal ICs via the test access mechanism. In *2020 IEEE European Test Symposium (ETS)* (pp. 1-6). IEEE.
- [30] Fyrbiak, M. et al. (2018). HAL—the missing piece of the puzzle for hardware reverse engineering, trojan detection and insertion. *IEEE Transactions on Dependable and Secure Computing*, 16(3), 498-510.
- [31] Ye, L. et al. (2021). The challenges and emerging technologies for low-power artificial intelligence IoT systems. *IEEE Transactions on Circuits and Systems I: Regular Papers*.
- [32] Zimmermann, H. (1980). OSI reference model-the ISO model of architecture for open systems interconnection. *IEEE Transactions on Communications*, 28(4), 425-432.
- [33] Wu, G., Talwar, S., Johnsson, K., Himayat, N., & Johnson, K. D. (2011). M2M: From mobile to embedded internet. *IEEE Communications Magazine*, 49(4), 36-43.
- [34] Qi, H., Ayorinde, O., & Calhoun, B. H. (2017, October). An ultra-low-power FPGA for IoT applications. In *2017 IEEE SOI-3D-Subthreshold Microelectronics Technology Unifed Conference (S3S)* (pp. 1-3). IEEE.
- [35] Boudguiga, A., Bouzerna, N., Granboulan, L., Olivereau, A., Quesnel, F., Roger, A., & Sirdey, R. (2017, April). Towards better availability and accountability for iot updates by means of a blockchain. In *2017 IEEE European Symposium on Security and Privacy Workshops (EuroS&PW)* (pp. 50-58). IEEE.
- [36] Azari, A., & Cavdar, C. (2018, December). Self-organized low-power iot networks: A distributed learning approach. In *2018 IEEE Global Communications Conference (GLOBECOM)* (pp. 1-7). IEEE.
- [37] Yamato, Y., Kumazaki, H., & Fukumoto, Y. (2016, November). Proposal of lambda architecture adoption for real time predictive maintenance. In *2016 Fourth International Symposium on Computing and Networking (CANDAR)* (pp. 713-715). IEEE.
- [38] Yao, B. et al. (2013, November). Applying graph theory to the internet of things. In *2013 IEEE 10th International Conference on High Performance Computing and Communications & 2013 IEEE International Conference on Embedded and Ubiquitous Computing* (pp. 2354-2361). IEEE.
- [39] Zaman, F., Aloqaily, M., Sallabi, F., Shuaib, K., & Othman, J. B. (2020, December). Application of Graph Theory in IoT for Optimization of Connected Healthcare System. In *GLOBECOM 2020-2020 IEEE Global Communications Conference* (pp. 1-6). IEEE.
- [40] Jia, Y., Xiao, Y., Yu, J., Cheng, X., Liang, Z., & Wan, Z. (2018, April). A novel graph-based mechanism for identifying traffic vulnerabilities in smart home IoT. In *IEEE INFOCOM 2018-IEEE Conference on Computer Communications* (pp. 1493-1501). IEEE.
- [41] Modarresi, A., & Sterbenz, J. P. (2018, September). Towards a model and graph representation for smart homes in the IoT. In *2018 IEEE International Smart Cities Conference (ISC2)* (pp. 1-5). IEEE.
- [42] Gorawski, M., & Grochla, K. (2019, October). Graph representation of linear infrastructure in Smart City IoT Systems. In *2019 11th International Congress on Ultra Modern Telecommunications and Control Systems and Workshops (ICUMT)* (pp. 1-4). IEEE.
- [43] He, C., Qu, G., & Wei, S. (2021, June). A Vehicular Communication Routing Algorithm Based on Graph Theory. In *2021 International Wireless Communications and Mobile Computing (IWCMC)* (pp. 2176-2181). IEEE.
- [44] Chuang, I. H., Guo, B. J., Tsai, J. S., & Kuo, Y. H. (2017, May). Multi-graph Zero-knowledge-based authentication system in Internet of Things. In *2017 IEEE International Conference on Communications (ICC)* (pp. 1-6). IEEE.
- [45] Maduako, I., Wachowicz, M., & Hanson, T. (2019). STVG: an evolutionary graph framework for analyzing fast evolving networks. *Journal of Big Data*, 6(1), 1-24.
- [46] Devaraj, A., Megahed, M., Liu, Y., Ramachandran, A., & Anand, T. (2019). A switched capacitor multiple input single output energy harvester (solar+ piezo) achieving 74.6% efficiency with simultaneous MPPT. *IEEE Transactions on Circuits and Systems I: Regular Papers*, 66(12), 4876-4887.
- [47] Bandyopadhyay, S., & Chandrakasan, A. P. (2012). Platform architecture for solar, thermal, and vibration energy combining with MPPT and single inductor. *IEEE Journal of Solid-State Circuits*, 47(9), 2199-2215.
- [48] Wan, Q., & Mok, P. K. (2019). A 14-nA, highly efficient triple-output thermoelectric energy harvesting system based on a reconfigurable TEG array. *IEEE Journal of Solid-State Circuits*, 54(6), 1720-1732.
- [49] Ramadass, Y. K., & Chandrakasan, A. P. (2010). A battery-less thermoelectric energy harvesting interface circuit with 35 mV startup voltage. *IEEE Journal of Solid-State Circuits*, 46(1), 333-341.
- [50] Ouda, M. H., Arsalan, M., Marnat, L., Shamim, A., & Salama, K. N. (2013). 5.2-GHz RF power harvester in 0.18- $\mu\text{m}$  CMOS for implantable intraocular pressure monitoring. *IEEE Transactions on Microwave Theory and Techniques*, 61(5), 2177-2184.
- [51] Torfs, T., Leonov, V., Yazicioglu, R. F., Merken, P., Van Hoof, C., Vullers, R. J., & Gyselinckx, B. (2008, October). Wearable autonomous wireless electro-encephalography system fully powered by human body heat. In *SENSORS, 2008 IEEE* (pp. 1269-1272). IEEE.
- [52] Beker, L., Benet, A., Meybodi, A. T., Eovino, B., Pisano, A. P., & Lin, L. (2017). Energy harvesting from cerebrospinal fluid pressure fluctuations for self-powered neural implants. *Biomedical Microdevices*, 19(2), 1-9.
- [53] Mercier, P. P., Lysaght, A. C., Bandyopadhyay, S., Chandrakasan, A. P., & Stankovic, K. M. (2012). Energy extraction from the biologic battery in the inner ear. *Nature Biotechnology*, 30(12), 1240-1243.
- [54] Sudevalayam, S., & Kulkarni, P. (2010). Energy harvesting sensor nodes: Survey and implications. *IEEE Communications Surveys & Tutorials*, 13(3), 443-461.
- [55] Paradiso, J. A., & Feldmeier, M. (2001, September). A compact, wireless, self-powered pushbutton controller. In *International Conference on Ubiquitous Computing* (pp. 299-304). Springer, Berlin, Heidelberg.
- [56] Zhang, Y. et al. (2012). A batteryless 19  $\mu\text{W}$  MICS/ISM-Band energy harvesting body sensor node SoC for ExG applications. *IEEE Journal of Solid-State Circuits*, 48(1), 199-213.
- [57] Lhermet, H., Condemine, C., Plissonnier, M., Salot, R., Audebert, P., & Rosset, M. (2008). Efficient power management circuit: From thermal energy harvesting to above-IC microbattery energy storage. *IEEE Journal of Solid-State Circuits*, 43(1), 246-255.
- [58] Shrivastava, A., Roberts, N. E., Khan, O. U., Wentzloff, D. D., & Calhoun, B. H. (2015). A 10 mV-input boost convert-

- er with inductor peak current control and zero detection for thermoelectric and solar energy harvesting with 220 mV cold-start and  $-14.5$  dBm, 915 MHz RF kick-start. *IEEE Journal of Solid-State Circuits*, 50(8), 1820-1832.
- [59] Yu, X., Ergun, K., Cherkasova, L., & Rosing, T. Š. (2020). Optimizing sensor deployment and maintenance costs for large-scale environmental monitoring. *IEEE Transactions on Computer-Aided Design of Integrated Circuits and Systems*, 39(11), 3918-3930.
- [60] Shah, N., Lajevardi, P., Wojciechowski, K., Lang, C., & Murmann, B. (2019). An energy harvester using image sensor pixels with cold start and over 96% MPPT efficiency. *IEEE Solid-State Circuits Letters*, 2(9), 207-210.
- [61] Kadirvel, K. et al. (2012, February). A 330nA energy-harvesting charger with battery management for solar and thermoelectric energy harvesting. In *2012 IEEE International Solid-State Circuits Conference* (pp. 106-108). IEEE.
- [62] Ahmed, K. Z. et al. (2020). A variation-adaptive integrated computational digital LDO in 22-nm CMOS with fast transient response. *IEEE Journal of Solid-State Circuits*, 55(4), 977-987.
- [63] Lee, Y. J. et al. (2016). A 200-mA digital low drop-out regulator with coarse-fine dual loop in mobile application processor. *IEEE Journal of Solid-State Circuits*, 52(1), 64-76.
- [64] Rahman, F. et al. (2019). A unified clock and switched-capacitor-based power delivery architecture for variation tolerance in low-voltage SoC domains. *IEEE Journal of Solid-State Circuits*, 54(4), 1173-1184.
- [65] Amin, S. S., & Mercier, P. P. (2018). MISIMO: A multi-input single-inductor multi-output energy harvesting platform in 28-nm FDSOI for powering net-zero-energy systems. *IEEE Journal of Solid-State Circuits*, 53(12), 3407-3419.
- [66] Shrivastava, A., Ramadass, Y. K., Khanna, S., Bartling, S., & Calhoun, B. H. (2014, June). A 1.2  $\mu$ W SIMO energy harvesting and power management unit with constant peak inductor current control achieving 83–92% efficiency across wide input and output voltages. In *2014 Symposium on VLSI Circuits Digest of Technical Papers* (pp. 1-2). IEEE.
- [67] Krippendorff, K. (2009). Ross Ashby's information theory: a bit of history, some solutions to problems, and what we face today. *International Journal of General Systems*, 38(2), 189-212.
- [68] "IEEE SA - Internet of Things Related Standards." [Online]. Available: <https://standards.ieee.org/ieee/2413/6226/>
- [69] Liu, X., & Ansari, N. (2019). Toward green IoT: Energy solutions and key challenges. *IEEE Communications Magazine*, 57(3), 104-110.
- [70] Sanislav, T., Mois, G. D., Zeadally, S., & Folea, S. C. (2021). Energy harvesting techniques for internet of things (IoT). *IEEE Access*, 9, 39530-39549.

# Low-power and High-Frequency Optogenetic Retinal Prostheses with ChRmine

Himanshu Bansal, Neha Gupta and Sukhdev Roy\*

Department of Physics and Computer Science,  
Dayalbagh Educational Institute, Agra, 282005, India

*Optogenetics has emerged as a promising technique in the field of retinal prostheses as new potent opsins with high light-sensitivity, red-shifted activation wavelength and large photocurrent have been discovered or engineered in the last decade. In the present study, a detailed theoretical analysis of optogenetic excitation of retinal ganglion neurons using already studied ChR2 opsin and ChRmine, the newly discovered, red-shifted opsin has been carried out. The theoretical models have been validated by comparing theoretical simulations with reported experimental results. Minimum pulse width required to achieve peak photocurrent at different irradiances in each opsin has been determined that is useful to optimize light power. The study reveals that ChRmine can evoke high-fidelity spiking upto 35 Hz, whereas ChR2 fails above 10 Hz. Also, the required power of each light pulse in ChRmine is three orders of magnitude smaller than ChR2. The present study highlights the importance of ChRmine as a potential opsin for low-power and high-frequency optogenetic retinal prostheses.*

**Keywords – Neurophotronics, Optogenetics, Retinal prostheses, ChRmine**

## I. INTRODUCTION

Retinal degenerative diseases that include retinitis pigmentosa and macular degeneration, caused due to dysfunction of rod and cone photoreceptors in the retina, are the leading cause of vision loss. Studies have shown that in absence of these functional photoreceptors, inner retinal neurons can retain functionality and connections to the brain [1], [2]. Earlier efforts have shown that electrical stimulation of inner retinal neurons enables patients to recover some visual perception and even perform some reading task [3], [4]. However, electrical prosthetic devices do not yet allow sufficient spatial resolution for face recognition and are invasive in nature [1], [5], [6].

In the last decade, optogenetics has provided opportunities for a wide-range of applications in and beyond neuroscience including retinal prostheses [7]-[9]. In optogenetics, light-sensitive proteins are expressed transgenically in neurons to mediate light-dependent transport of ions across the membrane and to excite or inhibit neural activity by causing depolarization or hyperpolarization of the neurons, respectively [10], [11]. Since the first use of Channelrhodopsin-2 (ChR2) in thalamic projecting neurons to restore light response in blind mice, a dozen of new opsins have been tested [5], [12]-[16]. Recently, screening guided by crystal structure derived knowledge of residues forming the cation-conducting ChR pore, revealed ~1000 suitable

new cation-conducting ChR sequences [17]. Optimization of these sequences for mammalian expression resulted in a promising marine opsin gene, named ChRmine from *Tiarina fusus* [18]. Expression of ChRmine in cultured hippocampal neurons has been reported to give rise to a very large inward photocurrent ~ 4 nA at red-shifted excitable wavelength. Along with high light sensitivity, recovery from de-sensitization of photocurrent in ChRmine in darkness is reported to be an order of magnitude faster than for other red-shifted opsins [18]. Computational studies of optogenetic systems have provided a better understanding of photocurrent generation in the opsin molecule as well as spiking in different opsin-expressing neurons [19]-[24]. The computational models can help to virtually analyze different combinations between opsins (~ more than hundreds), and target cell types. Thus, it is extremely important to develop a theoretical framework of the biophysical mechanism of optogenetic excitation of retinal neurons expressed with already tested opsin, namely, ChR2 and also newly discovered potential opsin, ChRmine. The objective of this paper is to (i) formulate accurate theoretical models of the photocurrent in ChR2 and ChRmine, (ii) study the effect of photostimulation parameters that include irradiance, pulse width, and pulse frequency, (iii) develop integrated neuron circuit models to accurately simulate optogenetic excitation in these opsin-expressing retinal ganglion neurons, and (iv) compare and determine optimized photostimulation conditions for optogenetic retinal prostheses.

\*Corresponding author: [sukhdevroy@dei.ac.in](mailto:sukhdevroy@dei.ac.in)

ISSN 0972-5032 (P); Copyright ©2022, SSI

## II. THEORETICAL MODEL

In presence of light, all the microbial opsins, used inoprogenetics, isomerize from all-*trans* to 13-*cis* conformation and initiate a photocycle with different intermediates [25]-[28]. Some of these intermediates transport ions across the neuron membrane, and thus lead to change in membrane potential [29], [30].

### A. Model for Opsin Photocurrent

The photocurrent through these opsin channels ( $I_{opsin}$ ) can be expressed as,

$$I_{opsin} = g_{opsin}(V - E_{opsin}) \quad (1)$$

where,  $opsin \equiv$  ChR2 or ChRmine,  $V$  is the membrane potential and,  $g_{opsin}$  and  $E_{opsin}$  are the conductance and reversal potential of each opsin [22], [23]. In general,  $g_{opsin}$  depends on time ( $t$ ), photon flux per unit area per unit time ( $\phi$ ), wavelength ( $\lambda$ ), local concentration of specific ions across the membrane ( $M$ ), and temperature ( $T$ ) [22], [23]. We consider the conductance to be defined as,  $g_i = g_{oi} f(\phi, \lambda, t)$ , where,  $g_{oi}$  accounts for both the maximum conductance of single-channel and expression density and  $f(\phi, \lambda, t)$  is a normalized light-dependent function.

The biphasic decay of photocurrent in both ChR2 and ChRmine indicates that their photocycles have two conducting states with different lifetimes [12], [18]. A 4-state model consisting of two closed non-conducting and two open conducting states has been considered to model their photocurrent [21]. The photo-thermal transitions among these states can be described by the following set of rate equations,

$$\dot{C}_1 = G_{a1}O_1 + G_rC_2 - G_{a1}(\phi)C_1 \quad (2)$$

$$\dot{O}_1 = G_{a1}(\phi)C_1 + G_b(\phi)O_2 - (G_{d1} + G_f(\phi))O_1 \quad (3)$$

$$\dot{O}_2 = G_{a2}(\phi)C_2 + G_f(\phi)O_1 - (G_{d2} + G_b(\phi))O_2 \quad (4)$$

$$\dot{C}_2 = G_{d2}O_2 - (G_r + G_{a2}(\phi))C_2 \quad (5)$$

where,  $C_1 + O_1 + O_2 + C_2 = 1$ . The transitions of molecules from  $C_1 \rightarrow O_1$ ,  $C_2 \rightarrow O_2$ ,  $O_1 \rightarrow C_1$ ,  $O_2 \rightarrow C_2$ ,  $O_1 \rightarrow O_2$ ,  $O_2 \rightarrow O_1$  and  $C_2 \rightarrow C_1$  have been described by the rate constants  $G_{a1}$ ,  $G_{a2}$ ,  $G_{d1}$ ,  $G_{d2}$ ,  $G_f$ ,  $G_b$  and  $G_r$ , respectively. These rate constants have been determined from experimental data and defined as  $G_{a1}(\phi) = \epsilon k_1 \phi^p / (\phi^p + \phi_m^p)$ ,  $G_{a2}(\phi) = \epsilon k_2 \phi^p / (\phi^p + \phi_m^p)$ ,  $G_f(\phi) = G_{f0} + \epsilon k_f \phi^q / (\phi^q + \phi_m^q)$ ,  $G_b(\phi) = G_{b0} + \epsilon k_b \phi^q / (\phi^q + \phi_m^q)$  [21], [31]. The values of parameters used in the model have been determined from reported experiments [12], [18], [31].

### B. Model for Optogenetic Excitation in ChR2/ChRmine-expressing Retinal Ganglion Neurons

Light-evoked voltage responses of opsin-expressing

neurons can be theoretically studied by integrating the photocurrent kinetics of opsin channels with biophysical circuit model of neurons [21]. The Fohlmeister and Miller circuit model has been used to simulate the voltage response of retinal ganglion neurons [32]. The rate of change in membrane voltage with time in presence of opsin-mediated photocurrent can be expressed as,

$$C_m \dot{V} = -I_i - I_{KCa} - I_L + I_{opsin} \quad (6)$$

where,  $I_i = I_{Na} + I_K + I_{KA} + I_{Ca}$ . Each ion-channel current in  $I_i$  has been modelled as,  $I_i = g_i m^p h^q (V - E_i)$ , where  $g_i$  is maximal conductance,  $m$  is activation variable (with exponent  $p$ ),  $h$  is inactivation variable (with exponent  $q$ ), and  $E_i$  is the reversal potential [31]-[33]. The kinetic equation for each of the gating functions  $x$  ( $m$  or  $h$ ) obeys the first-order kinetics as  $\dot{x} = -(\alpha_x + \beta_x)x + \alpha_x$ . The voltage-dependent functions ( $\alpha_x$  and  $\beta_x$ ) and the values of various parameters for the model have been taken from Refs. [31]-[33].  $I_L = g_L(V - E_L)$  and  $I_{KCa} = g_{KCa}(V - E_{Ca})$ , where  $E_{Ca}$  is modelled as a variable according to the Nernst equation as,

$$E_{Ca} = \frac{RT}{2F} \ln \left[ \frac{[Ca^{2+}]_e}{[Ca^{2+}]_i(t)} \right] \quad (7)$$

where,  $[Ca^{2+}]_e$  and  $[Ca^{2+}]_i$  are extracellular and intracellular  $Ca^{2+}$  concentrations, respectively.  $R$  is gas constant,  $F$  is Faraday constant and  $T = 22$  °C. The rate of change in  $[Ca^{2+}]_i$  is expressed as,

$$[Ca^{2+}]_i = \frac{-3 I_{Ca}}{2Fr} - \frac{([Ca^{2+}]_i - [Ca^{2+}]_{res})}{\tau_{Ca}} \quad (8)$$

where,  $[Ca^{2+}]_{res}$  is the residual level concentration, and  $\tau_{Ca}$  is calcium removal times. The  $g_{KCa}$  is ligand-gated conductance and varies according to the equation,

$$g_{KCa} = \bar{g}_{KCa} \frac{([Ca^{2+}]_i/[Ca^{2+}]_{diss})^2}{1 + ([Ca^{2+}]_i/[Ca^{2+}]_{diss})^2} \quad (9)$$

where,  $[Ca^{2+}]_{diss}$  is dissociation constant ( $= 10^{-3}$  mM) [31]-[33].

## III. RESULTS

The photoresponse of ChR2 and ChRmine has been studied through numerical simulation using Eqns. (1)-(5). The formulated model of optogenetic control with ChR2 and ChRmine has been validated by comparing simulated values with reported experimental values as shown in Table I [12],[18]. The photocurrents in ChR2 at different photon flux densities have been shown in Fig. 1. The photocurrent in ChRmine at different photon flux densities is shown in Fig. 2. It is evident from Figs. 1 and 2 that

the photocurrent in ChRmine is much larger than ChR2, even at very low irradiances. To optimize light powers, minimum pulse width required to achieve peak photocurrent *i.e.* saturating pulse width (SPW) has been determined (Fig. 3). The study reveals that at lower irradiances, ChRmine requires smaller pulse widths in comparison to ChR2. Optogenetically evoked spiking in each opsin-expressing retinal neuron has been studied through numerical simulations using Eqns. (1)-(9). Variation of average firing frequency with photon flux density under continuous illumination, in ChR2 and ChRmine-expressing retinal ganglion neurons has been shown in Fig. 4. ChRmine is able to evoke very high-frequency firing at very low irradiances. However, the firing frequency drops at higher photon fluxes in ChRmine. To get high-frequency control, the photostimulation parameters have been optimized. The analysis shows that ChRmine can evoke spiking upto 35 Hz with 100% fidelity, while ChR2 fails above 10 Hz (Fig. 5).

TABLE I  
COMPARISON OF EXPERIMENTAL AND THEORETICAL PHOTOCURRENT CHARACTERISTICS

ChR2		
$\phi = 1.8e+16 \text{ ph. mm}^{-2} \text{ s}^{-1}$ at 460 nm	Experimental value [12]	Simulated value
Peak photocurrent	295 pA	297 pA
Plateau Photocurrent	82 pA	72 pA
ChRmine		
$\phi = 2.06e+15 \text{ ph. mm}^{-2} \text{ s}^{-2}$ at 585 nm	Experimental value [18]	Theoretical value
Peak photocurrent	5.6 nA	5.52 nA
Plateau Photocurrent	1.28 nA	1.33 nA

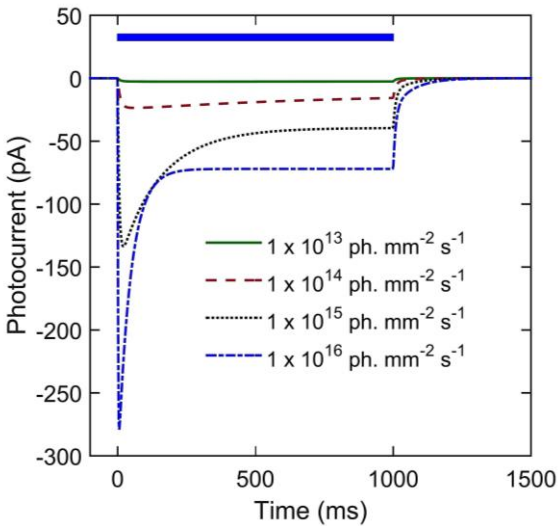


Fig. 1. Theoretically simulated photocurrent in ChR2 under 1 s light pulse at indicated photon flux at 460 nm.

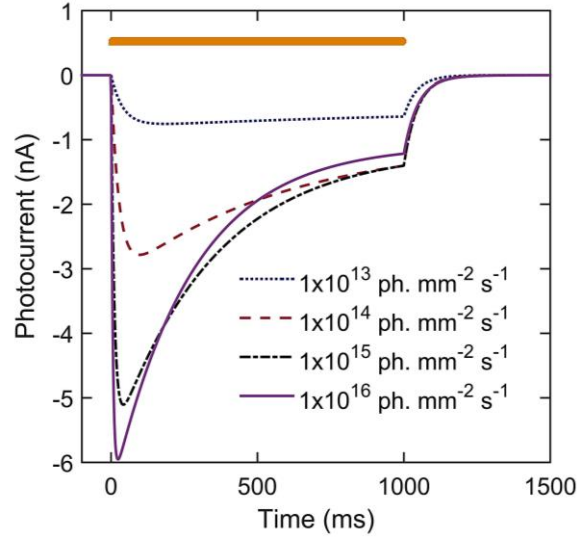


Fig. 2. Theoretically simulated photocurrent in ChRmine under 1 s light pulse at indicated photon flux at 585 nm.

Also, the required light power of each light pulse in ChRmine is three orders of magnitude lower in comparison to ChR2 (Fig. 5). The use of red-shifted wavelength with ChRmine further enhances its utility over blue light with ChR2.

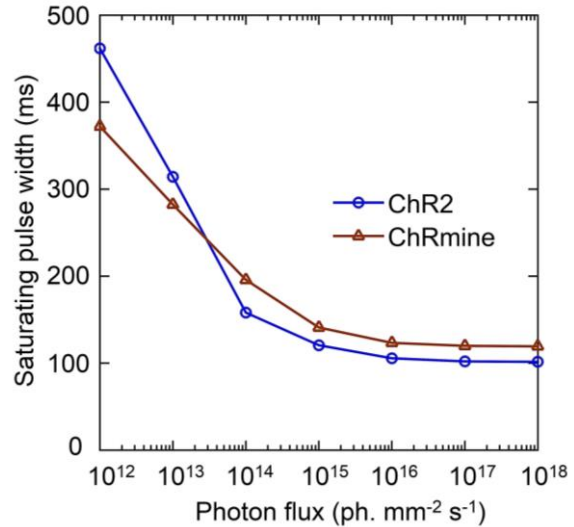


Fig. 3. Theoretically simulated variation of minimum pulse width required to achieve peak photocurrent (SPW) with photon flux at wavelength 460 nm and 590 nm in ChR2 and ChRmine, respectively.

#### IV. DISCUSSION

The theoretical models accurately simulate reported experimental results, and provide useful insights to determine optimized conditions for low-power and high-frequency optogenetic excitation in retinal ganglion neurons. The analysis reveals that ChRmine significantly

improves the intensity range for excitation along with temporal resolution at higher frequencies. In the present study, determination of SPW in both ChR2 and ChRmine would be helpful in optimizing light powers (Fig. 3).

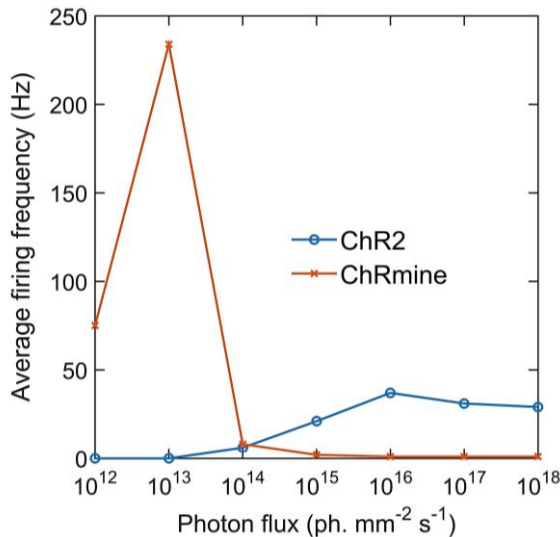


Fig. 4. Theoretically simulated variation of average firing frequency with photon flux in ChR2 and ChRmine expressing retinal ganglion neurons, under 1 s light illumination at wavelength of 460 nm and 590 nm for ChR2 and ChRmine, respectively.

To probe phenomena related to precise spike timing and high-frequency neural events, various new opsins with faster turn-off kinetics have provided temporal precision upto sub-millisecond [33]-[35]. The high-frequency limit of ChRmine-expressing retinal neurons (35 Hz) is much higher than ChR2 (Fig. 5). A major limitation with electrical prosthetic stimulation to restore visual activity is that it cannot selectively activate the ON/OFF visual pathways, and thus results in ambiguous encoding of visual information [36], [37]. In optogenetics, bidirectional control *i.e.* depolarization and hyperpolarization, both can be achieved by co-expressing excitatory and inhibitory opsins in a single neuron and subsequently by just changing the wavelength of illumination light [21], [38]. In a recent study, various possible opsin-pairs have been analysed based on spectral compatibility, light-sensitivity, photocurrent amplitude and kinetics, and suitability for different applications [21]. In combination with blue-light activated anion channel namely GtACR2, the presently studied red-shifted excitatory opsin ChRmine would restore retinal ON/OFF pathway at much lower intensities. In the present study, we have considered a 4-state model to describe photocurrent in various opsins. Although a six-state model for ChR2 has also been reported by considering transitions involved in retinal isomerization, it does not influence results under pulses longer than ~ ms [39], [40]. Also, the reported experimental results with ChRmine are inadequate to formulate such models with more number of states [18]. The

proposed theoretical models of photocurrent in ChRmine can also be integrated with the circuit models of other cell types to quickly predict their behavior through simulations. Such comparative studies are useful not only for finding new opsins and interpreting complex experimental results but also to design optogenetic neuroprosthetic devices and circuits, especially for retinal prostheses.

## V. ACKNOWLEDGMENTS

The authors express their gratitude to Professor P. S. Satsangi for his kind inspiration and encouragement. They also acknowledge the University Grants Commission, India, for the Special Assistance Programme Grant No. [F.530/14/DRS-III/2015(SAP-I)]. H.B. is grateful to the DST, India, for the award of the INSPIRE Fellowship (DST/INSPIRE/03/2017/003087).

## REFERENCES

- [1] Baker, C. K., & Flannery, J. G. (2018). Innovative optogenetic strategies for vision restoration. *Frontiers in Cellular Neuroscience*, 12, 316. <https://doi.org/10.3389/fncel.2018.00316>
- [2] Kleinlogel, S., Vogl, C., Jeschke, M., Neef J., & Moser, T. (2020). Emerging approaches for restoration of hearing and vision. *Physiological Reviews*, 100(4), 1467-1525. <https://doi.org/10.1152/physrev.00035.2019>
- [3] Margalit, E., et al. (2002). Retinal prosthesis for the blind. *Survey of Ophthalmology*, 47(4), 335-356. [https://doi.org/10.1016/S0039-6257\(02\)00311-9](https://doi.org/10.1016/S0039-6257(02)00311-9)
- [4] Humayun, M. S., et al. (2012). Interim results from the international trial of Second Sight's visual prosthesis. *Ophthalmology*, 119(4), 779-788. <https://doi.org/10.1016/j.ophtha.2011.09.028>
- [5] Chaffiol, A., et al. (2017). A new promoter allows optogenetic vision restoration with enhanced sensitivity in macaque retina. *Molecular Therapy*, 25(11), 2546-2560. <https://doi.org/10.1016/j.ymthe.2017.07.011>
- [6] Lorach, H., et al. (2015). Photovoltaic restoration of sight with high visual acuity. *Nature Medicine*, 21, 476-482. <https://doi.org/10.1038/nm.3851>
- [7] Pan, Z. H., Lu, Q., Bi, A., Dizhoor, A. M., & Abrams, G. W. (2015). Optogenetic approaches to restoring vision. *Annual Review of Vision Science*, 1, 185-210. <https://doi.org/10.1146/annurev-vision-082114-035532>
- [8] Ferenczi, E. A., Tan, X., & Huang, C. L. (2019). Principles of optogenetic methods and their application to cardiac experimental systems. *Frontiers in Physiology*, 10, 1096. <https://doi.org/10.3389/fphys.2019.01096>
- [9] Simon, C. J., Sahel, J. A., Duebel, J., Herlitze S., & Dalkara, D. (2020). Opsins for vision restoration. *Biochemical and Biophysical Research Communications*, 527, 325-330. <https://doi.org/10.1016/j.bbrc.2019.12.117>
- [10] Nagel, G., et al. (2003). Channelrhodopsin-2, a directly light-gated cation-selective membrane channel. *PNAS*, 100(24), 13940-13945. <https://doi.org/10.1073/pnas.1936192100>
- [11] Boyden, E. S., Zhang, F., Bamberg, E., Nagel G., & Deisseroth, K., (2005). Millisecond-timescale, genetically targeted optical control of neural activity. *Nature*

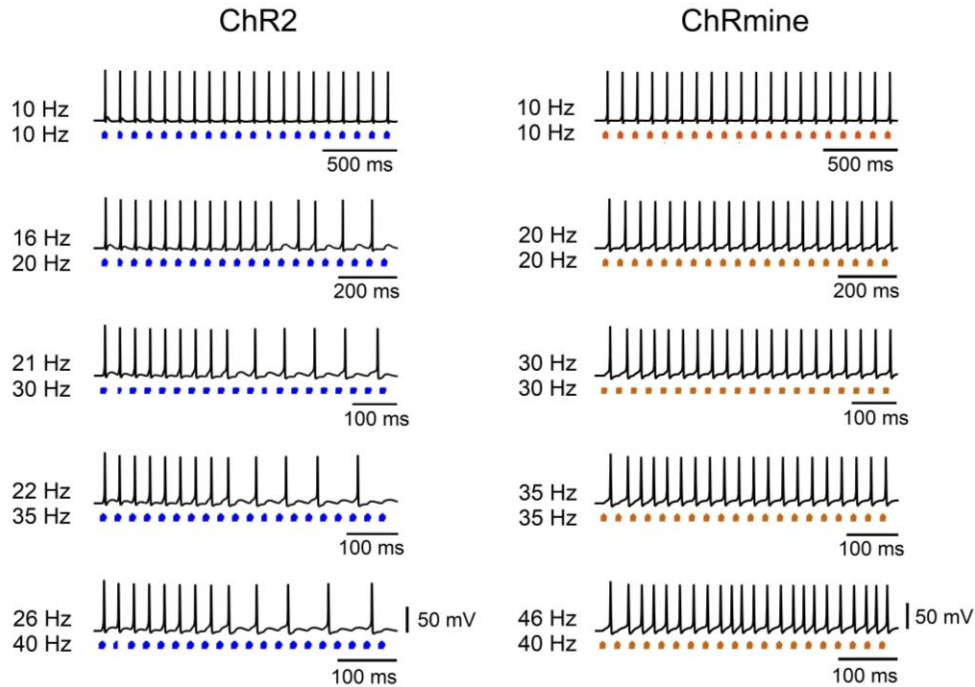


**Fig. 5. High-frequency optogenetic control with high fidelity in ChR2 and ChRmine-expressing retinal ganglion neurons. Variation of membrane potential with time under 20 opto-stimulations each of 2.5 ms at 5 mW/mm<sup>2</sup> (460 nm) for ChR2 and 0.98 ms at 0.013 mW/mm<sup>2</sup> (590 nm) for ChRmine. Upper and lower frequencies are showing stimulation frequency and spiking frequency respectively.**

*Neuroscience*, 8(9), 1263-1268.  
<https://doi.org/10.1038/nn1525>

[12] Bi, A., Cui, J., Ma, Y. P., Olshevskaya, E., Pu, M., Dizhoor, A. M., & Pan, H. N. (2006). Ectopic expression of a microbial-type rhodopsin restores visual responses in mice with photoreceptor degeneration. *Neuron*, 50, 23-33. <https://doi.org/10.1016/j.neuron.2006.02.026>

[13] Kleinlogel, S. et al., (2011). Ultra light-sensitive and fast neuronal activation with the Ca<sup>2+</sup> permeable channel rhodopsin CatCh. *Nature Neuroscience*, 14, 513-518. <https://doi.org/10.1038/nn.2776>

[14] Sengupta, A. et al. (2016). Red-shifted channelrhodopsin stimulation restores light responses in blind mice, macaque retina, and human retina. *EMBO Molecular Medicine*, 8(11), 1248-1264. <https://doi.org/10.15252/emmm.201505699>

[15] Ganjawala, T. H., Lu, Q., Fenner, M. D., Abrams, G. W., & Pan, Z. H. (2019). Improved CoChR variants restore visual acuity and contrast sensitivity in a mouse model of blindness under ambient light conditions. *Molecular Therapy*, 27(6), 1195-1205. <https://doi.org/10.1016/j.ymthe.2019.04.002>

[16] Gauvain, G. et al. (2021). Optogenetic therapy: high spatiotemporal resolution and pattern discrimination compatible with vision restoration in non-human primates. *Communication Biology*, 4, 125. <https://doi.org/10.1038/s42003-020-01594-w>

[17] Keeling, P. J. (2017). The Marine Microbial Eukaryote Transcriptome Sequencing Project (MMETSP): Illuminating the functional diversity of eukaryotic life in the oceans through transcriptome sequencing. *PLOS Biology*, 12, e1001889. <https://doi.org/10.1371/journal.pbio.1001889>

[18] Marshel, J. H., Kim, Y. S., Machado, T. A., Quirin, S., Benson, B., et al. (2019). Cortical layer-specific critical dynamics triggering perception. *Science*, 365, eaaw5202. <https://doi.org/10.1126/science.aaw5202>

[19] Boyle, P. M., Williams, J. C., Ambrosi, C. M., Entcheva, E., & Trayanova, N. A. (2013). A comprehensive multiscale framework for simulating optogenetics in the heart. *Nature Communication*, 4, 1-9. <https://doi.org/10.1038/ncomms3370>

[20] Bansal, H., Gupta, N., & Roy, S. (2020). Comparison of low-power, high frequency and temporally precise optogenetic inhibition of spiking in NpHR, eNpHR3.0 and Jaws-expressing neurons. *Biomedical Physics & Engineering Express*, 6(4), 045011. <https://doi.org/10.1088/2057-1976/ab90a1>

[21] Bansal, H., Gupta, N., & Roy, S. (2020). Theoretical Analysis of Low-power Bidirectional Optogenetic Control of High-frequency Neural Codes with Single Spike Resolution. *Neuroscience*, 449, 165-188. <https://doi.org/10.1016/j.neuroscience.2020.09.022>

[22] Saran, S., Gupta, N., & Roy, S. (2018). Theoretical analysis of low-power fast optogenetic control of firing of Chronos-expressing neurons. *Neurophotonics*, 5(2), 025009. <https://doi.org/10.1117/1.NPh.5.2.025009>

- [23] Gupta, N., Bansal, H., & Roy, S. (2019). Theoretical optimization of highfrequency optogenetic spiking of red-shifted very fast-Chrimson expressing neurons *Neurophotonics*, 6(2), 025002. <https://doi.org/10.1117/1.NPh.6.2.025002>
- [24] Hart, W., et al. (2020). Combined optogenetic and electrical stimulation of auditory neurons increases effective stimulation frequency-an in vitro study. *Journal of Neural Engineering*, 17, 016069. <https://doi.org/10.1088/1741-2552/ab6a68>
- [25] Engelhard, C., Chizhov, I., Siebert F., & Engelhard, M. (2018). Microbial halorhodopsins: Light-driven chloride pumps. *Chemical Reviews*, 118(21), 10629-10645. <https://doi.org/10.1021/acs.chemrev.7b00715>
- [26] Roy, S., & Yadav, C. (2014). All-optical sub-ps switching and parallel logic gates with bacteriorhodopsin (BR) protein and BR-gold nanoparticles. *Laser Physics Letters*, 11(12), 12590. <https://doi.org/10.1088/1612-2011/11/12/125901>
- [27] Roy, S., Kikukawa, T., Sharma, P., & Kamo N. (2006). All-optical switching in pharaonis phoborhodopsin protein molecules. *IEEE Transactions on NanoBioscience*, 5(3), 178-187. <https://doi.org/10.1109/TNB.2006.880828>
- [28] Roy, S., Singh, C. P., & Reddy, K. J. P. (2001). Generalized model for all-optical light modulation in bacterio rhodopsin. *Journal of Applied Physics*, 90(8), 3679-3688. <https://doi.org/10.1063/1.1403679>
- [29] Deisseroth, K. (2015). Optogenetics: 10 years of microbial opsins in neuroscience, *Nature Neuroscience*, 18(9), 1213-1225. <https://doi.org/10.1038/nn.4091>
- [30] Kuhne, J., et al. (2019). Unifying photocycle model for light adaptation and temporal evolution of cation conductance in channelrhodopsin-2. *PNAS*, 116, 9380-9389. <https://doi.org/10.1073/pnas.1818707116>
- [31] Bansal H., Gupta N., & Roy S. (2021). Theoretical analysis of optogenetic spiking with ChRmine, bReaChES and CsChrimson-expressing neurons for retinal prostheses. *Journal of Neural Engineering*, 18(4). <https://doi.org/10.1088/1741-2552/ac1175>
- [32] Fohlmeister, J. F., Coleman, P. A., & Miller, R. F. (1990). Modeling the repetitive firing of retinal ganglion cells. *Brain Research*, 510(2), 343-345. [https://doi.org/10.1016/0006-8993\(90\)91388-w](https://doi.org/10.1016/0006-8993(90)91388-w)
- [33] Fohlmeister, J. F., & Miller, R. F. (1997). Impulse encoding mechanisms of ganglion cells in the tiger salamander retina. *Journal of Neurophysiology*, 78(4), 1935-1947. <https://doi.org/10.1152/jn.1997.78.4.1935>
- [34] Ronzitti, E., et al. (2017). Submillisecond optogenetic control of neuronal firing with two-photon holographic photoactivation of chronos. *Journal of Neuroscience*, 37(44), 10679-10689. <https://doi.org/10.1523/JNEUROSCI.1246-17.2017>
- [35] Mager, T., et al. (2018). High frequency neural spiking and auditory signaling by ultrafast red-shifted optogenetics. *Nature Communications*, 9(1), 1750. <https://doi.org/10.1038/s41467-018-04146-3>
- [36] Guo, T., et al. (2018). Closed-loop efficient searching of optimal electrical stimulation parameters for preferential excitation of retinal ganglion cells. *Frontiers in Neuroscience*, 12, 168. <https://doi.org/10.3389/fnins.2018.00168>
- [37] Beyeler, M., Rokem, A., Boynton, G. M., & I. Fine, (2017). Learning to see again: biological constraints on cortical plasticity and the implications for sight restoration technologies. *Journal of Neural Engineering*, 14(5), 051003. <https://doi.org/10.1088/1741-2552/aa795e>
- [38] Zhang, F., et al. (2007). Multimodal fast optical interrogation of neural circuitry. *Nature*, 446, 633-639. <https://doi.org/10.1038/nature05744>
- [39] Grossman, N., Simiaki, V., Martinet, C., Toumazou, C., Schultz, S. R., & Nikolic, K. (2013). The spatial pattern of light determines the kinetics and modulates backpropagation of optogenetic action potentials. *Journal of Computational Neuroscience*, 34, 477-488. <https://doi.org/10.1007/s10827-012-0431-7>
- [40] Evans, B. D., Jarvis, S., Schultz, S. R., & Nikolic, K. (2016). PyRhO: a multiscale optogenetics simulation platform. *Frontiers in Neuroinformatics*, 10, 8. <https://doi.org/10.3389/fninf.2016.0000>

# Deep Feature Compression Based Ensemble Model Towards Content Based Image Retrieval

Rohan Raju Dhanakshirur<sup>1\*</sup> and Prem Kumar Kalra<sup>2</sup>

<sup>1</sup> Amar Nath and Shashi Khosla School of Information Technology,

<sup>2</sup> Department of Computer Science and Engineering,  
Indian Institute of Technology Delhi, New Delhi, India

*Recent advances in the field of technology have led to increased availability of image datasets. This has motivated the need for an efficient Content-Based Image Retrieval (CBIR) algorithm. Most of the present-day algorithms make use of classical image processing-based techniques for feature extraction, a major step in CBIR. In this paper, we propose a learning based ensemble algorithm for efficient feature extraction. The classical texture features and the compressed version of the parameters learnt by the latent space representation of the deep autoencoder are ensemble in the proposed algorithm. We fuse similarity distance and Euclidean distance between the extracted ensemble feature of the query image and the images in the database to retrieve relevant images. We demonstrate the efficiency of the proposed algorithm on the standard ukBench dataset using different quantitative parameters. We observe the proposed algorithm to be 96.7% accurate, which is 3.2% better than the best performing state-of-the-art algorithms.*

**Keywords** – Image retrieval, Deep autoencoder, Discrete Cosine Transforms (DCT), Ensemble model

## I. INTRODUCTION

With the advent of various social networking sites, it is observed that 300 million photos are uploaded in the public domain every day [1]. This has given rise to the need for an efficient image retrieval algorithm. The process of image retrieval can be defined as the act of fetching the most relevant image from the database. The query can be in terms of text, speech or in the form of an image [2]. When an image is given as a query, the task of any image retrieval algorithm would be to fetch that image from the database, whose content is most similar to the content of the query image. This process is thus, defined as Content Based Image Retrieval (CBIR). CBIR is not a new problem. It has been in the limelight since 1990s [3]. However, it is still an important problem that attracts attention from various scientific communities such as computer vision and multimedia due to the fact that the total data in the domain has significantly increased. The traditional technique of listing the meta data of the image in the form of titles and tags [1] cannot be used anymore because there can be inconsistencies in the visual content and the corresponding textual content. Moreover, this introduces the problem of intention gap. Intention gap is the difficulty, a user faces in precisely expressing his intent through words. Modern day

techniques focus on extracting some texture features from the query image and trying to match them with the corresponding features of the images in the database [4]. Although these techniques solve the problem of intention gap, they introduce a new problem called as the semantic gap. Semantic gap is the difficulty in describing high-level semantic concepts corresponding to the content of the image with low-level visual features [5]. Various efforts have been put in by researchers to narrow down this gap. Deep autoencoders are found to be very efficient in reducing the semantic gap [6]. However, they may make the system completely non-interpretable and susceptible to adversarial attacks [7]. In order to reduce the risk of adversarial attacks, it is necessary to fuse the output of the deep autoencoders with some classical hand-crafted features.

## II. RELATED WORK

Major steps involved in Content Based Image Retrieval (CBIR) are:

- i. Feature extraction and transforming feature vectors of various sizes to a fixed-length vector.
- ii. Computing similarity between two feature vectors.

### A. Feature Extraction

The early time CBIR algorithms focus upon hand-crafted features. They describe image content by shape [8],

\* Corresponding author: rohanrd@cse.iitd.ac.in  
ISSN 0972-5032 (P); Copyright ©2022, SSI

structure, color, and texture [9] related features. Gist as feature descriptors offer a low computation complexity and are also used by some researchers [10], [32]. These algorithms typically find their use cases in datasets that have simple images. These images tend to fail whenever there is a background clutter in the query image [1].

The introduction of Scale Invariant Feature Transforms (SIFT) [11] changed the feature extraction techniques. Various techniques make use of SIFT descriptors for feature detection. Attempts have been made to improve to SIFT key point detectors through algorithms such as Hessian affine detector [12], Maximally Stable External Regions (MSER) [13], Harris-Hessian detector [14], and Features from Accelerated Segment Test (FAST) [15]. Efforts have also been done in extracting the features by simply sampling the image [16], [31]. Apart from the regular hand-crafted features, researchers have also come up with learning-based features similar to that of local feature descriptors [17]. The last convolutional layer of the standard Convolutional Neural Network (CNN) based image classification architecture [18] and object detection architectures [19] have been used as a feature maps. Binarized Normed Gradients (BING) [18] is also used as a feature by a few researchers. Region Of Interest (ROI) based algorithms of region proposal network are also used for feature extraction [20]. Recently, researchers have started using the latent space representation of the autoencoder as features [6]. Zhao et. al transform an image using wavelet transform and then extracts the features using deep autoencoders [2].

All the proposed deep learning-based approaches use the deep learning architecture as a black-box and are highly susceptible to adversarial attacks [7]. They lack interpretability and they may not be suitable in any critical applications. Moreover, the architectures that use autoencoders have a limited number of convolutional layers, due to which the corresponding latent space representation's receptive field is smaller than the size of the image. As a result, the latent space representation does not learn the complete content of the image.

### B. Similarity Score

There are two types of scoring, that are generally used. Distance based scoring and voting based scoring. The algorithms that use distance-based scoring widely make use of some sort of a normalized Euclidean distance as shown in (1).

$$D(I_q, I_d) = \sum_{i=1}^N (|q_i - d_i|^p)^{\frac{1}{p}} \quad (1)$$

where,  $I_q$  is the query image and  $I_d$  is the image in the database. We assume the feature vector to be of length  $N$  and  $q_i, d_i$  are the corresponding elements of the feature vectors of the query and the database image respectively.  $p$  is the normalization factor. L-1 norm (with  $p=1$ ) as a

distance-based similarity metric has been used by the researchers [9]. However, it is generally claimed that the similarity measure by L-P distance is not optimal because using it can sometime lead to few images violating the  $k$  nearest neighborhood policy [21]. In order to mitigate this issue, [22] comes up with a probabilistic framework for similarity measure. Some researchers have even tried a learning-based score [23].

In voting-based methods, every element in the feature vector is considered as a vote and the similarity score is measured by the total number of matched feature points [24]. Jegou et. al [25] propose a scoring function as a summation of squared Term Frequency and Inverse Document Frequency (TF-IDF) weights on shared visual words. Authors in [26] made a slight modification and changed the scoring operation of TF-IDF weights into mod operation. Although the voting-based techniques seem to work well, it is indeed some sort of threshold on the distance-based techniques.

## III. CONTRIBUTIONS OF THE PAPER

The main contribution of the paper is an efficient algorithm for content-based image retrieval. Towards this, we make the following contributions.

1) We propose an ensemble-based architecture for feature extraction of images. The proposed architecture ensembles the following:

- Classical handcrafted texture features
- Latent space representation of the learnt deep convolutional autoencoder
- Compressed version of the latent space representation by passing it through the standard JPEG pipeline

2) We propose evidence-based combination algorithm to come up with the similarity scores.

- The Normalized Mutual Information (NMI), Mean Squared Error (MSE), and L-2 norm between the features of the query image and the image in the database act as the evidence for DSCR (Dempster Shafer Combination Rule).
- We consider the number of feature matches as its corresponding confidences.

3) We demonstrate the results of the proposed algorithm on the standard ukBench dataset using various quantitative analysis and show the improvement from with the other SOTA (State of The Art) algorithms.

## IV. PROPOSED SYSTEM FOR CONTENT BASED IMAGE RETRIEVAL

The proposed system for content-based image retrieval is divided into three stages. In the first stage, we train the

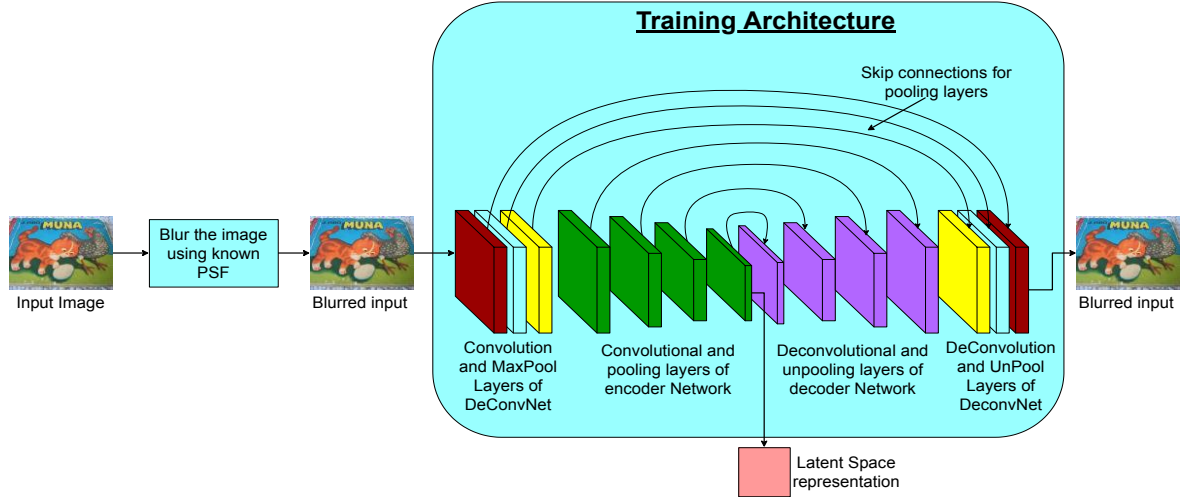


Fig. 1. Proposed architecture for training the network

proposed fully convolutional autoencoder. This gives us the encoding architecture to generate the latent spaces for each of the images in the database. In second stage, we generate the feature set for our database and in the third stage, we compute similarity and retrieve the most relevant images. Each of the stages are explained below.

**A. Fully Convolutional Autoencoder**

The proposed architecture for training is shown in Fig. 1. The latent space representation of a given image can be obtained by training the proposed fully convolutional autoencoder. The input image is initially blurred using standard gaussian blurring with 5x5 kernel, and this blurred image is used for training. Blurring reduces sharp edges and corners of the image and helps the initial layers of the neural network to learn faster. The autoencoder is kept fully convolutional so that the input of any resolution can be trained.

The input image is passed through an encoder-decoder kind of a network. The encoder network consists of the convolutional and pooling layers of DeConvNet (our backbone architecture). Along with those layers we add four additional convolutional and pooling layers. ReLU activation function is used in the proposed architecture. The backbone architecture is pre trained on the imagenet dataset and they serve as the weight initialization for all the layers. The addition of four layers help the model learn data specific high level features.

The decoder network is exactly the reverse of the encoder network. It consists of four deconvolutional and unpooling layers. We add skip connections for every maxpool layer to achieve better learnability. i.e., we propose to maintain the switch variables that identify the location of the maximum value during encoding (pooling) and the gradient is passed back to the same location

during unpooling. The latent space representations learnt in this level are used as one of the features.

**B. Feature Extraction**

The architecture to extract the features for all the images in the database is as shown in Fig. 2. The encoder part of the learnt autoencoder is used in this stage. The input image is blurred using a known Point Spread Function (PSF) and passed through the backbone architecture. Later it is passed through the four convolutional and pooling layers to generate the latent space representation. This serves as one of the features. We then propose to compress the latent space representation using the Discrete Cosine Transform (DCT) algorithm because we claim that the correlation and frequency properties of the input images are retained in the latent space. The reasoning of this claim is as follows. The input image has very high correlation because it is blurred and the proposed architecture contains only convolutional and pooling layers. Both, convolutional and pooling layers are spatial layers, and are applied patch wise and therefore, they do not reduce the correlation and frequency properties of the input image by significant amount. As the number of layers in the network is limited, we can say that the correlation and the frequency properties of the input images are retained in the latent space.

The non-correlated data is highly preferred as it contains less number of bits and covers all the important features. This data has no image structure related information and therefore, we prefer to keep both the compressed latent space and the original latent space in the proposed algorithm. Taking decision only based on deep learning-based features is not preferred because of the adversarial attacks. To avoid this, we propose to extract various texture features of the image, namely: mean, median, standard deviation, energy, entropy, third mom

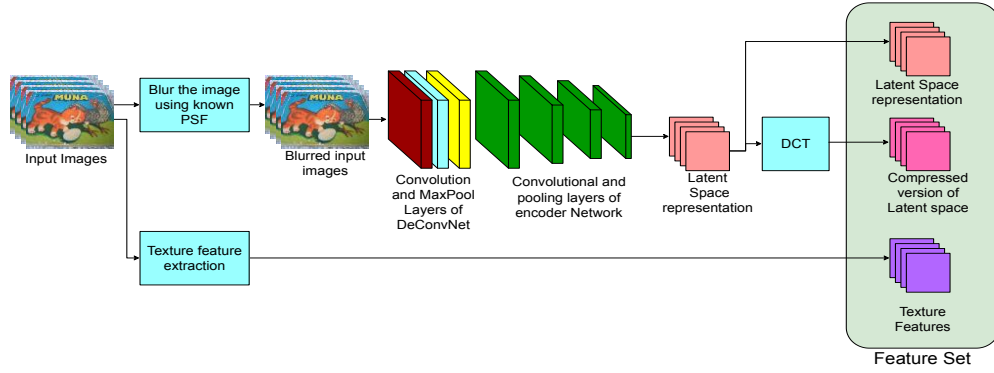


Fig. 2. Proposed architecture for feature extraction of all the images

ent and histogram of the image. All these contribute to the final feature set. Thus, the final feature set contains

- Latent space representation of the input image
- Compressed version of the latent space representation
- Texture features

### C. Similarity Scoring and Image Retrieval

The next stage of the architecture is to check the similarity between the feature set of the images and score them towards image retrieval. The proposed architecture is as shown in Fig. 3. Query image undergoes blurring, similar to the input image. It then passes through the same pipeline as discussed in Section IV-B to obtain the same feature set. We propose to compute similarity score in the following way.

1) *NMI and MSE between latent space representations:* The latent space representation contains the correlation information hence, we compute Normalized Mutual Information (NMI) and Mean Squared Error (MSE) between the two latent spaces. The NMI between the two latent spaces  $I_1, I_2$  is computed by Eq. (2)

$$NMI(I_1, I_2) = \frac{2 \times MI(I_1, I_2)}{H(I_1) + H(I_2)} \quad (2)$$

Where  $H(I)$  is the entropy of Image  $I$  and  $MI(I_1, I_2)$  represents the mutual information and is given by:

$$MI(I_1, I_2) = H(I_1) - H(I_1|I_2)$$

The MSE between the two latent spaces  $I_1, I_2$  is computed by Eq. (3)

$$MSE(I_1, I_2) = \frac{\left( \sum_{i=1}^m \sum_{j=1}^n \sum_{k=1}^p |I_{1(i,j,k)} - I_{2(i,j,k)}|^2 \right)^{\frac{1}{2}}}{m \times n \times p} \quad (3)$$

where,  $m$  and  $n$  are the dimensions of the image and  $p$  is the corresponding channel depth.

2) *L-2 norm between other parameters:* The compressed version of the latent space representation and the texture features do not have any structural similarity. We calculate L-2 norm between them using Eq. (4) as below.

$$D(I_1, I_2) = \left( \sum_{i=1}^N |q_i - d_i|^2 \right)^{\frac{1}{2}} \quad (4)$$

where, we assume that there are  $N$  elements in each of the features.

3) *Fusion of various similarity scores:* We now fuse the different similarity scores using the technique of weighted fusion. The weights for each of the features is selected using the number of votes they get i.e. percentage of elements that match with each other in query and database image. The fused value is used as the final similarity score and is used to extract the retrieved images from the database.

## V. IMPLEMENTATION DETAILS

We train our model for 350 epochs on the ukBench dataset and fine-tune on the same training dataset for another 350 epochs. The fine-tuning is divided into two steps, namely warm-up and final training. A batch size of 1 was chosen due to the inability of our GPU to load multiple high resolution, multi-resolution images in a batch. To train the architecture on ukBench dataset, we choose a learning rate of  $1e^{-5}$ , Adam optimizer with momentum of 0.8, weight decay of  $1e^{-4}$ , and gamma value of 0.1. We fine-tune the same architecture using a learning rate of  $1e^{-6}$ , weight decay as 0.0005 and momentum of 0.8. While finetuning, we only train the added 4 new convolutional and pooling layers, keeping the weights of DeconvNet backbone frozen. All computations are carried out on High Performance Computing Cluster having 32 GB V100 GPUs. The training procedure takes an average 4 sec (approx.) per iteration with a

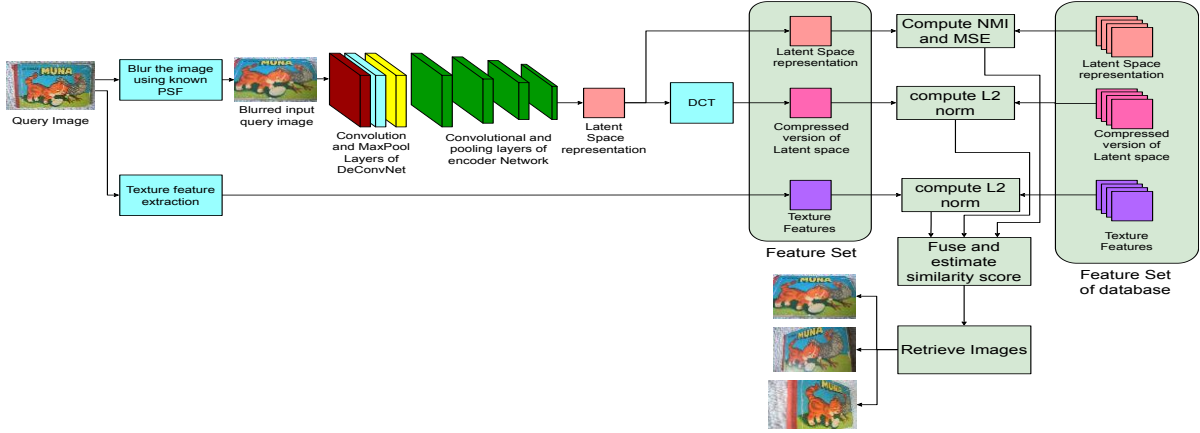


Fig. 3. Proposed architecture for image retrieval

GPU memory occupancy of 31GB (approx). We use fusion of quantized cross entropy loss, Mean Squared Error (MSE) loss and the Intersection Over Union (IOU) loss for final training and Mean Average Precision (MAP) loss for the warm-up-training.

## VI. RESULTS AND DISCUSSIONS

We demonstrate the results using the standard ukBench dataset, which has 10200 images in sets of 4 images that are very similar to each other. The results of the proposed algorithm are evaluated using two quantitative methods, namely accuracy and PR curve.

1) *Accuracy*: If an image  $I_1$  is fed as input to the system, we expect the output to be  $I_2$  or  $I_3$  or  $I_4$ . If one amongst the three is given as output, then we call it a positive retrieval else, it would be a negative retrieval. Therefore, accuracy is given by Eq. (5).

$$Accuracy = \frac{\Sigma Pos\ retrieval}{\Sigma Neg\ retrieval + \Sigma Pos\ retrieval} \quad (5)$$

2) *PR curve*: PR curve stands for Precision Recall Curve. To estimate the precision and recall, we test the algorithm in a loop.  $I_1$  is fed as input and we run the algorithm in a loop as long as  $I_2$ ,  $I_3$  and  $I_4$  are all retrieved, or maximum number of iterations is reached. Now, the number of detections, done so far that are not from the set  $\{I_2, I_3 \text{ and } I_4\}$  constitutes False Positive (FP). True Positive (TP) is the number of correct images detected ( $< 3$ , if the execution stops at the maximum number of iterations). False Negative (FN) is the number of images that are not detected amongst  $I_2, I_3$  and  $I_4$ . The values of Precision and Recall are calculated using the Eqs. (6).

$$Precision = \frac{TP}{TP + FP} \quad Recall = \frac{TP}{TP + FN} \quad (6)$$

We compute the values of Precision and Recall at different values of maximum number of iterations and plot the PR curve, with precision on y axis and recall on x axis. Ideally a system must have a straight line parallel to x axis at unit 1. This means, we are able to achieve 100% recall for any value of precision.

### A. Visualization of the Results

The Fig. 4 shows the visualization of the trained auto-encoder for some of the images of ukBench dataset. Here, (a) shows the input image (un-blurred), (b) shows the learnt latent space and (c) shows the corresponding decoder output. The reconstruction of the images using the proposed autoencoder is shown in Fig. 4.

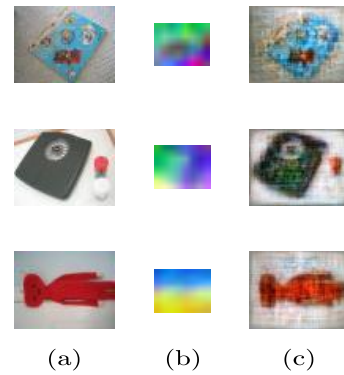


Fig. 4. Visualization of the output of the auto-encoder on some image

### B. Results on the ukBench Dataset

The accuracy of the proposed algorithm is shown in Table I. It also shows the comparative analysis with respect to the other state of the art techniques. The corresponding PR curve for the same is as shown in Fig. 5. Thus, we

observe an improvement of 3.2% from the best performing state of the art architecture.

TABLE I  
COMPARATIVE ANALYSIS OF THE ACCURACY ON THE UKBENCH DATASET

Method	Accuracy
VS CSIR [27]	89.53%
ALO CBIR [28]	91.25%
NC CBIR [29]	89.5%
DIR CBIR [30]	93.5%
Proposed Algorithm	96.7%

### VII. ABLATION STUDIES

To prove the need of every component used in the proposed architecture, we ablate the architecture by keeping only one component at a time and evaluate its performance. The results of the ablation study are shown in Table II and Fig. 5.

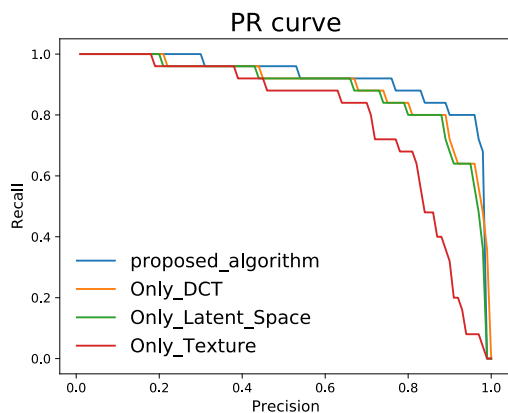


Fig. 6. PR curve for the proposed algorithm on the ukBench dataset and corresponding ablation studies.

Here, “Only\_DCT” refers to the ablated architecture where DCT based compressed version of the latent space is the sole contributor of the feature map. Similarly, “Only Latent space” and “Only Texture” are the architectures where latent space and texture features are the sole contributors for the feature maps respectively. Also, Table II provides the information on the time taken to fetch one image from the dataset (Tq). The corresponding PR curve for the same is as shown in Fig. 5. From the time analysis, it is evident that if we use only the compressed version of the latent space for comparison, we obtain fairly good results in a short span of time.

#### A. Effect of Blurring

To prove the need for blurring the input before it is fed

TABLE II  
ABLATION ANALYSIS OF THE ACCURACY ON UKBENCH DATASET. HERE TQ STANDS FOR THE TIME TAKEN TO QUERY ONE IMAGE

Method	Accuracy	Tq
Only DCT	92.3%	3.8 sec
Only Texture	76.7%	1.2 sec
Only Latent Space	92.0%	8.5 sec
Proposed Algorithm	96.7%	9.0 sec

to the autoencoder, we design a simple MSE based image retrieval algorithm as provided in [33]. We do an ablation study, of comparing the results obtained, with blurring and without blurring. The time taken to train the auto-encoder and corresponding accuracy are given in Table III.

TABLE III  
ABLATION TO SHOW THE NEED OF BLURRING ON UKBENCH DATASET. HERE TT IS THE TIME TAKEN TO TRAIN THE AUTOENCODER

Method	Accuracy	Tt
With Blur	81.8%	8.4 hours
Without Blur	76.9%	8.38 hours

As seen in the results, the addition of blur, has not changed the train time of the algorithm, but it has increased the accuracy of the image retrieval system. This is because, the addition of blur in the training dataset, reduces the edge information of the training image. Thus, the deep learning network is forced to learn the structure of the object in the image rather than learning the image properties. This makes the system learn more generalized latent spaces rather than learning the image specific latent space, which helps us to get a better image retrieval.

### VII. CONCLUSION

In this paper we propose a novel learning based ensemble algorithm for efficient feature extraction. The classical texture features, parameters learnt by the latent space representation of the deep autoencoder and its corresponding compressed parameters generated using the standard DCT technique are ensemble in the proposed algorithm. We fuse similarity distance and Euclidean distance between the extracted ensemble feature of the query image and the images in the database to retrieve relevant images. We demonstrate the efficiency of the proposed algorithm on the standard ukBench dataset using different quantitative parameters. We observe that the proposed algorithm is 96.7% accurate, which is 3.2% better than the best performing state-of-the-art algorithms.

## REFERENCES

- [1] Akhtar, N., & Mian, A. (2018). Threat of adversarial attacks on deep learning in computer vision: A survey. *IEEE Access*, 6, 14410-14430.
- [2] Alexe, B., Deselaers, T., & Ferrari, V. (2012). Measuring the objectness of image windows. *IEEE Transactions on Pattern Analysis and Machine Intelligence*, 34(11), 2189-2202.
- [3] Babenko, A., Slesarev, A., Chigorin, A., & Lempitsky, V. (2014, September). Neural codes for image retrieval. In *European Conference on Computer Vision* (pp. 584-599). Springer, Cham.
- [4] Cao, Y., Wang, C., Zhang, L., & Zhang, L. (2011, June). Edgel index for large-scale sketch-based image search. In *CVPR 2011* (pp. 761-768). IEEE.
- [5] Cheng, M. M., Zhang, Z., Lin, W. Y., & Torr, P. (2014). BING: Binarized normed gradients for objectness estimation at 300fps. In *Proceedings of the IEEE Conference on Computer Vision and Pattern Recognition* (pp. 3286-3293).
- [6] Donoser, M., & Bischof, H. (2013). Diffusion processes for retrieval revisited. In *Proceedings of the IEEE Conference on Computer Vision and Pattern Recognition* (pp. 1320-1327).
- [7] Gordo, A., Almazán, J., Revaud, J., & Larlus, D. (2016, October). Deep image retrieval: Learning global representations for image search. In *European Conference on Computer Vision* (pp. 241-257). Springer, Cham.
- [8] Jégou, H., Douze, M., & Schmid, C. (2010). Improving bag-of-features for large scale image search. *International Journal of Computer Vision*, 87(3), 316-336.
- [9] Jegou, H., Schmid, C., Harzallah, H., & Verbeek, J. (2008). Accurate image search using the contextual dissimilarity measure. *IEEE Transactions on Pattern Analysis and Machine Intelligence*, 32(1), 2-11.
- [10] Krizhevsky, A., & Hinton, G. E. (2011, April). Using very deep autoencoders for content-based image retrieval. In *ESANN* (Vol.1, p.2).
- [11] Lin, Z., Ding, G., Hu, M., & Wang, J. (2015). Semantics-preserving hashing for cross-view retrieval. In *Proceedings of the IEEE Conference on Computer Vision and Pattern Recognition* (pp. 3864-3872).
- [12] Lowe, D. G. (2004). Distinctive image features from scale-invariant keypoints. *International Journal of Computer Vision*, 60(2), 91-110.
- [13] Matas, J., Chum, O., Urban, M., & Pajdla, T. (2004). Robust wide-baseline stereo from maximally stable extremal regions. *Image and Vision Computing*, 22(10), 761-767.
- [14] Mikolajczyk, K., & Schmid, C. (2004). Scale & affine invariant interest point detectors. *International Journal of Computer Vision*, 60(1), 63-86.
- [15] Qin, D., Wengert, C., & Van Gool, L. (2013). Query adaptive similarity for large scale object retrieval. In *Proceedings of the IEEE Conference on Computer Vision and Pattern Recognition* (pp. 1610-1617).
- [16] Ren, S., He, K., Girshick, R., & Sun, J. (2015). Faster r-cnn: Towards real-time object detection with region proposal networks. *Advances in Neural Information Processing Systems*, 28.
- [17] Rosten, E., Porter, R., & Drummond, T. (2008). Faster and better: A machine learning approach to corner detection. *IEEE Transactions on Pattern Analysis and Machine Intelligence*, 32(1), 105-119s
- [18] Rui, Y., Huang, T. S., Ortega, M., & Mehrotra, S. (1998). Relevance feedback: A power tool for interactive content-based image retrieval. *IEEE Transactions on Circuits and Systems for Video Technology*, 8(5), 644-655.
- [19] Rupapara, V., Narra, M., Gonda, N. K., Thipparthy, K., & Gandhi, S. (2020, June). Auto-encoders for content-based image retrieval with its implementation using handwritten dataset. In *2020 5th International Conference on Communication and Electronics Systems (ICCES)* (pp. 289-294). IEEE.
- [20] Siagian, C., & Itti, L. (2007). Rapid biologically-inspired scene classification using features shared with visual attention. *IEEE Transactions on Pattern Analysis and Machine Intelligence*, 29(2), 300-312.
- [21] Siradjuddin, I. A., Wardana, W. A., & Sophan, M. K. (2019, October). Feature extraction using self-supervised convolutional autoencoder for content based image retrieval. In *2019 3rd International Conference on Informatics and Computational Sciences (ICICoS)* (pp. 1-5). IEEE.
- [22] Smeulders, A. W., Worring, M., Santini, S., Gupta, A., & Jain, R. (2000). Content-based image retrieval at the end of the early years. *IEEE Transactions on Pattern Analysis and Machine Intelligence*, 22(12), 1349-1380.
- [23] Wang, X. Y., Zhang, B. B., & Yang, H. Y. (2014). Content-based image retrieval by integrating color and texture features. *Multimedia Tools and Applications*, 68(3), 545-569.
- [24] Wu, Y., Liu, H., Yuan, J., & Zhang, Q. (2018). Is visual saliency useful for content-based image retrieval? *Multimedia Tools and Applications*, 77(11), 13983-14006.
- [25] Wu, Z., Ke, Q., Isard, M., & Sun, J. (2009, June). Bundling features for large scale partial-duplicate web image search. In *2009 IEEE Conference on Computer Vision and Pattern Recognition* (pp. 25-32). IEEE.
- [26] Xie, H., Gao, K., Zhang, Y., Tang, S., Li, J., & Liu, Y. (2011). Efficient feature detection and effective post-verification for large scale near-duplicate image search. *IEEE Transactions on Multimedia*, 13(6), 1319-1332.
- [27] Xie, L., Hong, R., Zhang, B., & Tian, Q. (2015, June). Image classification and retrieval are one. In *Proceedings of the 5th ACM on International Conference on Multimedia Retrieval* (pp. 3-10).
- [28] Babenko, A., & Lempitsky, V. (2015). Aggregating local deep features for image retrieval. In *Proceedings of the IEEE International Conference on Computer Vision* (pp. 1269-1277).
- [29] Zhao, X., & Nutter, B. (2016, March). Content Based Image Retrieval system using Wavelet Transformation and multiple input multiple task Deep Autoencoder. In *2016 IEEE Southwest Symposium on Image Analysis and Interpretation (SSIAI)* (pp. 97-100). IEEE.
- [30] Zhou, W., Li, H., Lu, Y., & Tian, Q. (2011, November). Large scale image search with geometric coding. In *Proceedings of the 19th ACM international conference on Multimedia* (pp. 1349-1352).
- [31] Raju Dhanakshirur, R., Ashok Tabib, R., Patil, U., & Mudanagudi, U. (2019). Evidence based feature selection and collaborative representation towards learning based PSF estimation for motion deblurring. In *Proceedings of the IEEE/CVF International Conference on Computer Vision Workshops* (pp. 0-0).
- [32] Dhanakshirur, R. R., Pillai, P., Tabib, R. A., Patil, U., & Mudanagudi, U. (2018, September). A framework for lane

prediction on unstructured roads. In *International Symposium on Signal Processing and Intelligent Recognition Systems* (pp. 178-189). Springer, Singapore.

[33] Zhou, W., Li, H., & Tian, Q. (2017). Recent advance in content-based image retrieval: A literature survey. *arXiv preprint arXiv:1706.06064*.

# Separation Axioms of the Space of Endless Causal Curves

Gunjan Agrawal\* and Shruti Sinha

Department of Mathematics,  
Dayalbagh Educational Institute, Agra, 282005, India

*There are two significant topologies on the collection of causal curves in spacetime – one is the Geroch topology and the other one is the topology defined by Low which is the same as the Geroch topology when the spacetime is equipped with the manifold topology. In the present paper, studying the separation axioms of the space of causal curves with respect to the latter topology when the spacetime is equipped with the path topology, it is obtained that it is non- $T_1$ , non-Hausdorff, non-regular, non-completely regular, and non-normal. However, its subspace consisting of endless causal curves is  $T_1$ , non-regular, non-completely regular, and non-normal, after imposing some causality conditions on the underlying spacetime.*

**Keywords** – Causal curve, Endless causal curve, Spacetime, Separation axioms, Lorentz manifold, Global hyperbolicity, Strong causality, Minkowski space

## I. INTRODUCTION

Spacetime, a continuum of space and time, admits a causal structure to explain cause-effect relationship among its elements. Spacetime in both classical physics and in the theory of relativity has been perceived as four dimensional: one dimension for time and the remaining three are spatial dimensions. However, the causal structure differs significantly in both of the physical theories. In classical physics, time is considered absolute, irrespective of frame of reference, and the spacetime has been mathematically modeled as the three-dimensional Euclidean space at different times. All the events in space at a fixed time are termed as simultaneous, and causally related events are mathematically described as those which can be joined by a parameterized curve in space which is required to move forward in time. However, in the special theory of relativity, the concept of absolute time had been replaced by the assumption that nothing moves faster than light. Hence, for an inertial observer (sometimes referred to as an inertial frame of reference), simultaneous events are defined using synchronization of clocks positioned at each point in a three-dimensional coordinate space constructed with respect to the observer positioned at the origin [18]. Mathematical framework for spacetime in special theory of relativity is the four-dimensional Minkowski space [20]. Physically significant non-Euclidean topologies, viz., fine topology, space topology, time topology,  $t$  and,  $s$ -topologies, as proposed by Zeeman on a Minkowski space are well studied [1]-[3],

[19], [20]. General relativity treats gravity not as a force field but a built-in feature of spacetime. A four-dimensional Lorentz manifold which is connected, Hausdorff, paracompact and smooth, serves as a mathematical model for spacetime in the theory of general relativity [8]. Path topology, introduced by Hawking on a strongly causal Lorentz manifold, is a non-manifold topology which is strictly finer than manifold topology and induces Euclidean topology on every timelike curve. Also, its homeomorphism group is consistent with the causal and conformal structure of the manifold [8].

Causal structure of spacetime provides useful insight into its geometry and underlying topological structure [13], [19]. It defines notions, known as causal conditions, on spacetime which are essential ingredients in Penrose singularity theorems [16]. Physicists describe singularity as a region in spacetime where physical laws tend to fail [7]. Singularities are broadly classified as (i) curvature singularity, and (ii) the singularity mathematically modeled in terms of incomplete timelike geodesics [15]. The latter one is studied by Penrose, Hawking, Geroch, to quote a few [4], [7], [17]. Penrose singularity theorems provide sufficient conditions for spacetime to be timelike or null geodesically incomplete [7]. The upper semi-continuity of the length function defined on the space of causal curves is used in Penrose singularity theorems [16]. Further, causality conditions enable to study the topological structure of the space of causal geodesics defined on it [9]. In the present paper, a topological study of the space of endless causal curves, in a smooth  $n$ -dimensional Lorentz manifold equipped with the path topology, has been undertaken.

---

\*Corresponding author: [dei.gunjan@yahoo.com](mailto:dei.gunjan@yahoo.com)

ISSN 0972-5032 (P); Copyright ©2022, SSI

## II. STANDARD DEFINITIONS AND RESULTS

Throughout this paper,  $R, N$  and  $Q$  denote the set of real, natural and rational numbers, respectively. If  $A$  and  $B$  are two sets then the notation  $A \setminus B$  refers to set difference of  $A$  and  $B$ . We denote the complement of the set  $A$  by  $A^c$ . If  $X$  is a topological space and  $G \subseteq X$ , then the notation  $Cl(G)$  represents closure of the set  $G$  in  $X$ . For  $x \in R^n$ ,  $N_\varepsilon^E(x)$  denotes the Euclidean open ball at  $x$  of radius  $\varepsilon > 0$  and is given by the set  $\{y \in R^n: d_E(x, y) < \varepsilon\}$ , where  $d_E$  denotes the Euclidean metric. For  $n \in N$  and  $n > 1$ , the  $n$ -dimensional real vector space  $R^n$  equipped with the bilinear form,  $g: R^n \times R^n \rightarrow R$ , satisfying the following properties: (i) For all  $x, y \in R^n$ ,  $g(x, y) = g(y, x)$ , i.e. the bilinear form is symmetric, (ii) If for all  $y \in R^n$ ,  $g(x, y) = 0$  then  $x = 0$ , and (iii) there exists a basis  $\{e_0, e_1, \dots, e_{n-1}\}$  for  $R^n$  with

$$g(e_i, e_j) \equiv \eta_{ij} = \begin{cases} 1 & \text{if } i = j = 0 \\ -1 & \text{if } i = j = 1, 2, \dots, n-1 \\ 0 & \text{otherwise} \end{cases}$$

is called  $n$ -dimensional *Minkowski space* and is denoted by  $M$ . An element  $x \in M$  is represented as,  $x = \sum_{i=0}^{n-1} x_i e_i$ , where  $x_0$  represents *time coordinate* and  $x_1, x_2, \dots, x_{n-1}$ , the *spatial coordinates* of  $x$  relative to the canonical basis vectors  $e_1, e_2, \dots, e_{n-1}$ . If  $x, y \in M$  then  $g(x, y) = x_0 y_0 - \sum_{i=1}^{n-1} x_i y_i$ . An element  $x \in M$  is called *timelike (causal)*, according to  $g(x, x) > (\geq) 0$ . A *timelike (causal) curve* in  $M$  is a smooth curve such that tangent vector (also an element of  $M$ ) at every point is non-zero and timelike (causal). A quadratic form  $Q$ , on Minkowski space is defined by  $Q(x) := g(x, x)$ . The time cone at  $x$  is the set  $C^T(x) := \{y \in M: y = x \text{ or } Q(y - x) > 0\}$ . The group generated by all linear operators, leaving the quadratic form  $Q$  invariant, translations and dilatations (multiplication by a scalar) on  $M$  is called the *Lorentz group* [19].

A smooth  $n$ -dimensional *Lorentz manifold* denoted by  $L$  is an  $n$ -dimensional  $C^r$  ( $r \geq 2$ ) manifold, such that the *tangent space* at  $p \in L$ , denoted by  $T_p(L)$ , is equipped with a smooth Lorentz metric tensor  $h$  of the type  $(1, n-1)$ . A tangent vector  $X_p \in T_p(L)$  is said to be *timelike* if  $h(X_p, X_p) > 0$ , *causal* if  $h(X_p, X_p) \geq 0$ , and *space-like* if  $h(X_p, X_p) < 0$  [4]. Minkowski space  $M$  equipped with the bilinear form  $g$ , also known as Lorentz metric, is an example of Lorentz manifold wherein the tangent space at each  $x \in M$  is  $M$  itself.  $L$  is called *time orientable*, if it is equipped with a smooth non-vanishing vector field, say  $V$ . A timelike (causal) tangent vector  $X_p \in T_p(L)$  is called *future directed* if  $h(X_p, V(p)) > 0$ , where  $V(p)$  at  $p$  belongs to  $T_p(L)$ . A *past directed timelike vector* is defined analogously by reversing the sign of the above inequality [4].

A *path* in  $L$  is a continuous map,  $\gamma: \Sigma \rightarrow L$ , where  $\Sigma$  is a connected subset of  $R$  containing more than one point. Two paths are considered to be equivalent if one is a reparametrization of the other. A curve is an equivalence

class of smooth paths with non-vanishing derivatives [16]. A *timelike (causal) curve* in  $L$  is a curve such that the tangent vector at every point of the curve is timelike (causal). A *future directed timelike (causal) curve* is one such that the tangent vector to the curve at every point is future directed timelike (causal). Similarly, *past directed timelike (causal) curve* is defined by replacing future with the past. The *chronological future of  $x$  relative to  $L$*  is defined as:  $I^+(x) = \{y \in L: \text{there exists a future directed timelike curve from } x \text{ to } y\}$ . The *causal future  $J^+(x)$  of  $x$  relative to  $L$*  is defined to be the union of  $I^+(x)$  and  $\{x\}$ . Similarly, the *chronological past of  $x$  relative to  $L$* , denoted by  $I^-(x)$  and the *causal past  $J^-(x)$*  are defined by replacing future with past [8]. A causal curve  $\gamma$  has future end point  $q$  if for any open set  $G(q)$  containing  $q$ , there exists  $s \in R$  such that  $\gamma(t) \in G(q)$ , for all  $t \geq s$ . Similarly,  $\gamma$  has past end point  $r$  if for any open set  $G(r)$  containing  $r$ , there exists  $v \in R$  such that  $\gamma(t) \in G(r)$ , for all  $t \leq v$ . A causal curve without any end points is called endless [16].

An *achronal set*, say  $K$ , is a subset of  $L$  such that if  $x, y \in K$ , then there does not exist any timelike curve joining  $x$  and  $y$  [6], [8]. A *Cauchy surface* is an achronal set in  $L$  such that it intersects every endless timelike curve exactly once. A spacetime is said to be *globally hyperbolic* if it contains a Cauchy hypersurface. There are several equivalent definitions for defining a globally hyperbolic spacetime [16].

A *causality neighborhood* of  $x \in L$  is an open set  $D$  (in manifold topology) such that  $\gamma^{-1}(D)$  is a connected subset of  $F$ , for any causal curve  $\gamma$ . If  $x$  has a neighbourhood basis consisting of causality neighborhoods,  $L$  is said to be *strongly causal* at  $x$ . A manifold  $L$  is said to be *strongly causal* if it is strongly causal at each of its points [8]. Let  $K(p, U) := (I^+(p) \cup I^-(p) \cup \{p\}) \cap U$ , where  $U$  is an open set at  $p$  diffeomorphic to a star shaped open set at the origin in the tangent space at  $p$ . The set  $U$  is also known as *open convex normal neighborhood* of  $p$ . Then  $V := \{K(p, U): p \in L\}$  forms a basis. The topology generated by  $V$ , is known as path topology on  $L$ :  $L$  together with the path topology is denoted by  $L^p$  [8]. Path topology on a Lorentz manifold is the finest topology that induces Euclidean topology on every timelike curve. It is Hausdorff and connected [8]. Any causal curve containing a segment of null geodesics is not continuous in  $L^p$ , as path topology induces a discrete topology on null geodesics [11]. For the  $n$ -dimensional Minkowski space  $M$ , the set  $B := \{C^T(x) \cap N_\varepsilon^E(x): x \in M, \varepsilon > 0\}$  forms a basis for the path topology on  $M$  which coincides with the  $t$ -topology on  $M$ :  $M$  with  $t$ -topology is denoted by  $M^t$  [1]. Throughout this paper, *spacetime*, denoted by  $L$ , refers to a connected, Hausdorff, paracompact, smooth  $n$ -dimensional Lorentz manifold equipped with a smooth non-vanishing vector field, unless otherwise specified. For terms not explained here, we refer to [7], [8], [14], [16], and [18].

### III. SPACE OF CAUSAL CURVES

A causal curve in spacetime provides information about its causal structure and is an important element in the study of spacetime singularities [9], [10], [16]. Physically admissible spacetimes, also known as causal spacetimes, are the ones that do not contain any closed causal curve [7]. In a spacetime, any two events are said to be causally related, if there exists a causal curve in the spacetime joining them. This generates a partial order relation, also referred to as *causal structure*, on the spacetime [6]. The conformal transformation which alters the spacetime metric, preserves the causal structure of the spacetime; illustrating the fact that causal cone at any point in one frame of reference is mapped to the causal cone at the image of the point in another frame of reference [8].

The collection of causal curves, denoted by the symbol,  $C_L$  in  $L$ , has been topologized by Low [11] as follows: Let  $\gamma \in C_L$ ,  $x \in Im(\gamma)$  and  $U$  be an open set containing  $x$  in  $L$ , where  $Im(\gamma)$  represents image of the curve  $\gamma$  in  $L$ . Define  $B_U^\gamma := \{\gamma' \in C_L: Im(\gamma') \cap U \neq \emptyset\}$ . It is clear that  $\gamma \in B_U^\gamma$ . The collection  $\mathcal{B} := \{B_U^\gamma: \gamma \in C_L, x \in Im(\gamma)\}$ , forms a sub-basis for a topology on  $C_L$ . There is another significant topology on  $C_L$ , known as *Geroch topology* [16]. These topologies are equal [11]. The topology defined by Low can also be extended to the collection of causal curves in the spacetime with the path topology. This space is denoted by  $C_L^\rho$ . In this section, separation axioms of  $C_L^\rho$  have been studied.

*Proposition 3.1*  $C_L^\rho$  is not  $T_1$  and hence not Hausdorff.

*Proof:* Let  $p \in L$  and  $U$  be an open convex normal neighborhood of  $p$ . Then a causal curve  $\gamma_1: I \rightarrow U$ , where  $I = [0, 1]$  can be constructed which is injective on  $I$ . Clearly,  $\gamma_1 \in C_L$ . Define  $\gamma_2 := \gamma_1|_{[0, 1/2]}$ . Then  $\gamma_2 \in C_L$ . It is evident that  $\gamma_1 \neq \gamma_2$  and  $Im(\gamma_2) \subseteq Im(\gamma_1)$ . Let  $G$  be an open set in  $C_L^\rho$ , such that  $\gamma_2 \in G$ . Then there exists a basis element  $H := \bigcap_{j=1}^n B_{U_j}^{\alpha_j}$ , where  $\alpha_j \in C_L$ ,  $U_j$  is an open set of  $x_j \in Im(\alpha_j)$ , for all  $j = 1, 2, \dots, n$ ; such that  $\gamma_2 \in H \subseteq G$ . Then  $Im(\gamma_2) \cap U_j \neq \emptyset$ , for all  $j = 1, 2, \dots, n$ . This implies that  $Im(\gamma_1) \cap Im(U_j) \neq \emptyset$ , for all  $j = 1, 2, \dots, n$ . Therefore,  $\gamma_1 \in H$  and the result follows.

*Remark 3.1* As is clear from the proof of Proposition 3.1, for arbitrary pair of causal curves, there may not exist nonempty open sets separating them in the sense of  $T_1$ . However, if  $\gamma_1$  and  $\gamma_2$  are two distinct causal curves containing their respective endpoints, such that their images are not contained in one another then, they can be separated by open sets: Consider two points  $x_1 \in Im(\gamma_1)$  and  $x_2 \in Im(\gamma_2)$ , such that  $x_1 \notin Cl(Im(\gamma_2))$  and vice-versa. Choose two disjoint open sets  $U$  and  $V$  in  $L^\rho$  containing  $x_1$  and  $x_2$ , respectively, as  $L^\rho$  is Hausdorff. Then, the two nonempty open sets,  $H_1 := B_U^{\gamma_1}$  and  $H_2 := B_V^{\gamma_2}$  in  $C_L^\rho$ , separate the causal curves under consideration.

*Proposition 3.2*  $C_L^\rho$  is not regular and hence not completely regular.

*Proof:* Let  $\gamma_1$  and  $\gamma_2$  be the causal curves as defined in Proposition 3.1. Choose  $x \in Im(\gamma_1) \setminus Im(\gamma_2)$  and an open set  $G$  containing  $x$  in  $L^\rho$ , such that  $G \cap Im(\gamma_2) = \emptyset$ . Existence of  $G$  is supported by the fact that endpoints of  $\gamma_2$  are contained in  $Im(\gamma_2)$ . This implies that  $\gamma_2 \notin B_G^{\gamma_1}$ . Define,  $F := (B_G^{\gamma_1})^c$ ,  $F$  is closed in  $C_L^\rho$  and  $\gamma_1 \notin F$ . Let  $G_1$  and  $G_2$  be two open sets containing  $F$  and  $\gamma_1$ , respectively. Now,  $\gamma_2 \in F$ . This implies that  $\gamma_2 \in G_1$ . Applying similar arguments as used in Proposition 3.1, we obtain that  $\gamma_1 \in G_1$ , which implies that  $G_1 \cap G_2 \neq \emptyset$ . This proves the result.

*Proposition 3.3*  $C_L^\rho$  is not normal.

*Proof:* Let  $\gamma_1$  be the causal curve as defined in Proposition 3.1. Choose,  $0 \leq t_1 < t_2 < t_3 < t_4 \leq 1$ . Define,  $\alpha := \gamma_1|_{[t_1, t_2]}$  and  $\beta := \gamma_1|_{[t_3, t_4]}$ . Clearly,  $Im(\alpha) \cap Im(\beta) = \emptyset$ . Let  $F_1 := \{\gamma \in C_L: Im(\gamma) \subseteq Im(\alpha)\}$  and  $F_2 := \{\gamma \in C_L: Im(\gamma) \subseteq Im(\beta)\}$ . Since  $\alpha \in F_1$ ,  $\beta \in F_2$ ;  $F_1$  and  $F_2$  are nonempty. By the definitions of  $F_1$  and  $F_2$ , and the fact that  $Im(\alpha) \cap Im(\beta) = \emptyset$ , it is obtained that  $Im(\gamma) \cap Im(\gamma') = \emptyset$  for any  $\gamma \in F_1$  and  $\gamma' \in F_2$ . Therefore,  $F_1 \cap F_2 = \emptyset$ . We now claim that both  $F_1$  and  $F_2$  are closed. If  $\gamma \in F_1^c$  then there exists  $x \in Im(\gamma) \setminus Im(\alpha)$ . Since endpoints of  $\alpha$  are contained in its image (from the definition of  $\alpha$ ), we can select an open set  $G$  containing  $x$  such that  $G \cap Im(\alpha) = \emptyset$ . This implies that  $G \cap Im(\gamma') = \emptyset$ , for any  $\gamma' \in F_1$ , that is  $F_1 \cap B_G^\gamma = \emptyset$ . Hence,  $B_G^\gamma \subseteq F_1^c$ , implying that  $F_1^c$  is open. Similarly,  $F_2^c$  is open, hence the claim. To complete the proof, let  $G_1$  and  $G_2$  be two open sets in  $C_L^\rho$  containing  $F_1$  and  $F_2$ , respectively. Then  $\alpha \in G_1$  and  $\beta \in G_2$ . As  $Im(\alpha) \subseteq Im(\gamma_1)$  and  $Im(\beta) \subseteq Im(\gamma_1)$ , in view of Proposition 3.1, it is obtained that  $\gamma_1 \in G_1 \cap G_2$ , that is,  $G_1 \cap G_2 \neq \emptyset$ .

### IV. SPACE OF ENDLESS CAUSAL CURVES

The collection of endless causal curves in spacetime  $L^\rho$ , denoted by  $\zeta_L$ , is a subset of the collection of causal curves. The set  $\zeta_L$  together with the subspace topology induced from the topology on  $C_L^\rho$  described in Section III, is denoted by  $\zeta_L^\rho$ . The subspace  $\zeta_L^\rho$  may or may not possess the topological properties which have been denied in  $C_L^\rho$  in Section III. Here, separation axioms of the space  $\zeta_L^\rho$  have been explored.

*Lemma 4.1* Let  $L^\rho$  be strongly causal. If  $\alpha \in \zeta_L$  then  $Im(\alpha) \not\subseteq Im(\beta)$  for any  $\beta \in \zeta_L$ , where  $\alpha \neq \beta$ .

*Proof:* We prove the result by the method of contradiction. Let us assume that  $Im(\alpha) \subseteq Im(\beta)$ , for some  $\beta \in \zeta_L$ , where  $\alpha \neq \beta$ . Therefore, there exists  $p \in Im(\beta) \setminus Im(\alpha)$ . Because both the causal curves are endless, using reparametrization and keeping the orientation of both curves unchanged, domains of both  $\alpha$  and  $\beta$  can be changed

to  $R$ . Choose,  $t_0 \in R$ , such that  $\beta(t_0) = p$ .

Let  $P := \text{Im}(\alpha) \cap \beta((-\infty, t_0])$  and  $Q := \text{Im}(\alpha) \cap \beta([t_0, \infty))$ . Clearly,  $\text{Im}(\alpha) = P \cup Q$ , where  $P \cap Q = \emptyset$ . We first claim that either  $P$  or  $Q$  is empty. Now,  $\beta((t_0, \infty)) = \beta((-\infty, t_0])^c \cap \text{Im}(\beta)$ . If  $x \in \beta((t_0, \infty))$ , then there exists a causality neighborhood  $E$  containing  $x$ , such that  $\beta^{-1}(E) \subseteq (t_0, \infty)$ , i.e.,  $\beta((t_0, \infty))$  is open in  $\text{Im}(\beta)$ . Hence  $\beta((-\infty, t_0])$  is closed in  $\text{Im}(\beta)$  and hence in  $\text{Im}(\alpha)$ . As  $\alpha$  is endless,  $\text{Im}(\alpha)$  is closed in  $L^\rho$ . Being a finite intersection of closed sets,  $P$  is closed in  $\text{Im}(\alpha)$ . Similarly,  $Q$  is closed in  $\text{Im}(\alpha)$ . This proves our claim, as  $\text{Im}(\alpha)$  is connected.

Without loss of generality, let us assume that  $\text{Im}(\alpha) \cap \beta((-\infty, t_0]) = \emptyset$ . Define  $r := \inf\{t > t_0 : \beta(t) \in \text{Im}(\alpha)\}$ . Since  $\beta(t_0) \notin \text{Im}(\alpha)$ ,  $r > t_0$ . Let  $z = \beta(r)$ . It is important to note that for every  $t > r$ , there exists  $\varepsilon > 0$ , such that  $r < r + \varepsilon < t$  and  $\beta(r + \varepsilon) \in \text{Im}(\alpha)$ , for otherwise, either  $r$  will not be an *infimum* or  $\alpha^{-1}(D_z)$  will be a singleton, where  $D_z$  is a causality neighborhood containing  $z$ . Let  $G$  be an open set containing  $z$ . Since  $L^\rho$  is strongly causal, there exists a causality neighborhood  $D_z$  containing  $z$ , such that  $D_z \subseteq G$  and  $\beta^{-1}(D_z)$ ,  $\alpha^{-1}(D_z)$  are nonempty, connected, and open in  $R$ . Let  $\beta^{-1}(D_z) = (b_1, b_2)$ . Since  $z \in D_z$ ,  $b_1 < r < b_2$ . Define  $A := \alpha^{-1}(D_z)$ . We assert that  $A$  is unbounded. To the contrary, let us suppose that  $A = (c_1, c_2)$ ;  $c_1, c_2 \in R$ . From the definition of  $r$ , a sequence  $(t_n)_{n \in \mathbb{N}}$ ;  $t_i \neq t_j$  for  $i \neq j$  can be constructed, where  $r < t_n \in (b_1, b_2)$  and  $\beta(t_n) \in \text{Im}(\alpha) \cap D_z$ , such that  $(t_n)_{n \in \mathbb{N}}$  converges to  $r$ . Then  $\beta(t_n)_{n \in \mathbb{N}}$  will converge to  $z$ . Now, construct a sequence  $(u_n)_{n \in \mathbb{N}}$ ;  $u_n \in A$ , such that  $\alpha(u_n) = \beta(t_n)$ . Then there exists a subsequence  $(u_{n_k})_{k \in \mathbb{N}}$  of  $(u_n)_{n \in \mathbb{N}}$  converging to  $v$  in  $Cl(A)$ . This implies that  $\alpha(u_{n_k})$  converges to  $\alpha(v)$ . But  $\alpha(u_{n_k}) \in \beta(t_n)_{n \in \mathbb{N}}$ , therefore  $\alpha(v) = z$ . As  $\alpha(A) \subseteq \beta([r, b_2])$ , choose  $\varepsilon_1, \varepsilon_2 > 0$  and  $r_1, r_2 \in (r, b_2)$ , such that  $\beta(r_1) = \alpha(v - \varepsilon_1)$  and  $\beta(r_2) = \alpha(v + \varepsilon_2)$ , where  $v - \varepsilon_1, v + \varepsilon_2 \in (c_1, c_2)$ . Without loss of generality, let us assume that  $r_1 < r_2$ . Now,  $\alpha([v, v + \varepsilon_2])$  is connected assuming values  $\alpha(v) = \beta(r)$  and  $\alpha(v + \varepsilon_2) = \beta(r_2)$ . We assert that there exists  $v' \in (v, v + \varepsilon_2)$ , such that  $\alpha(v') = \beta(r_1)$ . To the contrary, let us suppose that  $\beta(r_1) \notin \alpha([v, v + \varepsilon_2])$ . Define  $F_1 := \alpha([v, v + \varepsilon_2]) \cap \beta((r, r_1))$  and  $F_2 := \alpha([v, v + \varepsilon_2]) \cap \beta((r_1, b_2))$ . Clearly,  $F_1 \cap F_2 = \emptyset$ . Let  $W := \alpha([v, v + \varepsilon_2])$ . Now,  $\beta((r, r_1))$  and  $\beta((r_1, b_2))$  are open in  $\text{Im}(\beta)$  [proof is similar as stated above for  $\beta((t_0, \infty))$ ]. Hence,  $F_1$  and  $F_2$  are open in  $W$ . This is a contradiction since  $W$  is connected. Thus,  $\beta(r_1) \in \alpha([v - \varepsilon_1, v]) \cap \alpha([v, v + \varepsilon_2])$ , that is,  $\alpha([v - \varepsilon_1, v]) \cap \alpha([v, v + \varepsilon_2]) \neq \emptyset$ , which is a contradiction, as  $L^\rho$  is strongly causal and hence  $\alpha$  is injective. Therefore,  $\alpha^{-1}(G)$  is unbounded. This implies that  $z$  is an endpoint of the curve  $\alpha$ , giving a contradiction to the fact that  $\alpha \in \zeta_L$ . This completes the proof.

**Proposition 4.1** Let  $L^\rho$  be strongly causal. Then  $\zeta_L^\rho$  is  $T_1$ .

*Proof:* Let  $\gamma_1, \gamma_2 \in \zeta_L^\rho$ , where  $\gamma_1 \neq \gamma_2$ . Then, there exist

$x_1 \in \text{Im}(\gamma_1) \setminus \text{Im}(\gamma_2)$  and  $x_2 \in \text{Im}(\gamma_2) \setminus \text{Im}(\gamma_1)$  from Lemma

4.1. Also, neither  $x_1$  nor  $x_2$  is an endpoint of  $\gamma_1$  and  $\gamma_2$ , as both the curves are endless. Therefore, there exist two disjoint open sets  $N(x_1)$  and  $N(x_2)$  containing  $x_1$  and  $x_2$ , such that  $N(x_1) \cap \text{Im}(\gamma_2) = \emptyset$  and  $N(x_2) \cap \text{Im}(\gamma_1) = \emptyset$ . Define  $G_1 := B_{N(x_1)}^{\gamma_1}$ , and  $G_2 := B_{N(x_2)}^{\gamma_2}$ . Then  $G_1$  and  $G_2$  are the required open sets separating  $\gamma_1$  and  $\gamma_2$ .

Proposition 4.1 is applicable to globally hyperbolic as well as non-globally hyperbolic spacetimes, provided it is strongly causal. Low has proved that a strongly causal spacetime equipped with the path topology is globally hyperbolic if and only if  $\zeta_L^\rho$  is Hausdorff [11]. Minkowski space with  $t$ -topology is an example of a globally hyperbolic spacetime [13]. Therefore, the space of endless causal curves in it will be Hausdorff. Though, global hyperbolicity is an essential ingredient of Penrose singularity theorems [7], it is considered to be inconsistent with the phenomenon of black hole radiations [12]. We have also considered specific spacetimes which are non-globally hyperbolic. However, the space of endless causal curves in a non-globally hyperbolic spacetime will be non-Hausdorff [11]. This leads to the following corollary:

**Corollary 4.1** If  $L^\rho$  is non-globally hyperbolic but strongly causal then  $\zeta_L^\rho$  is non-regular, non-completely regular, and non-normal.

*Proof:* The result immediately follows from Proposition 4.1 and the fact that if a topological space is  $T_1$  and satisfies any of the following topological properties: (1) normal, (2) regular, (3) completely regular, then it is also Hausdorff [14].

Let  $H_c := \{y \in M : y^{(0)} = c\}$  for some  $c \in R$ , denotes an  $(n - 1)$  dimensional surface consisting of points in  $M$  having same time coordinate. We provide below a simpler alternate proof for the fact that the space of endless causal curves in  $M^t$ , denoted by  $\zeta_M^t$ , is Hausdorff.

**Proposition 4.2** Any two distinct endless causal curves in  $M^t$  can be separated by disjoint open sets in  $\zeta_M^t$ , i.e.,  $\zeta_M^t$  is Hausdorff.

*Proof:* Let  $\gamma_1, \gamma_2 \in \zeta_M^t$ , where  $\gamma_1 \neq \gamma_2$ . Since  $M$  is globally hyperbolic and every globally hyperbolic spacetime is strongly causal [13],  $\text{Im}(\gamma_1) \not\subseteq \text{Im}(\gamma_2)$  and  $\text{Im}(\gamma_2) \not\subseteq \text{Im}(\gamma_1)$ , in view of Lemma 4.1. Therefore, we obtain  $x_1 \in \text{Im}(\gamma_1)$  and  $x_2 \in \text{Im}(\gamma_2)$ , where  $x_1 \neq x_2$ . Now,  $x_1, x_2 \in H_c$  for some  $c \in R$ , for  $H_c$  is a Cauchy surface intersecting every endless causal curve [18]. Using Hausdorffness of  $M^t$  and the fact that  $x_1, x_2 \in H_c$ , one can select two disjoint basic open sets in  $M^t$ , say  $U_1$  and  $U_2$  containing  $x_1$  and  $x_2$ , such that  $C^T(x) \cap U_2 = \emptyset$ , for all  $x \in U_1$  and  $C^T(z) \cap U_1 = \emptyset$ , for all  $z \in U_2$ . From this, we can say that there does not exist any endless causal curve lying in  $B_{U_1}^{\gamma_1} \cap B_{U_2}^{\gamma_2}$ . Therefore,  $B_{U_1}^{\gamma_1}$  and  $B_{U_2}^{\gamma_2}$  are the required disjoint

open sets separating  $\gamma_1$  and  $\gamma_2$ .

*Proposition 4.3* The space  $\zeta_M^t$  is regular.

*Proof:* Let  $\gamma \in \zeta_M^t$  and  $F$  be an arbitrary closed set in  $\zeta_M^t$  not containing  $\gamma$ . Since  $F^c$  is open in  $\zeta_M^t$  and  $\gamma \in F^c$ , there exists a basic open set  $E$  containing  $\gamma$ , such that  $E \subseteq F^c$ . It is easy to show that there exist  $p_i \in Im(\gamma)$  and basic open set  $U_i$  containing  $p_i$  in  $M^t$  for  $i = 1, 2, \dots, k$ ; such that  $G := \bigcap_{i=1}^k B_{U_i}^\gamma \subseteq E$ . If  $\alpha \in F$ , then  $Im(\alpha) \cap U_i = \emptyset$ , for some  $i \in \{1, 2, \dots, k\}$ . Let  $q_i \in U_i \cap Im(\gamma)$ ,  $q_i \neq p_i$ . Choose  $r_i > 0$ , such that  $N_{r_i}^E(q_i) \subseteq U_i$ . Now,  $q_i \in H_c$ , where  $c = q_i^0$ . Also,  $N_{r_i}^E(q_i)$  is constructed in a way such that  $Im(\alpha) \cap H_c$  is contained in the complement of  $A_i := Cl(C^T(\gamma))$ , for all  $\gamma \in N_{r_i}^E(q_i)$  and for any  $\alpha \in F$ , where  $Im(\alpha) \cap U_i = \emptyset$ . Let  $\{z_\alpha\} = Im(\alpha) \cap H_c$ , as  $H_c$  intersects with  $Im(\alpha)$  exactly once [16]. Hence, there exists an open set  $U_{z_\alpha}$  containing  $z_\alpha$ , which does not intersect with  $A_i$  and  $Cl(C^T(x)) \cap N_{r_i}^E(q_i) = \emptyset$ , for  $x \in U_{z_\alpha}$ . This implies that  $B_{N_{r_i}^E(q_i)}^\gamma \cap B_{U_{z_\alpha}}^\alpha = \emptyset$ . Therefore,  $G_F := \bigcup_{\alpha \in F} U_{z_\alpha}$ ;  $z_\alpha \in Im(\alpha)$  and  $G_\gamma := \bigcap_{i=1}^k B_{N_{r_i}^E(q_i)}^\gamma$  are the required disjoint open covers.

## V. CONCLUSION

In this paper it is shown that the collection of causal curves equipped with the topology defined by Low [11] does not satisfy major separation axioms. This does not provide an understanding of the separation axioms of its subspaces. So, an independent study of the separation axioms of the subspace consisting of endless causal curves, which is considered to be of significance in the study of singularities [11], has been undertaken. It has been proved that in general, the space of endless causal curves does not satisfy most of the separation axioms; but if the spacetime is strongly causal, then it is  $T_1$  and if the spacetime is in addition non-globally hyperbolic, then this subspace is non-regular, non-completely regular and non-normal. In Minkowski spacetime equipped with  $t$ -topology, this subspace has been found to be regular. This differentiates topologically the space of endless causal curves from its parent space.

## REFERENCES

- [1] Agrawal, G., Shrivastava, S. (2009).  $t$ -topology on the  $n$ -dimensional Minkowski Space. *J. Math. Phys.*, 50, 053515.
- [2] Agrawal, G., Shrivastava, S. (2009, November). A non-Euclidean topology proposed by Zeeman. *Proc. Joint Int. Conf. ASR-NSC*.
- [3] Dossena, G. (2007). Some results on the Zeeman topology. *J. Math. Phys.*, 48, 113507.
- [6] Geroch R., Kronheimer, E. H., & Penrose R. (1972). Ideal points in space-time. *Proc. R. Soc. Lond. A.*, 327, 545-567.
- [7] Hawking, S. W., Ellis, G. F. R. (1973). *The large scale structure of space-time* (1<sup>st</sup> ed.). Cambridge University Press, Cambridge.
- [8] Hawking, S. W., King, A. R., & McCarthy, P. J. (1976). A new topology for curved space-time which incorporates the causal, differential, and conformal structures, *J. Math. Phys.*, 17, 174-181.
- [9] Low, R. J. (1989). The geometry the space of null geodesics. *J. Math. Phys.* 30, 809. <https://doi.org/10.1063/1.528401>
- [10] Low, R. J. (1990). Spaces of causal paths and naked singularities, *Class. Quantum Grav.*, 7, 943-954. <https://iopscience.iop.org/article/10.1088/0264-9381/7/6/004>
- [11] Low, R. J. (2016) Spaces of paths and the path topology, *J. Math. Phys.*, 57, 92503. <https://doi.org/10.1063/1.4963144>
- [12] Minguzzi, E. (2020, March 3). A gravitational collapse singularity theorem consistent with black hole evaporation. *Lett. Math. Phys.*, 110 (9), 2383-2396.
- [4] Galloway, G. J. (2014, August 4). Notes on Lorentzian causality. ESI-EMS-IAMP Summer School on Mathematical Relativity. <https://www.math.miami.edu/~galloway/vienna-course-notes.pdf>
- [5] Geroch, R. (1968). What is Singularity in General Relativity? *Annals of Phys., Princeton*, 48, 526-540. <https://archiv.org/abs/1909.07348>
- [13] Minguzzi, E., Sanchez, M. (2008). The causal hierarchy of spacetimes. *J. Math. Phys.*, Soc., Zurich, 299-358. <https://arxiv.org/abs/gr-qc/0609119>
- [14] Munkres, J. R. (2002, January 1). *Topology: A first course* (2<sup>nd</sup> ed.). Prentice Hall India Learning Pvt. Ltd.
- [15] Ong, Y. C. (2020, May 26). Spacetime Singularities and Cosmic Censorship Conjecture: A Review with Some Thoughts. Unpublished manuscript. Downloaded from <https://arxiv.org/abs/2005.07032>
- [16] Penrose, R. (1972). Techniques of Differential Topology in Relativity. Regional Conference Series in Applied Math. 7, *Society of Industrial and Applied Mathematics*, Philadelphia.
- [17] Penrose, R., & Hawking, S. (1996). *The Nature of Space and Time*, Princeton University Press, Princeton.
- [18] Wald, R. M. (1984, June 1). *General Relativity* (UK ed.). The University of Chicago Press, Chicago and London.
- [19] Zeeman, E. C. (1964). Causality implies the Lorentz group. *J. Math. Phys.*, 5, 490-493.
- [20] Zeeman, E. C. (1967). The topology of Minkowski space, *Topology*, 6, 161-17.

# APPENDIX

## NSC-2021 CONFERENCE COMMITTEE

### CHIEF PATRON

**Prof. P. S. Satsangi**

*Chairman*

Advisory Committee on Education

Dayalbagh Educational Institutions, Dayalbagh, Agra 282005

### PATRON

**Prof. P.K. Kalra**

*Director*

Dayalbagh Educational Institute, Dayalbagh, Agra 282005

### INTERNATIONAL ADVISORY COMMITTEE

(Late) Dr. Vijai Kumar, President, DEI

Prof. Peter H. Roe, University of Waterloo, Canada

Prof. Keith W. Hipel, University of Waterloo, Canada

Prof. Ashok Agarwal, University of Maryland, USA

Prof. Anand Srivastava, Kiel University, Germany

Prof. Anna Horatchek, Kiel University, Germany

Dr. Anirban Bandyopadhyay, NIMS, Japan

Prof. Karmeshu, Shiv Nadar University

Prof Huzur Saran, IIT Delhi

Mr. M.A. Pathan, Former Chairman Indian Oil Corporation Ltd.

Prof. D K Srivastava, TISS

Prof. Pami Dua, Delhi School of Economics

Prof. Prem Kumar Kalra, IIT Delhi, President, SSI

Prof. C. Patvardhan, DEI, Vice-President, SSI

### PROGRAM AND ORGANISING COMMITTEE

Prof. K Soami Daya, Faculty of Science, DEI, Convener NSC

Dr. P.S. Sudhish, Faculty of Science, DEI, Coordinator Plenary Speakers

Prof. Sanjay Bhushan, Faculty of Social Science, DEI

Dr. Sanjay Saini, Faculty of Science, DEI

Shri Dheeraj Kumar Angajala, Technical College, DEI

Dr. Neetu Gupta, Faculty of Arts, DEI

Prof. D. Bhagwan Das, Faculty of Engineering, DEI, Secretary, SSI

### SESSION CHAIRS

Dr. Dayal Pyari Srivastava, DEI

Prof. K. Soami Daya, DEI

Prof. P.K. Kalra, IIT Delhi

Dr. Bani Dayal Dhir, DEI

Dr. P.S. Sudhish, DEI

Prof. D. Bhagwan Das, DEI

(Late) Prof. P.K. Dantu, DEI

Prof. Sunita Malhotra, DEI

Prof. G.S.S. Babu, DEI

Dr. Sonal Singh, DEI

Prof. Praveen Saxena, DEI

Dr. Ranjit Kumar, DEI

Prof. Swami P. Saxena, DEI

Dr. Saurabh Mani, DEI

Dr. Sanjay Saini, DEI

Dr. Rohit Rajwanshi, DEI

Prof. Sandeep Paul, DEI

Dr. Kumar Ratnakar, DEI

Prof. V.K. Gangal, DEI

Prof. Vijay S. Caprihan, DEI